SEARCH FOR PAIR PRODUCED HEAVY QUARKS DECAYING INTO A Z BOSON AND A LIGHT GENERATION JET

by

Serhat Iştın

M.S, Physics, Boğaziçi University, 2008

Submitted to the Institute for Graduate Studies in
Science and Engineering in partial fulfillment of
the requirements for the degree of
Doctor of Philosophy

Graduate Program in Physics
Boğaziçi University
2015

ACKNOWLEDGEMENTS

I would like to express my sincere gratitude to my thesis supervisor V. Erkcan Özcan for his guidance and endless support during the development of this work, and especially to Prof. Metin Arık for always inspiring people around him both on professional and personal level.

Many special thanks to the colleagues from CERN, Joe Haley, Suyog Shreshta and Nicholas Bousson for arranging motivating meetings and for their collaboration spirit.

Last but not least, many thanks to the folks from Boğaziçi, Bora Işıldak, Cem Erol, Kazım Çamlıbel, Cemile Ezer, Burcu Ersoy, Yavuz Öz, Erol Ertan. Without your true friendship, my entire graduate life would be too boring.

ABSTRACT

SEARCH FOR PAIR PRODUCED HEAVY QUARKS DECAYING INTO A Z BOSON AND A LIGHT GENERATION JET

We present here our results from the search for the pair production of new massive quarks using 20fb^{-1} data collected by the ATLAS detector in 2012 proton-proton collisions at $\sqrt{s}$ =8TeV centre of mass energy. There are many models extending beyond the well established Standard Model (SM) predicting additional massive quarks on top of the existing quark list. One of them is the grand unified theory (GUT) having the exceptional E_6 as its symmetry group. This model predicts an additional iso-singlet down type quark for each existing SM family with possible decay channels involving $W^{\pm}, Z$ and H. Assuming a similar mass structure, the lightest of these quarks denoted by the letter D would be the first one to be discovered at ATLAS. Our search focuses on the decay signature of D quark decays via a Z boson which would further decay into two leptons. The other heavy quark searches at ATLAS are carried out with the assumption that the new quarks should couple to the heavy generations t,b only with final states involving b-quarks. Our search differs by vetoing the b-quarks in the final state. No excess events have been observed beyond the backgrounds of the SM. Our measurements are consistent with the SM expectations without a significant deviation. We exclude the heavy quarks with mass less than 530 GeV with 95% confidence level using the branching ratios predicted by the E_6 model. A higher mass limit of 730 GeV is put with the assumption that quarks decay in the Z channel with 100% branching ratio.

ÖZET

Z BOZONU VE HAFİF AİLE JETLERİNE BOZUNAN AĞIR KUARKLARIN ÇİFT ÜRETİMLERİNİN ARAŞTIRILMASI

Olası muhtemel yeni kuarkların çift üretilimi, ATLAS algıcı tarafından 2012 yılında toplanılan 20.3 fb^{-1} lık 8 TeV lik proton-proton çarpışma deneyi verilerinde araştırılmıştır. Mevcut Standart Model (SM) ötesine uzanan kimi modellerde, hali hazırdaki üç kuark ailesi dışında yeni ağır kuarklar öngörülmektedir. Bu modellerden bir tanesi E_6 grup simetrisini temel alan Büyük Birleştime Kuramı'dır. Bu modele göre her mevcut kuark ailesine ekleme olarak birer alt-tip izo-singlet kuark var olmalıdır. Bu kuarklar $W^{\pm}$, H ve Z bozonları kanallarıyla bozunmaktadırlar. Standart Model'deki kütle sıralanmasının bu model için de geçerli olduğunu var sayarsak, yeni kuarklardan D harfi ile gösterdiğimiz en hafif olanı ATLAS deneyinde ilk keşfedilen olması beklenmektedir. ATLAS Deneyi'ndeki diğer ağır kuark araştırmaları sadece üçüncü aile ile etkileşen senaryolar için yürütülmektedir. Bizim çalışmamız bunlardan farklı olarak son durumlarda b-jetlerin/kuarkların var olmaması gerekliliğine dayanmaktadır. Çalışmamızda SM ardalan olaylarının üzerine ek olarak başka olaylar gözlemlenmedi. Bütün ölçümlerimiz SM beklentileri ile önemli sapmalar olmaksızın uyumludur. Tamamen Z kanalı ile bozunma senaryosunda 730 GeV den hafif kuarkları %95 güvenilirlik seviyesinde elemiş bulunuyoruz. E_6 modelinin öngördüğü dallanma oranları için kütle alt sınırı 530 GeV olarak ölçülmüştür.

TABLE OF CONTENTS

ACKNOWLEDGEMENTS iii

ABSTRACT iv

ÖZET v

LIST OF FIGURES ix

LIST OF TABLES xvii

LIST OF ACRONYMS/ABBREVIATIONS xviii

1. INTRODUCTION 1
    - 1.1. The Standard Model 1
        - 1.1.1. Electroweak Theory 2
        - 1.1.2. Quantum Chromodynamics 6
    - 1.2. Beyond The Standard Model 8
        - 1.2.1. Non-zero neutrino masses 8
        - 1.2.2. Matter Dominated Universe 8
        - 1.2.3. Dark Matter 8
        - 1.2.4. Hierarchy Problem 9
        - 1.2.5. Gravity 9
        - 1.2.6. Grand Unified Theories 9
    - 1.3. CERN 11
    - 1.4. The Large Hadron Collider 12
    - 1.5. ATLAS Detector 16
        - 1.5.1. ATLAS Coordinate System 17
        - 1.5.2. Inner Detector 18
            - 1.5.2.1. Pixel Detector 19
            - 1.5.2.2. SCT Detector 19
            - 1.5.2.3. Transition Radiation Tracker 19
        - 1.5.3. Calorimetry 21
            - 1.5.3.1. Electromagnetic Calorimeter 22
            - 1.5.3.2. Hadronic Calorimeter 23
        - 1.5.4. Muon Spectrometer 23

- 1.5.5. Magnet System 24
  - 1.5.5.1. Solenoid 24
  - 1.5.5.2. Toroid 25
- 1.5.6. Trigger and Data Acquisition System 25

2. HEAVY QUARK ANALYSIS 28
- 2.1. Analysis Strategy 28
- 2.2. Data Sample 29
- 2.3. Simulated Samples 31
  - 2.3.1. Background Samples 32
  - 2.3.2. Signal Samples 35
- 2.4. Reconstructed Physics Objects 37
  - 2.4.1. Tracks and Vertices 37
  - 2.4.2. Electrons 38
  - 2.4.3. Muons 40
  - 2.4.4. Jets 41
  - 2.4.5. *b*-Jet Identification 43
- 2.5. Event Selection, Definition of Signal and Control Regions 44
  - 2.5.1. Event Pre-Selection 44
    - 2.5.1.1. Trigger requirements 44
    - 2.5.1.2. Exactly two lepton requirement 44
    - 2.5.1.3. Primary Vertex 44
  - 2.5.2. Control and Signal Regions 44
- 2.6. Comparison of the Predicted Backgrounds and Data 47
  - 2.6.1. Comparisons at the Inclusive Z Boson Selection Stage 47
  - 2.6.2. Comparisons at the $Z+\geq$ 4jets stage 60
  - 2.6.3. Comparisons after $p_{\mathrm{T}}(Z)$ requirement 70
  - 2.6.4. Comparisons after H_{T} requirement 74
  - 2.6.5. Comparisons of the reconstructed variables 76
- 2.7. Systematic Uncertainties 82
  - 2.7.1. Luminosity 83
  - 2.7.2. Background and Signal Cross Sections 83

2.7.3. Systematics related to data-driven $p_{\mathrm{T}}(Z)$ correction 84
2.7.4. Lepton Trigger, Identification, and Reconstruction 84
2.7.5. Lepton Energy-Momentum Scale and Resolution 84
2.7.6. Jet Reconstruction Efficiency and Jet Energy Scale 85
2.7.7. B-jet Uncertainties 85
3. FINAL RESULTS 88
3.1. Future Prospects 90
APPENDIX A: VALIDATION OF SIGNAL SAMPLES 91
APPENDIX B: ΔR DISTRIBUTION BETWEEN Z BOSON AND THE p_{T} ORDERED JETS 94
APPENDIX C: RECONSTRUCTION PERFORMANCE IN THE REVERTED H_{T} CONTROL REGION 97
REFERENCES 98

LIST OF FIGURES

Figure 1.1. CERN accelerator complex (not in scale). There are many experiments conducted in the accelerator complex which are drawn in different colors in the above schematic representation. 13

Figure 1.2. Multiple p-p collisons at ATLAS in 2012 [24]. 15

Figure 1.3. A schematic view of the ATLAS detector [25]. 17

Figure 1.4. A sliced view of barrel region of the inner detector of ATLAS [33]. 21

Figure 1.5. A barrel electromagnetic calorimeter module [34]. 22

Figure 1.6. Layout of the ATLAS muon system [36]. 24

Figure 1.7. Schematic of the ATLAS trigger system [39]. 27

Figure 2.1. Leading order D quark production at the LHC. 28

Figure 2.2. A pair of D quarks produced via gluon-gluon fusion and the resulting final state. 29

Figure 2.3. Integrated luminosity versus time during stable beams and for pp collisions at 8 TeV centre-of-mass energy in 2012 [24]. 31

Figure 2.4. Event processing times for ATLFAST2 and Full GEANT4 simulations [27]. 32

Figure 2.5. Some of the Z+jets production mechanisms at p-p collisions. . . 33

Figure 2.6. D quark branching ratio as predicted by E_6 iso-singlet model [19]. 36

Figure 2.7. D quark width as a function of its mass. 37

Figure 2.8. A candidate $H \to ZZ \to 4e$ event recorded in 2012 $\sqrt{s}$=8 TeV p-p collisions. The invariant mass of the 4 electron system is 124.5 GeV. Reconstructed Z boson masses are 70.6 GeV and 44.7 GeV. Calorimeter clusters are colored in green while the associated tracks and the calorimeter seeds are colored in red [58]. 39

Figure 2.9. Event display of a top pair e- μ dilepton candidate with two b-tagged jets. The electron is shown by the green track pointing to a calorimeter cluster, the muon by the long red track intersecting the muon chambers, and the missing ET direction by the dotted line on the XY view. The secondary vertices of the two b-tagged jets are indicated by the orange ellipses on the zoomed vertex region view [58]. 41

Figure 2.10. Event display of a candidate $H \to ZZ \to \mu\bar{\mu} + b\bar{b}$ event. B-jets are shown in grey cones while the muons are in blue. Invariant mass of $\mu\bar{\mu}b\bar{b}$ system is 332 GeV [58]. 43

Figure 2.11. Comparison of the discriminating variables $p_{\mathrm{T}}(Z)$ and H_{T} for the simulated signal at 600GeV and Z+jets after requiring at least 4 jets. Distributions are normalized to unity. 45

Figure 2.12. Leptonically(a) and hadronically(b) reconstructed D quark masses as discriminating variables for the signal and the Z+jets background. Distributions are normalized to unity. Distributions are obtained from simulations. 46

Figure 2.13. Comparison of the data and the simulated backgrounds in the M_Z distribution using ALPGEN(left) and SHERPA(right) Z+jets samples in the e^+e^- channel at the inclusive Z boson selection stage. . 48

Figure 2.14. Comparison of the data and the simulated backgrounds in the M_Z distribution using ALPGEN(left) and SHERPA(right) Z+jets samples in the $\mu^+\mu^-$ channel at the inclusive Z boson selection stage. 48

Figure 2.15. Comparison of the data and the simulated backgrounds in the $p_{\mathrm{T}}(Z)$ distribution using ALPGEN(left) and SHERPA(right) Z+jets samples in the e^+e^- channel. 49

Figure 2.16. Comparison of the data and the simulated backgrounds in the $p_{\mathrm{T}}(Z)$ distribution using ALPGEN(left) and SHERPA(right) Z+jets samples in the $\mu^+\mu^-$ channel. 49

Figure 2.17. $p_{\mathrm{T}}(Z)$ and M_Z distributions at the inclusive Z boson selection stage for the e^+e^- channel. Z+jets backgrounds have been modelled by MENLOPS. 50

Figure 2.18. Comparisons of $p_{\mathrm{T}}(Z)$ and M_Z distributions at the inclusive Z boson selection stage for the $\mu^+\mu^-$ channel. Z+jets backgrounds have been modelled by MENLOPS. 51

Figure 2.19. Comparisons of M_Z distributions at the inclusive Z boson selection stage for the e^+e^- channel after MENLOPS $p_{\mathrm{T}}(Z)$ correction is applied. Z+jets events are modelled by ALPGEN(left) and SHERPA(right). 52

Figure 2.20. Comparisons of M_Z distributions at the inclusive Z boson selection stage for the $\mu^+\mu^-$ channel after MENLOPS $p_{\mathrm{T}}(Z)$ correction is applied. Z+jets events are modelled by ALPGEN(left) and SHERPA(right). 52

Figure 2.21. Comparisons of $p_{\mathrm{T}}(Z)$ distributions at the inclusive Z boson selection stage for the e^+e^- channel after MENLOPS $p_{\mathrm{T}}(Z)$ correction is applied. Z+jets events are modelled by ALPGEN(left) and SHERPA(right). 53

Figure 2.22. Comparisons of $p_{\mathrm{T}}(Z)$ distributions at the inclusive Z boson selection stage for the $\mu^+\mu^-$ channel after MENLOPS $p_{\mathrm{T}}(Z)$ correction is applied. Z+jets events are modelled by ALPGEN(left) and SHERPA(right). 53

Figure 2.23. Comparisons of the jet multiplicites at the inclusive Z boson selection stage for the e^+e^- channel. Z+jets events are modelled by ALPGEN(left) and SHERPA(right). 54

Figure 2.24. Comparisons of the jet multiplicites at the inclusive Z boson selection stage for the $\mu^+\mu^-$ channel. Z+jets are modelled by ALPGEN(left) and SHERPA(right). 55

Figure 2.25. Comparisons of the b-jet multiplicites at the inclusive Z boson selection stage for the e^+e^- channel. Z+jets events are modelled by ALPGEN(left) and SHERPA(right). 56

Figure 2.26. Comparisons of the b-jet multiplicites at the inclusive Z boson selection stage for the $\mu^+\mu^-$ channel. Z+jets events are modelled by ALPGEN(left) and SHERPA(right). 56

Figure 2.27. Comparisons of M_Z with the side-bands outside the Z mass window in the 0 b-tag exclusive bin. Left(Right) column consists of ALPGEN(SHERPA) Z+jets sample. 57

Figure 2.28. Comparisons of M_Z with the side-bands outside the Z mass window in the 1 b-tag exclusive bin. Left(Right) column consists of ALPGEN(SHERPA) Z+jets sample. 58

Figure 2.29. Comparisons of M_Z with the side-bands outside the Z mass window in the 2 b-tag inclusive bin. Left(Right) column consists of ALPGEN(SHERPA) Z+jets sample. 59

Figure 2.30. b-jet multiplicities after requiring at least 4 jets obtained by ALPGEN(left) and SHERPA(right) in the e^+e^- channel. 60

Figure 2.31. b-jet multiplicities after requiring at least 4 jets obtained by ALPGEN(left) and SHERPA(right) in the $\mu^+\mu^-$ channel. 61

Figure 2.32. b-jet multiplicity corrections derived in the nominal and systematic regions in the Z+$\geq$4 jets sample in the e^+e^- channel. 61

Figure 2.33. b-jet multiplicity corrections derived in the nominal and systematic regions in the Z+$\geq$4 jets sample in the $\mu^+\mu^-$ channel. 62

Figure 2.34. b-jet multiplicities after requiring at least 4 jets obtained by ALPGEN(left) and SHERPA(right) in the $\mu^+\mu^-$ channel when the b-jet scaling correction is applied. 63

Figure 2.35. Third leading jet p_{T} shape for the simulated signal and total expected background after requiring at least 4 jets. The distributions are normalized to unity. 64

Figure 2.36. $p_{\mathrm{T}}(Z)$ distribution at $Z+\geq 4$ jets stage after b-jet multiplicity scaling and before data-driven $p_{\mathrm{T}}(Z)$ correction is applied. Left(Right) column consists of ALPGEN(SHERPA) Z+jets sample. 65

Figure 2.37. $p_{\mathrm{T}}(Z)$ distribution at $Z+\geq 4$ jets stage after data driven $p_{\mathrm{T}}(Z)$ correction is applied. Left(Right) column consists of ALPGEN(SHERPA) Z+jets sample. 66

Figure 2.38. Data-driven $p_{\mathrm{T}}(Z)$ corrections and their systematic variations for ALPGEN and SHERPA Z+jets samples in the ee channel. 67

Figure 2.39. Data-driven $p_{\mathrm{T}}(Z)$ corrections and their systematic variations for ALPGEN and SHERPA Z+jets samples in the $\mu^+\mu^-$ channel. . . 68

Figure 2.40. ΔR between Z boson and the first four hardest jets in the event at $Z+\geq 4$ jets sample after data-driven $p_{\mathrm{T}}(Z)$ correction and b-jet veto are applied. Distributions are obtained by SHERPA Z+jets sample. 70

Figure 2.41. M_Z distributions in $Z+\geq 4$ jets sample after applying $p_{\mathrm{T}}(Z)$ cuts and b-jet veto. Left(right) column consists of ALPGEN (SHERPA) Z+jets sample. 71

Figure 2.42. H_{T} distributions in $Z+\geq 4$ jets sample after applying $p_{\mathrm{T}}(Z)$ cut. Left(right) column consists of ALPGEN (SHERPA) Z+jets sample. 72

Figure 2.43. M_Z distributions in $Z+\geq 4$ jets sample after applying H_{T} cut. Left(right) column consists of ALPGEN (SHERPA) Z+jets sample. 74

Figure 2.44. $p_{\mathrm{T}}(Z)$ distributions in $Z+\geq 4$ jets sample after applying H_{T} cut obtained by ALPGEN(left) and SHERPA. 75

Figure 2.45. Leptonically reconstructed D quark mass in e^+e^- and $\mu^+\mu^-$ channels with ALPGEN(left) and SHERPA. 77

Figure 2.46. Hadronically reconstructed W/Z boson mass in e^+e^- and $\mu^+\mu^-$ channels as obtained from ALPGEN(left) and SHERPA. 79

Figure 2.47. Mass difference between pairs of reconstructed D quarks in the both channels as obtained by ALPGEN(left) and SHERPA. 80

Figure 2.48. Leptonically reconstructed D quark mass after $|M_D - M_{\bar{D}}|$ and $|M_{jj} - M_V| \leq 100$ GeV cuts in the both channels obtained by ALPGEN(left) and SHERPA. 81

Figure 3.1. Expected and observed 95% CL upper limits on the D quark pair production cross section. The green and yellow bands correspond to the 1 and 2 standard deviations around the expected limit where the blue line shows the theoretical prediction. 89

Figure A.1. Heavy quark mass and angular separation between bosons and the associated jets for the signal events at the truth level 91

Figure A.2. Traansverse momenta of the bosons and the jets coupled to the heavy quark for the signal events at the truth level 92

Figure A.3. Applied event weight distributions for each decay mode for the signal events 93

Figure B.1. ΔR between Z boson and the second hardest jet in the event at Z+$\geq$ 4 jets sample after data-driven $p_{\mathrm{T}}Z$ correction and b-jet veto are applied. Left(right) column is obtained by ALPGEN(SHERPA) Z+jets sample 94

Figure B.2. ΔR between Z boson and the third hardest jet in the event at Z+$\geq$ 4 jets sample after data-driven $p_{\mathrm{T}}Z$ correction and b-jet veto are applied. Left(right) column is obtained by ALPGEN(SHERPA) Z+jets sample 95

Figure B.3. ΔR between Z boson and the fourth hardest jet in the event at Z+$\geq$ 4 jets sample after data-driven $p_{\mathrm{T}}Z$ correction and b-jet veto are applied. Left(right) column is obtained by ALPGEN(SHERPA) Z+jets sample 96

Figure C.1. Leptonically reconstructed D quark mass in e^+e^- and $\mu^+\mu^-$ channels with ALPGEN(left) and SHERPA in the reverted H_{T} control region 97

LIST OF TABLES

Table 1.1. List of SM quarks. 2

Table 1.2. List of SM bosons. 2

Table 1.3. LHC design and operating parameters 14

Table 2.1. Data Periods. 30

Table 2.2. List of all simulated backgrounds used in this analysis and their corresponding cross sections. 34

Table 2.3. Number of expected and observed events in $Z+\geq$ 4 jets sample . . 69

Table 2.4. Number of expected and observed events after $p_{\mathrm{T}}(Z) \geq 150$ GeV requirement. 73

Table 2.5. Number of expected and observed events after $H_{\mathrm{T}} \geq 600 GeV$ requirement. 76

Table 2.6. Number of expected and observed events in the reconstructed sample. 78

Table 2.7. Number of expected and observed events in the final selection. . . 82

Table 2.8. List of all systematic errors in the e^+e^- channel 86

Table 2.9. List of all systematic errors in the $\mu^+\mu^-$ channel 87

LIST OF ACRONYMS/ABBREVIATIONS

ALICE	A Large Ion Collider Experiment
ATLAS	A Toroidal LHC Apparatus
BR	Branching Ratio
CERN	Conseil Européen pour la Recherche Nucléaire
CKM	Cabbibo Kobayashi Matsawa
CMS	Compact Muon Solenoid
CP	Charge-Parity
CSC	Cathode Strip Chamber
ECAL	Electromagnetic Calorimeter
EF	Event Filter
EMB	Electromagnetic Barrel
EMEC	Electromagnetic End Cap
EW	Electro Weak
FCal1	Forward Calorimeter 1
FCal2	Forward Calorimeter 2
FCal3	Forward Calorimeter 3
GUT	Grand Unified Theory
HCAL	Hadronic Calorimeter
HEC	Hadronic End Cap
HLT	High Level Trigger
ID	Inner Detector
LAr	Liquid Argon
LEP	Large Electron Positron collider
LHC	Large Hadron Collider
LHCb	LHC Beauty
LHCf	LHC Forward
LINAC-2	Linear Accelerator-2
LLR	Log Likelihood Ratio

LO	Leading Order
LVL1	Level 1
LVL2	Level 2
LVL3	Level 3
MDT	Monitored Drift Tube
MET	Missing Transverse Energy
MS	Muon Spectrometer
NLO	Next to Leading Order
NNLO	Next to Next to Leading Order
OSSF	Opposite Sign Same Flavor
PDF	Parton Distribution Function
PMT	Photo Multiplier Tube
PS	Proton Synchrotron
PSB	Proton Synchrotron Booster
pQCD	Perturbative QCD
QCD	Quantum Chromo Dynamics
RPC	Resistive Plate Chamber
SCT	Semi Conductor Tracker
SM	Standard Model
SSB	Spontaneous Symmetry Breaking
TDAQ	Trigger and Data Acquisition
TGC	Thin Gap Chamber
TileCal	Tile Calorimeter
TOTEM	Total Cross Section, Elastic Scattering and Diffraction Dissociation
TR	Transition Radiation
TRT	Transition Radiation Tracker
UA1	Underground Area 1
UA2	Underground Area 2
WWW	World Wide Web

1. INTRODUCTION

1.1. The Standard Model

The Standard Model (SM) explains interactions and behaviors of particles at the sub-atomic scale as a set of quantum field theories contributed by many scientists since 1920s with the foundation of quantum electrodynamics. SM covers all the fundamental forces except the gravity enabling us to make precise calculations which are consistent and verified by the experimental data up to date. The theory has been tested extensively in higher energy scales along with the advancements in the accelerator technologies.

In the SM, the fundamental particles are spin-$\frac{1}{2}$ fermions interacting by exchange of spin-1 gauge bosons. The fermions are mainly categorized as quarks and leptons depending on whether they carry color charge or not respectively . Leptons are grouped in two main categories, the charged leptons (e, μ, τ) and the associated neutrinos with no electric charge $(\nu_e, \nu_\mu, \nu_\tau)$. Aside from leptons, quarks carry color charge and they are denoted by symbols u, c, t, d, s, b where the first three are up-type and the latter are down-type. Leptons undergo electromagnetic and weak interactions while quarks undergo the strong interaction additionally. Various properties of these fermions and bosons in the SM are given in Table 1.1 and 1.2.

The SM possesses an overall group structure of $SU(3)_C \times SU(2)_L \times U(1)_Y$ underlying in its symmetries. $SU(3)_C$ part defines the theory of strong interactions known as the quantum chromo-dynamics (QCD) where the part $SU(2)_L \times U(1)_Y$ corresponds to the electroweak part of the theory which unifies electromagnetism and weak interactions within a single framework.

Table 1.1. List of SM fermions [1].

Name	Particle	Anti-Particle	Family	Charge(e)	Mass[MeV]
up	u	$\bar{u}$	1st gen.	$+2/3$	$2.3^{+0.7}_{-0.5}$
down	d	$\bar{d}$	1st gen.	$-1/3$	$4.8^{+0.5}_{-0.3}$
charm	c	$\bar{c}$	2nd gen.	$+2/3$	1275 ± 25
strange	s	$\bar{s}$	2nd gen.	$-1/3$	95 ± 5
top	t	$\bar{t}$	3rd gen.	$+2/3$	173070 ± 720
bottom	b	$\bar{b}$	3rd gen.	$-1/3$	4180 ± 30
electron	e	$\bar{e}$	1st gen.	-1	0.511
electron neutrino	ν_e	$\bar{\nu_e}$	1st gen.	0	≤0.0000022
muon	μ	$\bar{\mu}$	2nd gen.	-1	105.7
muon neutrino	ν_μ	$\bar{\nu_\mu}$	2nd gen.	0	≤0.170
tau	τ	$\bar{\tau}$	3rd gen.	-1	1777
tau neutrino	ν_τ	$\bar{\nu_\tau}$	3rd gen.	0	≤15.5

Table 1.2. List of SM bosons [1].

Name	Particle	Force	Charge(e)	Mass[GeV]	Width[GeV]	Spin
photon	γ	EM	0	0	0	1
gluon	g	strong	0	0	0	1
Higgs	H	–	0	125.9 ± 0.4	≤0.01	0
Z boson	Z	weak	0	91.188 ± 0.002	2.495 ± 0.002	1
W boson	$W^\pm$	weak	±1	80.390 ± 0.015	2.085 ± 0.042	1

1.1.1. Electroweak Theory

Glashow-Weinberg-Salam model is the gauge theory describing electromagnetic and weak interactions in a common framework. It has the group symmetry of $SU(2)_L \times$

$U(1)_Y$ with subscript L denoting the left-handed weak interactions while Y denotes the hypercharge defined in Gell-Mann Nishijima formula [2,3] $Q = T_3 + \frac{1}{2}Y$. Q is the ordinary electric charge and T_3 is the third component of the weak isospin. The model became extremely successful especially with its predictions of $W^{\pm}$ and Z bosons which was discovered later by UA1 and UA2 collaborations at CERN [4–6]. The model has yielded precise calculations consistent with the measurements from LEP, TEVATRON and finally LHC. It is the first successful model attempting to yield a unified description of the interactions under a single model.

The fermionic fields will transform under $SU(2)_L \times U(1)_Y$ like:

$$\psi \longrightarrow \psi' = e^{\frac{i}{2}\vec{\sigma}\cdot\vec{\alpha}} e^{i\frac{Y}{2}\beta}\psi \tag{1.1}$$

To preserve the interactions, massless gauge fields W_μ^i (i=1, 2, 3) B_μ with two different couplings g and g' corresponding to $SU(2)_L$ and $U(1)_Y$ are included in the covariant derivative of the model:

$$D_\mu = \left(\partial_\mu - i\frac{g}{2}\boldsymbol{\sigma}\cdot\boldsymbol{W_\mu} - i\frac{g'}{2}YB_\mu\right) \tag{1.2}$$

The observed $W^{\pm}$ bosons are defined in terms of the 1st and 2nd components of the above $\boldsymbol{W_\mu}$:

$$W_\mu^{\pm} = \frac{1}{\sqrt{2}}\left(W_\mu^1 \pm iW_\mu^2\right) \tag{1.3}$$

The remaining component W_μ^3 and B_μ construct the neutral interactions with Z and the photon fields A_μ:

$$\begin{pmatrix} Z_\mu \\ A_\mu \end{pmatrix} = \begin{pmatrix} \cos\theta_W & -\sin\theta_W \\ \sin\theta_W & \cos\theta_W \end{pmatrix} \begin{pmatrix} W_\mu^3 \\ B_\mu \end{pmatrix} \tag{1.4}$$

The angle θ_W is called the Weinberg angle for weak mixing. It appears as a free parameter in the SM whose value is determined by the experiment. Ordinary electric charge $\boldsymbol{e}$ and the coupling constants $\boldsymbol{g/g'}$ are related through the Weinberg angle as :

$$g\sin\theta_W = g'\cos\theta_W = e \tag{1.5}$$

In the electroweak (EW) model, only left handed fermions ψ_L transform non-trivially under $SU(2)_L$. The chiral states ψ_L and ψ_R are the eigenstates of the projection operators :

$$P_L = \frac{1-\gamma_5}{2} \qquad\qquad P_R = \frac{1+\gamma_5}{2} \tag{1.6}$$

Depicted in a three family picture, left-handed fermions with $T_3 = \pm\frac{1}{2}$ appear as $SU(2)_L$ doublets while right-handed fermions are $SU(2)_L$ singlets with $T_3 = 0$:

$$\begin{array}{ccccccc} \begin{pmatrix} \nu_e \\ e \end{pmatrix}_L & \begin{pmatrix} \nu_\mu \\ \mu \end{pmatrix}_L & \begin{pmatrix} \nu_\tau \\ \tau \end{pmatrix}_L & \qquad & \begin{pmatrix} u \\ d' \end{pmatrix}_L & \begin{pmatrix} c \\ s' \end{pmatrix}_L & \begin{pmatrix} t \\ b' \end{pmatrix}_L \\ e_R & \mu_R & \tau_R & & d'_R & s'_R & b'_R \end{array}$$

where $d'_i = \sum\limits_i = V_{ij} d_j$. The matrix V is the 3×3 unitary Cabibo-Kobayashi-

Matsawa (CKM) matrix defining the quark mixings due to different mass and weak eigenstates.

$$\begin{pmatrix} d' \\ s' \\ b' \end{pmatrix} = \begin{pmatrix} |V_{ud}| & |V_{us}| & |V_{ub}| \\ |V_{cd}| & |V_{cs}| & |V_{cb}| \\ |V_{td}| & |V_{ts}| & |V_{tb}| \end{pmatrix} = \begin{pmatrix} d \\ s \\ b \end{pmatrix}$$

The electroweak model elegantly explains the two interactions in a unified model while inspiring us with an idea of a grand unified theory of all the interactions. The model has an exact $SU(2) \times U(1)$ symmetry with massless vector bosons. However, experimental data showed that $W^{\pm}$ and Z bosons are very heavy with their masses around 90 GeV strongly suggesting that this symmetry should be broken.

Spontaneous Symmetry Breaking (SSB) of the electroweak symmetry occurs by introducing a $SU(2)_L \times U(1)_Y$ doublet Higgs field whose three of four degrees of freedom are absorbed by the gauge bosons making them massive particles. A_μ stays massless and is identified as the photon. Part of the Lagrangian defining the interaction between fermions and the electroweak gauge bosons after the symmetry breaking is :

$$\begin{aligned} \mathcal{L}_{EW} = \sum_i \bar{\psi}_i \left(i\gamma^\mu \partial_\mu - m_i - \frac{g m_i H}{2M_W} \right) \psi_i \\ -\frac{g}{2\sqrt{2}} \sum_i \bar{\psi}_i \gamma^\mu (1-\gamma^5)(T^+ W_\mu^+ + T^- W_\mu^-)\psi_i \\ -e \sum_i q_i \bar{\psi}_i \gamma^\mu \psi_i A_\mu - \frac{g}{2\cos\theta_W} \sum_i \bar{\psi}_i \gamma^\mu (g_V^i - g_A^i \gamma^5) Z_\mu \psi_i \end{aligned} \tag{1.7}$$

where summation is over all fermions. $T^{\pm}$ are isospin raising-lowering operators, q_i is the electric charge, g_V and g_A being the vectorial and axial weak coupling with the Z boson respectively.

$$\begin{aligned} g_V^i &= t_3^i - 2q_i \sin\theta_W \\ g_A^i &= t_3^i \end{aligned} \tag{1.8}$$

where t_3 is the eigenvalue for the third component of the weak isospin.

1.1.2. Quantum Chromodynamics

Quantum Chromodynamics (QCD) is the non-Abelian Yang-Mills theory describing behavior of quark and gluons under strong interaction. It has a group symmetry of $SU(3)_C$ corresponding to the conserved color charge and is described by the Lagrangian given below:

$$\mathcal{L}_{QCD} = \sum_{q,i} \bar{q}_i(i\gamma^\mu D_\mu - m_q)q_i - \frac{1}{4}G_\alpha^{\mu\nu}G_{\alpha\mu\nu} \tag{1.9}$$

where q_i is the quark field with color index $i \in$[1,2,3], m_q is the non-zero quark mass, $G_\alpha^{\mu\nu}$ is the gluon field strength tensor with color indices $\alpha \in$[1..8] in the adjoint representation of the SU(3), D_μ is the covariant derivative:

$$\begin{gathered} D_\mu = \partial_\mu + ig_s T_\alpha G^\alpha \\ G_\alpha^{\mu\nu} = \partial^\mu G_\alpha^\nu - g_s f_{\alpha bc} G_b^\mu G_c^\nu \end{gathered} \tag{1.10}$$

where g_s is the strong coupling constant and $f_{\alpha bc}$ is the SU(3) algebra structure constants.

After solving renormalization equations at the leading order, it can be shown that the strong coupling constant depends on the energy-momentum scale as follows :

$$g_s(|q^2|) = \frac{g_s(\mu^2)}{1 + g_s(\mu^2) b \ln(|q^2|/\mu^2)} \tag{1.11}$$

where b=$(11n_c$-$2n_f)/12\pi$, n_c is the number of colors and n_f is the number of quark flavors. The parameter μ defines the cutoff region where $g_s(\mu^2) \leq 1$ allowing perturbative calculations. Defining a new parameter Λ as:

$$\ln \Lambda^2 = \ln \mu^2 - \frac{12\pi}{(11n_c - 2n_f) g_s(\mu^2)} \tag{1.12}$$

we can re-write equation 1.11 as:

$$g_s(|q^2|) = \frac{12\pi}{(11n_c - 2n_f) \ln(|q^2/\Lambda^2|)} \tag{1.13}$$

The unintuitive behavior of the QCD emerges from the fact that strong coupling drastically decreases at small scales and high energies while it becomes very large at long ranges and low energies. This leads us to the idea of asymptotic freedom and color confinement. No bare color charge can be observed above distance $1/\Lambda_{QCD}$ because confinement binds quarks into color neutral hadrons. The regime where g_s is small enough to allow calculations in perturbation series is called the perturbative QCD (pQCD) region. For example, production cross sections of hypothetical heavy quarks can be obtained precisely from pQCD calculations at TeV scale proton-proton collisions. However, in the non-perturbative region, calculations are not obvious, we need various approximation methods such as lattice-QCD and string fragmentation models. [7,8]

1.2. Beyond The Standard Model

Besides all its success, the SM cannot be considered a complete description of the nature. First of all, it has a large number of free parameters that needs to be determined from experimental results.This is not a satisfying situation from theoretical grounds. Moreover, SM is so far unable to explain some phenomena that we will briefly describe below.

1.2.1. Non-zero neutrino masses

Neutrino oscillation experiments have successfully demonstrated that neutrinos change their flavor as they propagate in free space [9]. This is a consequence of differing mass and flavor eigenstates. However according to the SM, all neutrinos are left-handed so they are unable to acquire mass via the Higgs mechanism meaning that they are massless.

1.2.2. Matter Dominated Universe

Big-Bang should have produced equal amounts of matter and antimatter according to the laws of the SM. But where did all the antimatter go? Why are there no anti-galaxies? CP violation might have been able to explain the matter dominated universe but CP violation in the SM is almost 10 orders of magnitude smaller than what is really needed [10].

1.2.3. Dark Matter

Only 5% of the universe's energy-matter content is accounted for by the SM. Studies based on galactic rotational dynamics shows evidence of unknown sources of gravity which we refer as dark matter. Dark matter makes up about 20% of the energy-mass content in the observable universe [11].

1.2.4. Hierarchy Problem

Loop corrections to the Higgs boson predicts very large mass values at the order of Planck scale. To acquire the actual mass around 125 GeV [12, 13], the parameters of the standard model must be very fine-tuned. This is quite unnatural and referred as the hierarchy problem.

1.2.5. Gravity

Gravitational interaction has no place in the SM. No one has yet been successful in fitting the ideas from general relativity and quantum field theories into a single framework that is consistent wit the SM.

1.2.6. Grand Unified Theories

The problems mentioned above gives us the clue that SM is not the ultimate theory in describing the nature. There may be a larger picture where the SM is only a part of it. Grand unification theories are seeded by the idea that the current group structure of SM is a subset of a larger group G such that:

$$G \supset SU(3) \times SU(2) \times U(1) \tag{1.14}$$

Thus gravity is still not included in these theories. The smallest candidate group G is SU(5) [14]. The first unified theory based on SU(5) predicted two heavy gauge bosons X,Y which introduced transitions between quarks and leptons. This model has been excluded experimentally since it predicts that unification of the coupling constants is quite below 10^{15} GeV which contradicts the proton decay lifetime measurements [15, 16]

Another unified model is based on E_6 exceptional Lie group with its 27 dimensional representation. The model predicts additional gauge interactions and fundamental particles while putting all quarks and leptons in the same 27 multiplet [17]. The quark sector of the SM is extended by additional iso-singlet down type quarks for each family [18]:

$$\begin{pmatrix} u_L \\ d_L \end{pmatrix}, u_R, d_R, D_L, D_R \qquad \begin{pmatrix} c_L \\ s_L \end{pmatrix}, c_R, s_R, S_L, S_R \qquad \begin{pmatrix} t_L \\ b_L \end{pmatrix}, t_R, b_R, B_L, B_R \tag{1.15}$$

We assume that the mixings of D, S, B would be dominant in their corresponding SM families. Another assumption is that similar mass pattern as in the case of SM should hold for the iso-singlet quarks. This implies that the first one to be accessible by experiment is the lightest one, the D quark.

The part of the E_6 Lagrangian describing the interactions of the D quark with the SM electroweak gauge bosons is written as referenced in [18] :

$$\begin{aligned}\mathcal{L}_{\mathcal{D}} = \frac{\sqrt{4\pi\alpha_{em}}}{2\sqrt{2}\sin\theta_W}&\left[\bar{u}^{\theta}\gamma_{\alpha}(1-\gamma_5)d\cos\phi + \bar{u}\gamma_{\alpha}(1-\gamma_5)D\sin\phi\right]W^{\alpha} \\ &-\frac{\sqrt{4\pi\alpha_{em}}}{4\sin\theta_W}\left[\frac{\sin\phi\cos\phi}{\cos\theta_W}\bar{d}\gamma_{\alpha}(1-\gamma_5)D\right]Z^{\alpha} + H.C\end{aligned} \tag{1.16}$$

Here superscript θ denotes usual CKM mixing but written in the up sector, while the angle ϕ is the mixing between D and d quarks.

It is important to note here that since these D,S,B are iso-singlets, they cannot gain their masses through Yukawa couplings with the SM Higgs boson. There should either be another mechanism or the Higgs mechanims must be modified to fit the 27 multiplet in the E_6 GUT as mentioned in [17].

However the D quark decay via the SM Higgs boson is possible if the interaction between the SM Higgs and the d quark occurs before the SSB and after D-d mixing provided that $m_D > m_H$. The part of the Lagrangian related to D decays involving the Higgs boson as written in the mass basis is [19]:

$$\begin{aligned}\mathcal{L}_M^h = \frac{m_D}{v}\sin^2\phi_L \bar{D}^M D^M h - \frac{\sin\phi_L\cos\phi_L}{2v}\bar{D}^M\left[(1-\gamma_5)m_D + (1+\gamma_5)m_d\right]d^M h \\ -\frac{\sin\phi_L\cos\phi_L}{2v}\bar{d}^M\left[(1+\gamma_5)m_D + (1-\gamma_5)m_d\right]D^M h + \frac{m_d}{v}\cos^2\phi_L \bar{d}^M d^M h\end{aligned} \tag{1.17}$$

Where v is the vacuum expectation value of the Higgs field (≈250 GeV). Combining the Lagrangian parts 1.16 and 1.17 the branching fractions $B(D \longrightarrow Wu)$, $B(D \longrightarrow Zd)$, $B(D \longrightarrow Hd)$ can be calculated, they asymptotically approach to 50%, 25%, 25% respectively for very large values of the D mass.

In this dissertation, we do not consider decay channels of D involving the Higgs boson. We require at least one of Ds to decay via Z while the remaining partner is free to decay via $W^\pm$ or Z. The details of target final states will be seen in the analysis chapter.

1.3. CERN

CERN (European Center for Particle Physics) located at the French-Swiss border near Geneva was established in 1954 by the contribution of 12 Western European countries, 5 years after the famous physicist Louis de Broglie proposed the creation of a European science laboratory. Today, it is the largest particle physics laboratory in the world housing the world's most powerful particle accelerator complex known as the Large Hadron Collider (LHC) which has been built in its predecessor's tunnel measuring 27 km in circumference.

LHC took the flag from its predecessor, the LEP (Large Electron-Positron Collider) accelerator which provided data for various physics experiments until it was decomissioned in 2000. LEP began operation in 1989 delivering electron-positron collisions with the centre of mass energy tuned to 91 GeV working as a Z boson factory and made very precise measurements of Z mass and its line shape. Later on, LEP received an energy upgrade with increased center of mass energy up to 204 GeV which enabled it to produce $W^{\pm}$ pairs [20]. LEP provided valuable data for experiments on electroweak measurements and constraints on the Standard Model [21] together with constraints on the SM Higgs Boson mass [22].

Apart from its pure physics discoveries, CERN have led to many spin-off contributions to the humanity in the fields of medical imaging technologies, information technology and many others. The most striking example is the birth of World-Wide-Web (WWW) at CERN in 1990 as a distributed information system based on `hypertext` concept. Most recently, it has played an important role for creating a worldwide computation grid, which allowed the processing of the enormous amount of data used in this thesis.

1.4. The Large Hadron Collider

Search for new heavy resonances predicted by many models beyond the SM requires pushing the energy frontier as much as possible. Built in the same tunnel of the LEP, the LHC makes it possible to probe new physics at TeV energy regime. Having two counter rotating proton beams, the LHC has 7 TeV design energy per beam. However the data analyzed in this thesis have been obtained in LHC Run-1 phase in 2012 with $\sqrt{s}$=8 TeV centre of mass energy.

Before being injected into the main LHC ring, proton beams are tuned and accelerated sequentially by different machines as seen in Figure 1.1. The acceleration of the protons starts at the linear accelerator LINAC-2, which accelerates them to an energy of 50 MeV. The proton beam is then transferred to the Proton-Synchrotron Booster (PSB), where the energy is increased to 1.4 GeV. The energy is further increased to 26 GeV by the Proton-Synchrotron (PS). The protons are then injected into the Super Proton Synchrotron where they are accelerated up to 450 GeV. Finally, the SPS injects the protons into the main LHC ring in clockwise and counter-clockwise directions, where they are accelerated to their final energy at the order of TeV.

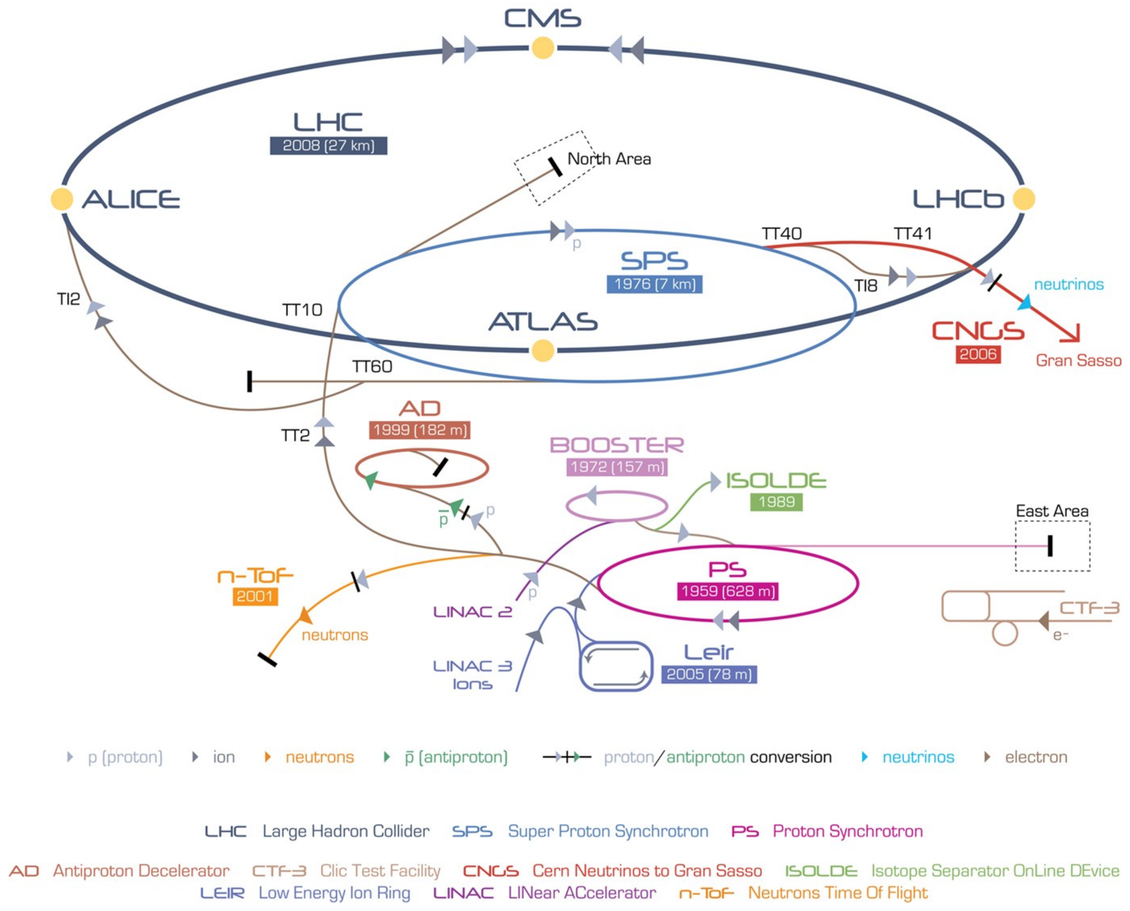

Figure 1.1. CERN accelerator complex (not in scale). There are many experiments conducted in the accelerator complex which are drawn in different colors in the above schematic representation.

Currently there are four main detectors and two forward detectors at LHC. They are ATLAS, ALICE, CMS, LHCb, LHCf and TOTEM. Together with the CMS detector, ATLAS aims to investigate general physics processes where ALICE, LHCb, LHCf and TOTEM are designed for special purposes. ALICE examines quark-gluon plasma in lead ion collisions where LHCb focuses on measuring parameters of CP violation in the interactions of b-hadrons. LHCf tries to explore the mechanism by which ultra-energetic cosmics rays interact with the atmosphere. LHCf shares the collision point with the ATLAS detector and studies forward particles emerging from the collisions. Like LHCf, the TOTEM also shares the beam intersection point with one of the big detectors CMS and studies total cross section and cross section of elastic scattering and diffractive processes.

Table 1.3. LHC design and performance parameters [23].

Parameter	Value in 2012	Design Value
Beam energy [TeV]	4	7
Bunch spacing [ns]	50	25
Number of bunches	1374	2808
Protons per bunch	1.7×10^{11}	1.15×10^{11}
Peak luminosity [$\mathrm{cm}^{-2}\mathrm{s}^{-1}$]	7.7×10^{33}	1×10^{34}
Stored beam energy [MJ]	≈ 140	≈ 362

Instantaneous luminosity is defined as the number of particle collisions per centimeter-square per-second at any given time:

$$L = \frac{N^2 k_b f}{4\pi\sigma_x^*\sigma_y^*}F \tag{1.18}$$

- N is the number of protons in a bunch.
- k_b is the number of bunches per beam.
- f is the revolution frequency of the accelerator.
- σ_x^* and σ_y^* are the horizontal and vertical beam sizes at the interaction point.
- F is a correction factor due to non-zero crossing angle of the two counter rotating beams at the interaction point.

This implies that proton density and revolution frequencies should be high with small beam size in order to achieve high luminosities. Luminosity is a very crucial parameter in high energy experiments. It determines the rate of events of any physics process with cross section σ given in barns (1barn=10^{-24} cm^2). The event rate is :

$$R = \frac{dN_{ev}}{dt} = L\sigma \tag{1.19}$$

Integrating the above equation we determine number of events that has occurred in a collider experiment. Number of events determine the statistical significance of any measurement or discovery.

$$N_{ev} = \int_{t_0}^{t_1} R(t)dt = \sigma \int_{t_0}^{t_1} L(t)dt = \sigma \mathcal{L} \tag{1.20}$$

The quantity $\mathcal{L}$ is called the integrated luminosity and often referred as the amount of data collected by a collider experiment in a given time period. The dataset used in this dissertation corresponds to 20.3 fb^{-1} integrated luminosity. The design and performance parameters of the LHC are given in table 1.3.

At high luminosities, obtaining multiple proton collisions in a single bunch crossing is highly probable. In other words, a single recorded event consists many proton collisions which are called pile-up events. Out of these, a single collision is chosen from the primary vertex with the hardest partonic interaction. The selection criteria will be mentioned later in the event selection part of the thesis. The Figure 1.2 indicates the average number of proton-proton per bunch crossing in the run of 2012.

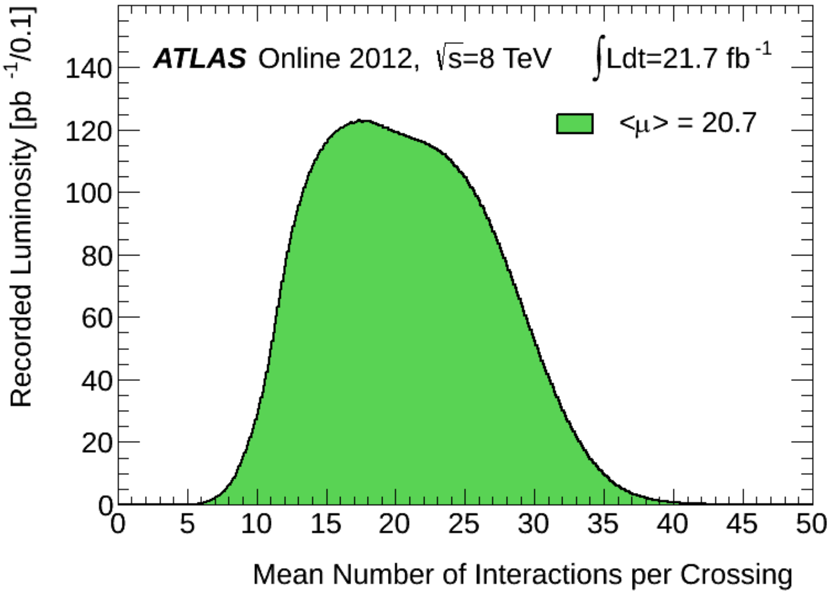

Figure 1.2. Multiple p-p collisons at ATLAS in 2012 [24].

1.5. ATLAS Detector

The ATLAS (A Toroidal LHC Apparatus) is a general purpose particle physics detector located at the southern interaction point of the LHC. It is cylindrically symmetric around the beam-line, and it is 25 m in height and 44 m in length and about 7000 tonnes in weight. The detector has been designed as concentric layers of sub-detectors. Unlike its competitor CMS(Compact Muon Solenoid), ATLAS has two distinct type of magnets, a solenoid covering the volume inside the tracker system, and the toroid magnet covering the muon spectrometer at the outermost layer.

ATLAS mainly consists of four components. Inner Detector (ID) tracks charged particles, measures momentum and provides information for particle identification. Electromagnetic and hadronic calorimeters measure energies of photons, electrons and hadrons. Muons are able to pass through all the detector layers and they are identified and measured at the outermost ATLAS layer, the Muon Spectrometer. The magnet system, a solenoid for the inner detector and an outer toroid, provides magnetic fields to bend particles and thereby achieve momentum measurements.

When operated at high luminosity, ATLAS yields enormous amounts of raw data per second most of which is irrelevant for physics studies. In order to handle this data rate and to select those events of interest for new physics searches, a three level trigger and data acquisition (TDAQ) system reduces the data rate from 20 MHz to approximately 200 Hz.

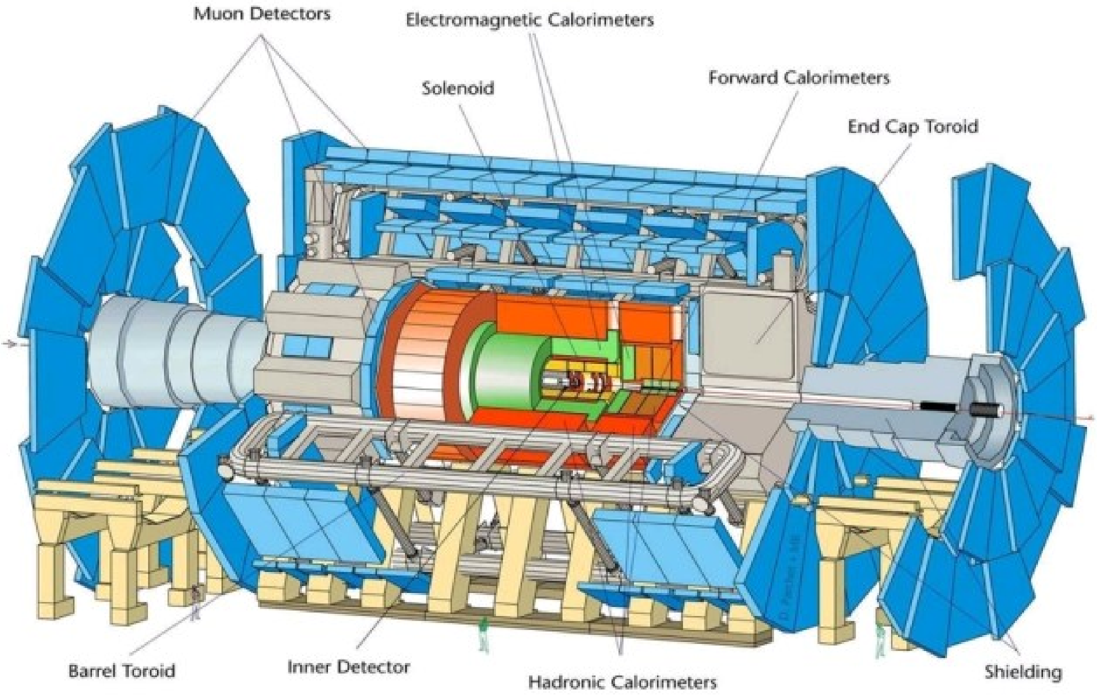

Figure 1.3. A schematic view of the ATLAS detector [25].

1.5.1. ATLAS Coordinate System

The coordinate system used at the ATLAS experiment has its origin at the interaction point with the z-axis defined pointing along the beam direction, x-axis pointing radially inward towards the center of LHC while y-axis points vertically upwards. The transverse plane refers to the $x-y$ plane and any kinematic variable with prefix "transverse" is actually projected onto this plane. The variable ϕ refers to the azimuthal angle measured in the $x-y$ plane from the x-axis while the polar angle θ is measured from the z-axis.

The entire spectrum of particles produced in TeV collision scales are highly relativistic. Also considering the fact that protons are not fundamental particles, a whole hard-scattering event might have a net boost along z direction. Instead of the polar angle θ, a more convenient variable,the pseudorapidity is defined as follows:

$$\eta = -\ln\left[\tan\left(\frac{\theta}{2}\right)\right] \tag{1.21}$$

The differences between pseudo-rapidities are invariant under Lorentz Boosts along the z-axis. Pseudorapidities transform like:

$$\eta = -\ln\left[\tan\left(\frac{\theta}{2}\right)\right] \quad \rightarrow \quad \eta' = -\ln\left[\tan\left(\frac{\theta}{2}\right)\right] - \ln\gamma \tag{1.22}$$

Another variable often used at the ATLAS coordinate system is the angular separation between two 4-momenta :

$$\Delta R = \sqrt{\Delta\phi^2 + \Delta\eta^2} \tag{1.23}$$

ΔR is also invariant under Lorentz boost along the z direction and is quite convenient in defining tracks and jets in the detector. The four momenta are usually defined in these coordinates as (p_{T}, η, ϕ, E) as a convenience where E is the energy and p_{T} is the transverse momentum.

1.5.2. Inner Detector

The inner detector (ID) is the particle tracking system of ATLAS with highly granular detector components placed very close to the interaction point. The components of the ID have been designed to provide precise spatial resolutions in highly luminous collision environments with radiation resistant sensors and electronics to perform robustly over years. The ID system covers the pseudo-rapidity region $|\eta| \leq 2.5$ with a full range of acceptance in ϕ. The whole ID system is placed inside the superconducting solenoid magnet providing a uniform magnetic field of 2 T along the beam direction to measure momentum of the charged particles. It has three concentric sub-detector components as seen in Figure 1.4, the pixel detector at the innermost followed by a semiconductor tracker and the transition radiation tracker at the outermost [26, 27].

1.5.2.1. Pixel Detector. The pixel detector covers the radial volume between 50.5 mm and 150 mm in the form of three concentric layers of cylinders in the barrel and three disks at the both end-caps designed to provide three precision hits for tracking. It is made up of 1744 modules each covering an area of 16.4 mm × 60.8 mm with 47232 pixel sensors. Each module is equipped with 16 radiation hard readout chips with each individual pixel having its own electronic readout channel resulting in approximately 80.4 million readout channels in total. Each individual pixel covers an area of 50 μm by 400 μm. The nominal operating temperature for the whole system is between 0 °C-20 °C [28]. The pixel system plays an important role in identifying the location of the primary vertex and in b-jet identification.

1.5.2.2. SCT Detector. Similar to the pixel detector, SCT system is also based on silicon technology. It spans the radial distance in between 290-560 mm as measured from the beamline. The barrel region is composed of silicon strips with 80 μm thickness placed on the surfaces of four coaxial cylinders aligned parallel to the magnetic field of the solenoid. Each end cap has nine disks with radially aligned strips of varying thickness. The barrel region covers the pseudo-rapidity region $|\eta| \leq 1.4$ while the end-caps have the acceptance over $1.1 \leq |\eta| \leq 2.5$.

Each SCT module consists of two planes glued with a stereo angle of 10 mrads to yield space-points. Each plane has 768 strip readouts measuring 6 cm in the length, for a total of over 6.3 million. The whole system provides eight precision hits with a spatial resolution of 16 μm in r-ϕ plane and 580 μm along the z-axis. [29]

1.5.2.3. Transition Radiation Tracker. Unlike Pixel and SCT, Transition Radiation Tracker (TRT) consists of many drift tubes called straws with a high voltage anode wire along their axes and the walls acting as the cathode. The straws are filled with Xe,CO_2 and O_2 gas mixture and embedded in plastic fibres and foils to provide a medium for transition radiation to occur. When a charged particle traverses a straw the electrons from the ionized gas is drifted to the central wire. By measuring the drift time of the ionization products, TRT drift circles are drawn. In order to achieve these drift circles, the relation between wire to track distance versus drift time and the anode voltage is carefully profiled. Each straw work as a proportional drift tube. TRT provides 36 drift circles in average for tracking [30].

Asides from tracking, TRT is capable of doing particle identification to a certain extent by studying the ionization profile occurring in the straw tubes. When a relativistic charged particle passes through a discontinuous interface between two different media with plasma frequencies ω_1 and ω_2 the particle may emit radiation. The emitted photon has an energy given by [31] :

$$E = \frac{1}{3}\alpha z^2 \hbar \gamma \omega_p \tag{1.24}$$

$$\omega_p = \sqrt{\omega_2^2 - \omega_1^2} \tag{1.25}$$

Where ω_p is the plasma frequency at the interface, z is the particle's electric charge and $\alpha = \frac{1}{137}$. The transition radiation photon(TR) is absorbed by the special gas mixture inside the straw tube producing more ionization current compared to situations without TR photons. The dependence on γ term implies a mass dependent distinctive transition radiation patterns. TRT is capable of separating electrons from pions to some extent [32].

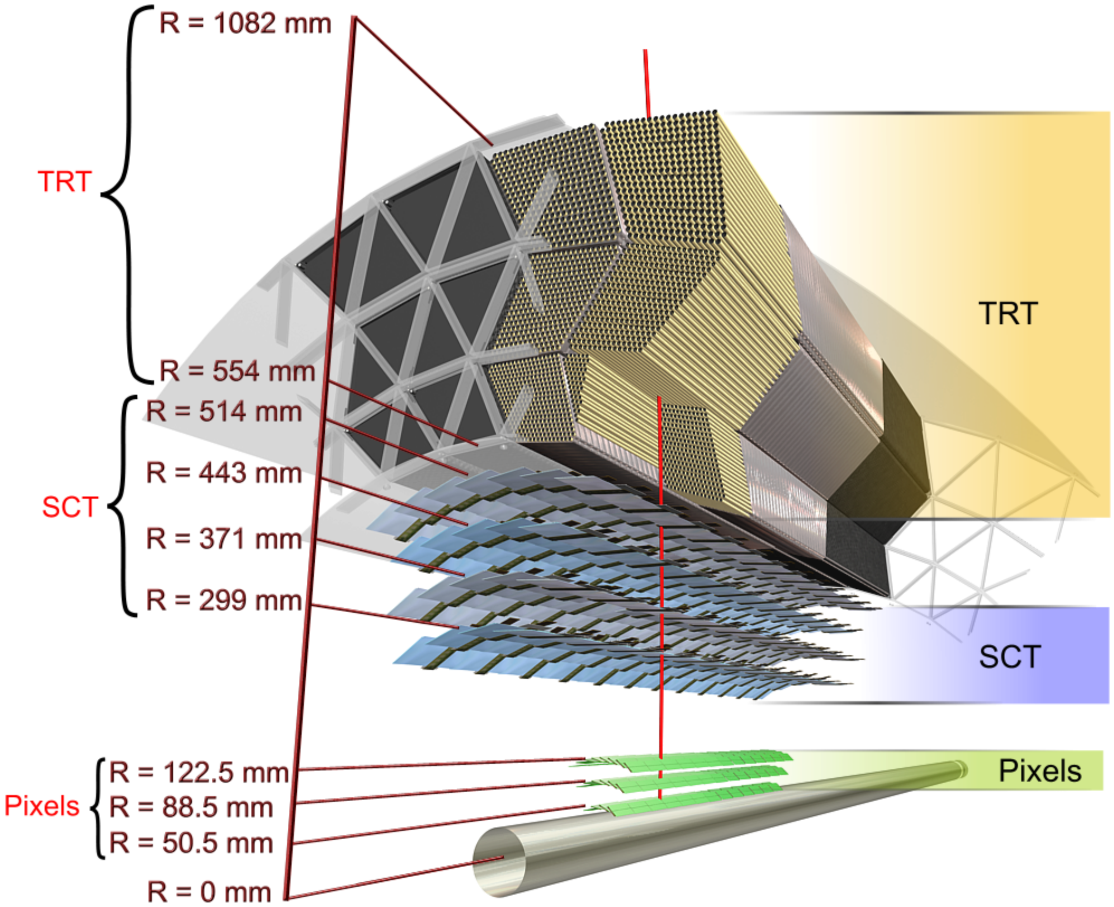

Figure 1.4. A sliced view of barrel region of the inner detector of ATLAS [33].

Similar to the other ID components, TRT has a barrel part with straws aligned parellel to the beamline and two end-cap parts with straws aligned radially. TRT covers the pseudo-rapidity range $|\eta| \leq 2.0$ with spatial resolution of approximately 130 μm.

1.5.3. Calorimetry

The ATLAS has two kinds of calorimeter system covering the entire ID to measure energies of particles. The electromagnetic calorimeter (ECAL) system is designed to measure energies of particles going under electromagnetic interaction such as electrons, photons and charged hadrons. The hadronic calorimeter (HCAL), measures energies of hadrons whether they are neutral or charged.

Each calorimeter system is equipped with alternating layers of absorber and active materials. Many components use liquid argon (LAr) as active medium with tungsten, lead, copper and carbon-steel absorbers. The basic working principle of such sampling calorimeters is that interaction with the absorber creates particle showers which are then detected by the active material. This process continues to happen in the alternating layers until all the energy is dissipated inside showers. The radiation lengths are carefully chosen to avoid particles to punch through and escape the entire calorimeter system. The EM calorimeter is placed closer to the interaction point above the inner detector and is covered by the hadronic calorimeter.

1.5.3.1. Electromagnetic Calorimeter. The electromagnetic calorimeter system consists of lead absorbers and liquid argon acting as active material as seen in Figure 1.5. A high voltage of 2000V is applied in between the absorbers and the electrodes causing a charge drift from the ionization in the liquid argon. This drift time is typically around 450 ns. The electrodes are accordion shaped in order to avoid gaps in the ϕ direction.

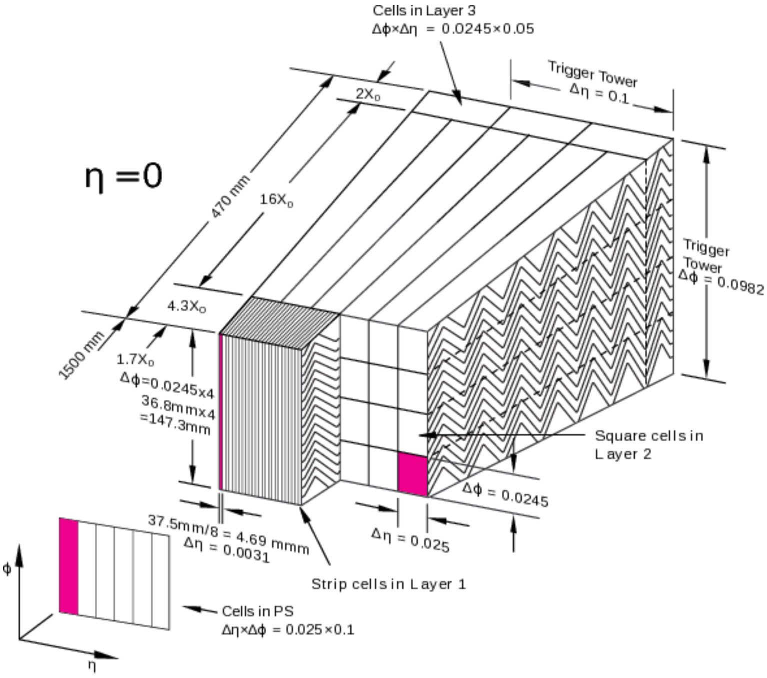

Figure 1.5. A barrel electromagnetic calorimeter module [34].

The electromagnetic calorimeter system provides a full pseudo-rapidity coverage of $|\eta| \leq 3.2$. The barrel part (EMB) spans the region $|\eta| \leq 1.475$ and an end-cap part (EMEC) covering $1.375 \leq |\eta| \leq 3.2$. Barrel and end-caps are placed in their dedicated cryostat. EMB-EMEC transition region $1.37 \leq |\eta| \leq 1.52$ contains a small gap which affects trigger and reconstruction efficiency. A copper-tungsten/liquid argon forward calorimeter (FCal1) provides measurements very close to the beam axis in the region $3.1 \leq |\eta| \leq 4.9$ [34].

1.5.3.2. Hadronic Calorimeter. The hadronic calorimeter system consists of two parts, the tile colorimeter (TileCal) and LAr end-cap (HEC) calorimeter. The tile calorimeter is located outside the EM calorimeter with its central barrel region covering $|\eta| \leq 1.0$ and two barrels on both sides covering $0.8 \leq |\eta| \leq 1.7$. The absorbers are made of carbonized steel while the active materials are built from special scintillating plastic. Wavelength shifting fibers are connected to the tiles converting the scintillation light into a longer wavelength where each fiber is connected to a photo-multiplier tube (PMT).

The hadronic end-cap calorimeter (HEC) is a LAr sampling calorimeter with copper absorbers with the coverage $1.5 \leq |\eta| \leq 3.2$. It has two wheels at each end-cap with planar electrodes instead of accordion shape.

The forward hadronic calorimeter extends to the region $3.1 \leq |\eta| \leq 4.9$ consisting of three modules at each end-cap. As already mentioned, the first module, FCal1 is designed for electromagnetic measurements. The other two, FCal2 and FCal3, has tungsten absorbers that measures forward hadrons [35].

1.5.4. Muon Spectrometer

At the outermost layer, ATLAS implements a large muon spectrometer (MS) to provide fast triggering and high precision tracking. It is designed to measure a wide range of muons with momenta from a few GeV up to 3 TeV. The momentum resolution is typically around 10% for a muon with transverse momentum of 1 TeV.

Placed inside the magnetic field generated by the toroid system, MS consists of four types of modules. The monitored drift tubes (MDT) and cathodes strip chambers (CSC) provide precise tracking within the range $|\eta| \leq 2.7$ working as proportional drift chambers. In the innermost layer, within $2.0 \leq |\eta| \leq 2.7$, CSC is used for tracking in order to cope with high occupancies because CSCs have faster counting rates than MDTs.

The resistive plate chambers (RPC) and thin gap chambers (TGC) with high-rate capabilities and fast time resolutions are designed to deliver fast signals for muon triggering in the barrel and end-caps respectively.

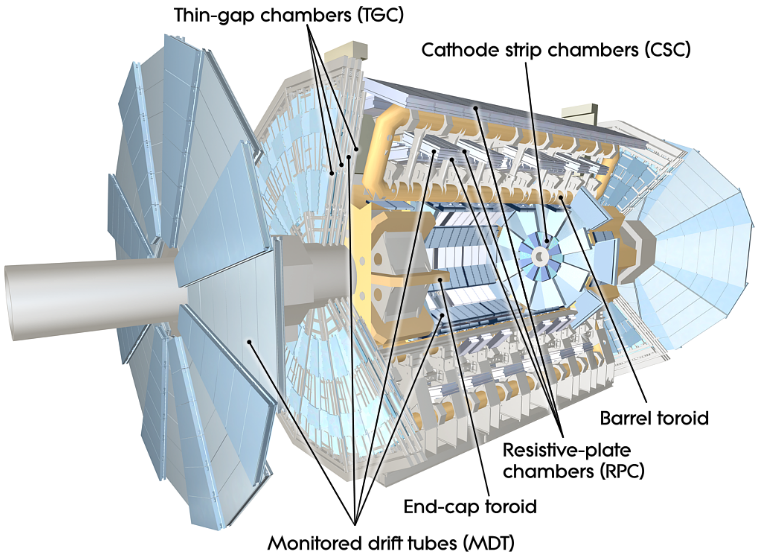

Figure 1.6. Layout of the ATLAS muon system [36].

1.5.5. Magnet System

<u>1.5.5.1. Solenoid.</u> The solenoid magnet provides a uniform magnetic field for the entire volume of the tracker system for momentum measurement. It has a length of 5.3 meters and thickness of 4.5 centimeters with a weight of approximately of 5 tonnes. When operated at the nominal values the solenoid provides a 2 T of uniform magnetic field with currents of 7.73 kA storing energy of 38 MJ in the magnetic field.

1.5.5.2. Toroid. The toroid system has a barrel and two end-caps. Each part is equipped with eight coils aligned along the radial direction symmetrically. Each individual coil in the barrel is placed in their own cryostat operating at 4.7 K temperature. The coils at the two end-caps share a single cryo-stat. The field strength is 3.9 T at the center and grows to 4.1 T in the forward region. The coils are winded from Al/NbTi/Cu superconducting cables. The barrel stores 1.08 GJ of magnetic energy while each end-cap stores 0.25 GJ with each coil circulating 20.5 kA of current [37].

1.5.6. Trigger and Data Acquisition System

When operating at its maximum design capacity, the LHC would produce collision data in unmanageable rates with ~100 TB/s at 40 MHz frequency [38]. The ATLAS experiment implements a three level trigger and data acquisition (TDAQ) system to select most interesting events for physics studies while providing a decent bandwidth to record selected events on the permanent storage. A schematic diagram of ATLAS TDAQ is depicted in Figure 1.7.

The level 1 trigger(LVL1) is a hardware-based system using information from the muon chambers and the calorimeters. It basically selects high-p_{T} muons, electrons, photons, jets, hadronically decaying tau leptons and large missing transverse energy (MET). A LVL1 decision is made within the first few μs of the bunch crossing. To perform this fast, the LVL1 system identifies the geographical coordinates of the detector with significant calorimeter clusters and muon tracks keeping the full event information in read-out buffers. These coordinates, so called regions of interest (RoI), are then passed to the level-2 (LVL2) system at a rate of 75 kHz.

The LVL2 system is software based and seeded by the RoI information provided by the LVL1. It has access to the partial event information from the detector components only located in the RoI. The system works on a large computer farm with thousands of CPU cores. High level trigger (HLT) algorithms reconstruct the partial event and the related objects while doing compatibility checks to decide whether the event survives or not. The surviving event fragments are fully collected and passed to the level-3

(LVL3) at the rate of approximately 3 kHz.

The LVL3 acts as an event filter (EF) and reconstructs the whole event using the full detector information which was not accessible by the LVL2 due to time constraints. The EF utilizes off-line reconstruction and analysis algorithms such as missing transverse energy calculation, vertex reconstruction, track fitting and isolation. The rate of events is reduced to ~100 Hz. Depending on the satisfied trigger(s), the surviving event is recorded onto the permanent storage in jet, e/γ, tau, muon and E^T_{miss} data streams in parallel. The data sample used in this dissertation is recorded by e/γ and muon streams to obtain enriched samples containing $Z \to ee$ and $Z \to \mu\mu$ events.

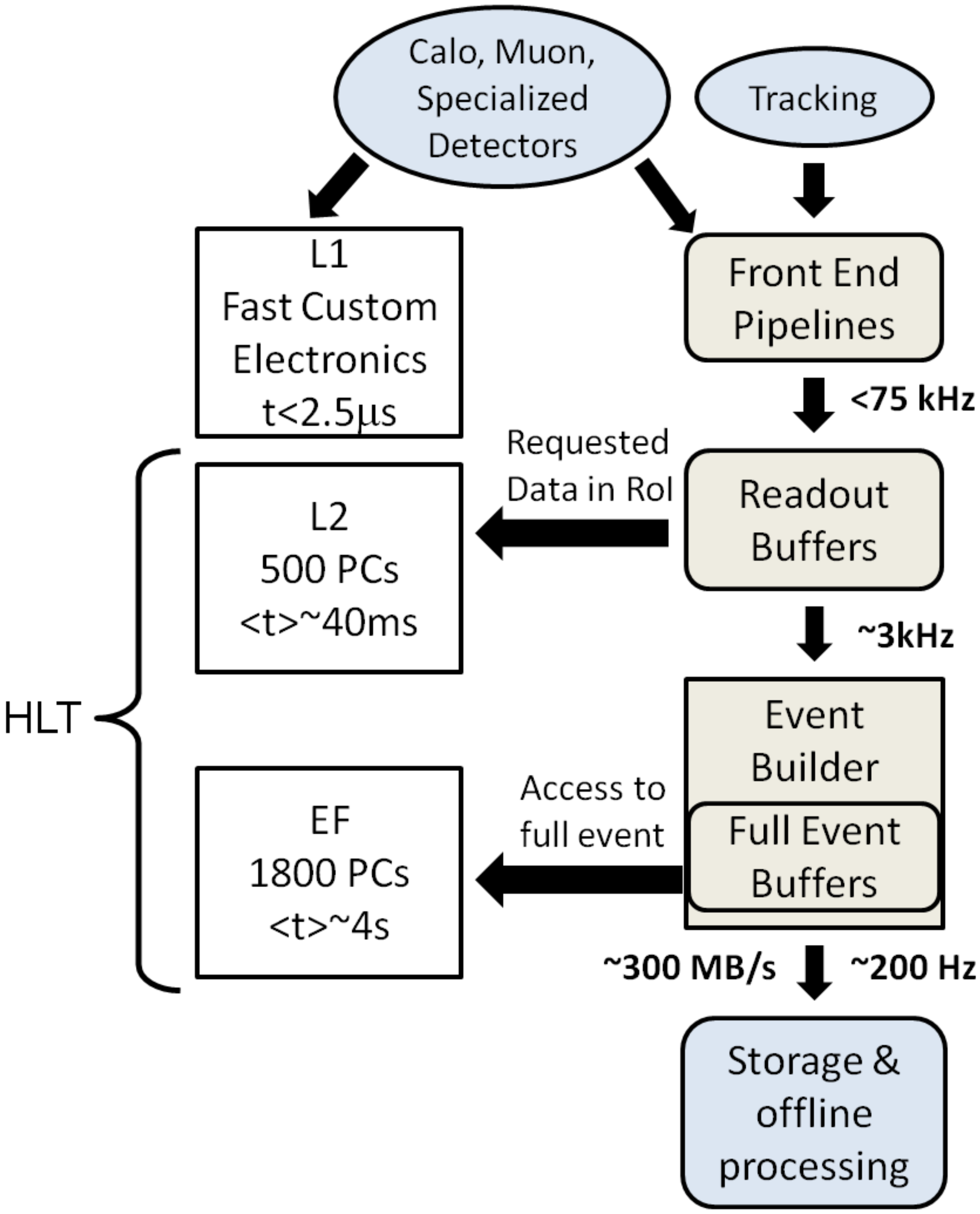

Figure 1.7. Schematic of the ATLAS trigger system [39].

2. HEAVY QUARK ANALYSIS

2.1. Analysis Strategy

Heavy quark production at the LHC energy regime is dominated by QCD processes. The cross section of possible new heavy quarks can easily be calculated by pQCD calculations. The pair production cross sections used in this analysis are obtained from a pQCD cross section calculator TOP++ at next to leading order (NLO) [40]. Various Feynman diagrams related to D quark pair production are shown below.:

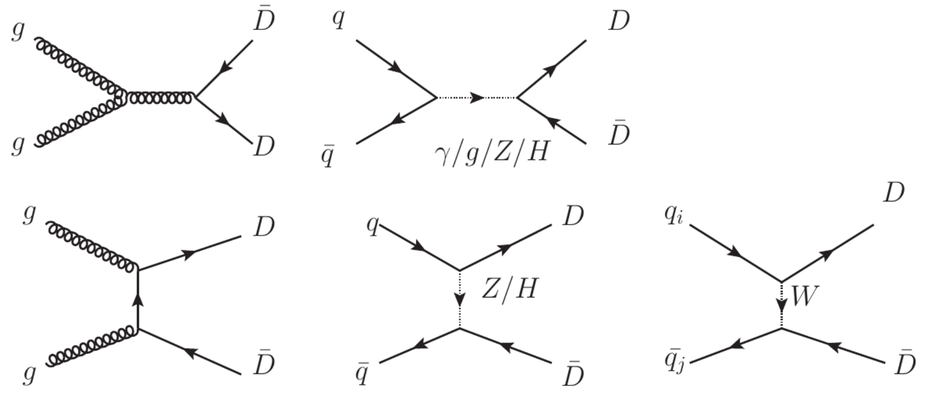

Figure 2.1. Leading order D quark production at the LHC.

This search aims to observe final states in which one of the pair produced heavy quarks decay into a Z boson and the other one into a $W^{\pm}$ or Z with the associated light generation prompt jets (u,d). We also impose the requirement that if the final state includes more than one Z boson, only one of them decays into a lepton pair while the other one decays into hadrons. Furthermore, in order to stay orthogonal to the other heavy quark searches where coupling to only 3rd generation is present [41], our final selection includes a b-jet veto which is also necessary for staying orthogonal to the final states with the Higgs boson. Orthogonality of individual searches are kept as maximum as possible at ATLAS and such collaborations to avoid overlaps in between different analyses so that in case of any observation or discovery, it would be easier to assign the phenomena a meaning within a theoretical framework.

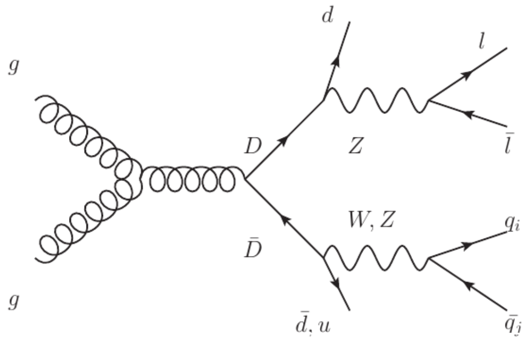

Figure 2.2. A pair of D quarks produced via gluon-gluon fusion and the resulting final state.

The search is carried in two distinct channels e^+e^- and $\mu^+\mu^-$, named after the lepton pairs of interest by which the leptonic Z boson is reconstructed. There is no dedicated τ channel since τ lepton is unstable and decays mostly into pions. However $Z \rightarrow \tau\tau$ cases slightly contribute to e^+e^- and $\mu^+\mu^-$ channels via the leptonic decays of τ.

2.2. Data Sample

The data sample used in this analysis correspond to 20.3 of fb^{-1} integrated luminosity at $\sqrt{s}$=8 TeV center of mass energy collected during the 2012 p-p collisions. The whole dataset consist of ten data taking periods labeled by capital letters A-L as shown in Table 2.1. Each data taking period consists of small luminosity blocks of two minutes of bunch crossings synchronized with the LHC clock. To ensure a good data quality, luminosity blocks with one or more malfunctioning detector components are masked out from the data set at the offline level. The integrated luminosity is then calculated according to the list of good luminosity blocks provided by the ATLAS Collaboration.

As our signal events would have leptonic signatures in the detector, we have used

Table 2.1. Individual data taking periods and their corresponding integrated luminosities before bad lumi-blocks have been filtered out.

Period	Dates (2012)	Integrated Luminosity (fb^{-1})
A	April 04 - April 20	0.91
B	May 01 - June 18	5.59
C	July 01 - July 24	1.64
D	July 24 - August 23	3.60
E	August 23 - September 17	2.86
G	September 26 - October 8	1.40
H	October 13 - October 26	1.65
I	October 26 - November 02	1.15
J	November 02 - November 26	2.94
L	November 30 - December 06	0.98
Total	—	22.7

two separate datasets recorded by single electron and muon triggers, e/γ and muon streams respectively. Both e/γ and muon trigger signals consist of the logical OR operation of a high p_{T} threshold trigger without an isolation criteria and a lower p_{T} one with isolation requirements. Triggers used to record e/γ stream were `EF_e24vhi_medium1 OR EF_e60_medium1` and `EF_mu24i_tight OR EF_mu36_tight` for the muon stream.

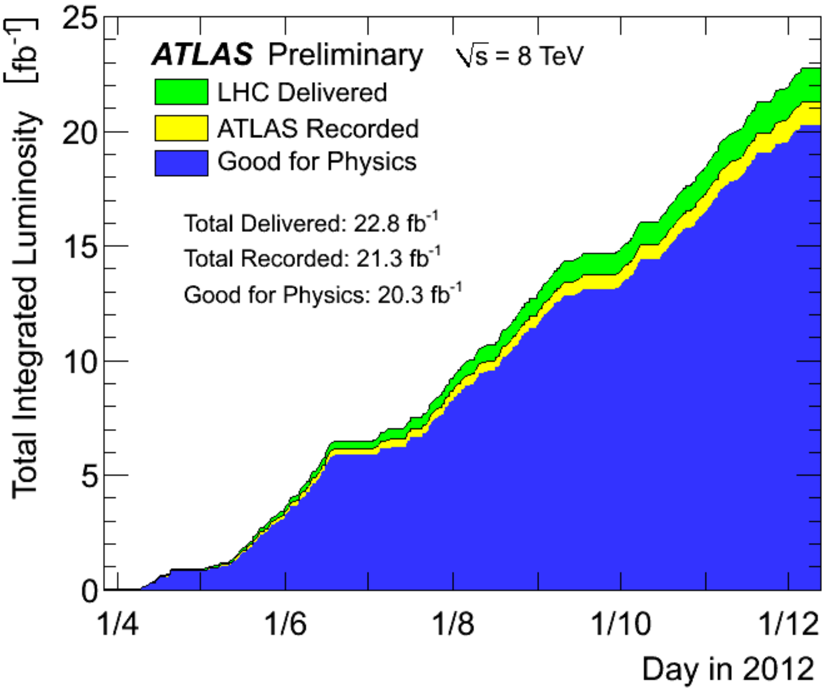

Figure 2.3. Integrated luminosity versus time during stable beams and for pp collisions at 8 TeV centre-of-mass energy in 2012 [24].

2.3. Simulated Samples

All the background and signal events are modelled by simulated data in this search. Background events have been created with various event generators by the ATLAS Collaboration and passed through the detector simulations to create sensor hits and energy deposits inside the detector material. These sensor hits are processed through the trigger and digitization steps to obtain digitized sensor hits. Finally the physics objects such as electrons, muons, jets and missing transverse energy are obtained by reconstructing these digitized data with the same algorithms used for real data taking. Any real world effect is reflected in the detector simulation such as problematic modules and dead material distribution within the detector. Effects of pile-up are mimicked by overlaying sensors hits from minimum bias simulation events during the digitization step. [1]

---

[1] Unlike hard scattering events that are interesting for physics studies, minimum bias events correspond to low p_T events in highly luminous LHC environment and mostly consist of inelastic scatterings.

The main challenge in this computational chain is the detector simulation which is carried out by the GEANT4 [42] implementation of the ATLAS detector. This is a very CPU intensive task with several minutes of processing time per event. Time consuming part is the shower formation while energetic particles pass through the calorimeter.

For this reason another detector simulation package called ATLFAST2 [43] is also utilized while obtaining simulation samples. In ATLFAST2 calorimeter part of the simulation is parametrized instead of fully simulating particle showers there. This drastically reduces event processing time in exchange of loosing some details of information from the calorimeter cells. The rest of ATLFAST2 simulation in the inner detector is exactly the same as in full GEANT4. Figure 2.4 shows the improvement in timing performance.

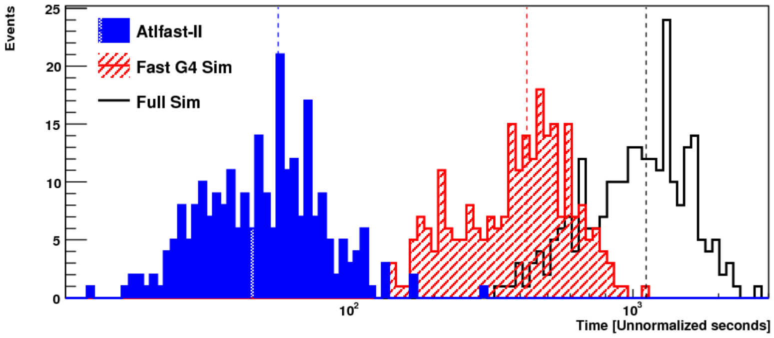

Figure 2.4. Event processing times for ATLFAST2 and Full GEANT4 simulations [27].

2.3.1. Background Samples

Due to the large cross section and sharp $m_{l\bar{l}}$ peak, the major SM background contribution comes from Z bosons produced in association with jets. This is followed by top quark pairs ($t\bar{t}$) and dibosons ($W^{\pm}W^{\mp}$,$W^{\pm}Z$,ZZ) produced in association with jets. A small fraction of background contribution is due to $t\bar{t}$+$W^{\pm}/Z$, $t+Z$, and single top quark events. In addition to these we have taken contributions from W+jets into

---

As its name speaks for itself, minimum bias events are recorded with specialized triggers with minimal set of selection requirements account since these processes have very large cross sections and some portion of such events are likely to pass through our event selection when combined with non-prompt leptons.

The following Figure 2.5 indicates only a few of the production mechanism for a single Z boson produced together with various number of jets at the LHC. It is important to state that large numbers of jets in the final state can be obtained when initial or final state quarks radiate additional gluons.

We have used two separate Z+jets background samples produced by different event generators in order to cross check modelling of this overwhelming background throughout the analysis. These have been produced with ALPGEN v2.13 [44] and SHERPA v1.41 [45] generators with two different Parton Distribution Function (PDF) set and slightly different truth level cuts. Each sample consists of several sub-samples where Z boson decays into the three lepton flavors.

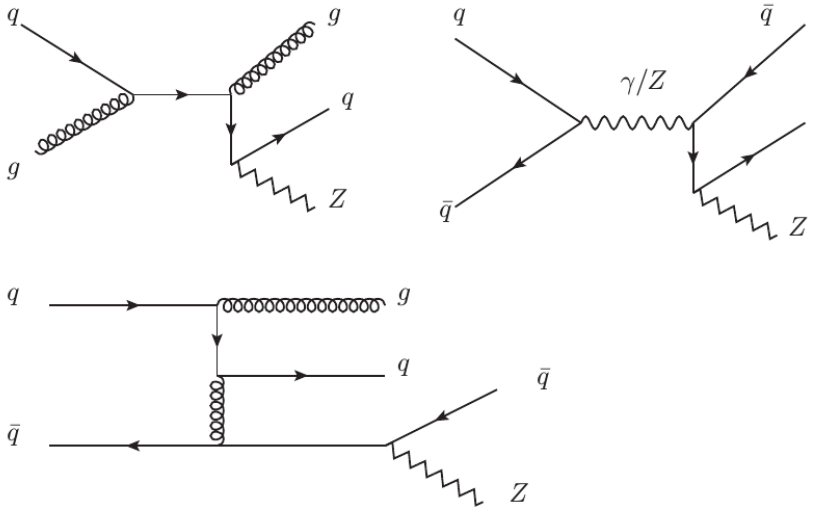

Figure 2.5. Some of the Z+jets production mechanisms at p-p collisions.

ALPGEN samples were produced with CTEQ6L1 [46] PDF set and interfaced to Pythia v6.426 [47] generator for parton showering and hadronization. A requirement on dilepton invariant mass $m_{l\bar{l}} \geq 40$ GeV is imposed at the generator level. It is a combination of three sub-samples categorized by their heavy flavor compositions. The first ALPGEN sub-sample consists no heavy flavor jets in the matrix element but c and b flavors may only arise in further time evolution during the parton showering. The other remaining two samples are simply Z+$b\bar{b}$+jets and Z+$c\bar{c}$+jets generated with heavy flavors at the matrix level. The overlap between these ALPGEN sub-samples are removed by exploiting the distinct kinematics of final state particles resulting from matrix element and parton showering. Particles created during the parton showering tend to be collinear while the reverse is true for the matrix element particles. The same heavy flavor overlap removal procedure in [48] classifies each type of event thus preventing multiple counting of the same Feynmann diagrams present in each sub-sample.

Table 2.2. List of all simulated backgrounds used in this analysis and their corresponding cross sections.

Sample	Event Generator	Detector Simulation	Cross Section [pb]
Z+jets	Sherpa	ATLFAST2+FULL SIM	3843.03
Z+jets	Alpgen	FULL SIM	3576.00
$t\bar{t}$	Powheg	FULL SIM	137.32
dibosons	Sherpa	FULL SIM	56.93
single top	MC@NLO	FULL SIM	52.62
t+Z	MadGraph	FULL SIM	0.04
$t\bar{t}+W^{\pm}/Z$	Alpgen	FULL SIM	0.11
$W^{\pm}$+jets	Alpgen	FULL SIM	38574.53

SHERPA Z+jets sample were produced with CT10 [49] PDF set with dilepton invariant mass cut $m_{l\bar{l}} \geq 60$ GeV. It is also categorized with respect to its c and b flavor compositions. Each category consists of non-overlapping filtered events at the hadron level which are dubbed as BFilter-CFilter, CFilter-BVeto and CVeto-BVeto.

These samples were produced inclusively and sliced in different bins of $p_{\mathrm{T}}(Z)$ to keep statistics high at large transverse momenta. Sliced $p_{\mathrm{T}}(Z)$ regions are [70-140], [140-280], [280-500] and [500+] GeV. We removed the overlap between sliced and inclusive SHERPA samples by rejecting all the events with $p_{\mathrm{T}}(Z) \leq 70$ GeV at the truth level in the inclusive sample. The highest momentum slices have been processed by the full simulation while the others were obtained by ATLFAST2.

In addition to these samples, another SHERPA Z+jets sample prepared with MENLOPS [50] prescription with NLO accuracy at the matrix element, has been used as well. However as this sample have massless c and b quarks implemented, we do not use it throughout the analysis. This sample is expected to have more realistic kinematic distributions for variables such as $p_{\mathrm{T}}(Z)$ and thus used to compare variables related to the Z boson with the main samples described above.

$t\bar{t}$ background samples are produced with POWHEG [51] using CT10 PDF set interfaced to Pythia v6.421 for hadronization and parton showering. $t + Z$ background events are generated by MADGRAPH [52] interfaced to Pythia. MC@NLO [53] is used to obtain background events contributed by single top quark production. The same ALPGEN Z+jets prescriptions are used while obtaining W+jets simulation samples.

2.3.2. Signal Samples

Our signal samples consist of six heavy quark mass points ranging from 300 GeV to 800 GeV in steps of 100 GeV. Signal events have been privately produced with CompHEP v4.5.1 [54] event generator at leading order with the model Lagrangian in equations 1.16 and 1.17 implemented. CTEQ6L1 PDF set is used and the QCD scale is set to the heavy quark mass while producing the signal events. The remaining steps of the simulation have been carried out using the official ATLAS Collaboration tools. CompHEP events are then interfaced to Pythia v8.165 for parton showering and hadronization. These events are finally processed by ATLFAST2 detector simulation. A single lepton filter is utilized with lepton cuts of $|\eta| \leq 2.7$ and $p_{\mathrm{T}} \geq 15$ GeV at the truth level to increase the statistics of surviving events after our di-lepton criteria is met. Even though leptonic decay modes of one Z boson produced by heavy quark decays are of interest in this search, the signal samples are inclusive in terms of the decay modes of vector and Higgs bosons to include contributions from events from the other decay modes as well.

Signal $D\bar{D}$ events have been generated with all six decay modes $D \to Wq$, $D \to Zq$, $D \to Hq$ in equal numbers such that any set of branching ratios can be chosen from truth information in order to make model independent studies. For example, in the chiral model BR($D \to Wq$)=100%. However E_6 model predicts BR($D \to Wq$)=50% and BR($D \to Zq$)=0.25% at large mass as shown in Figure 2.6. For the rest of this thesis, expectations from signal events corresponding to m_D=600 GeV with BR($D \to Zq$)=100% are shown in the figures and tables unless stated otherwise.

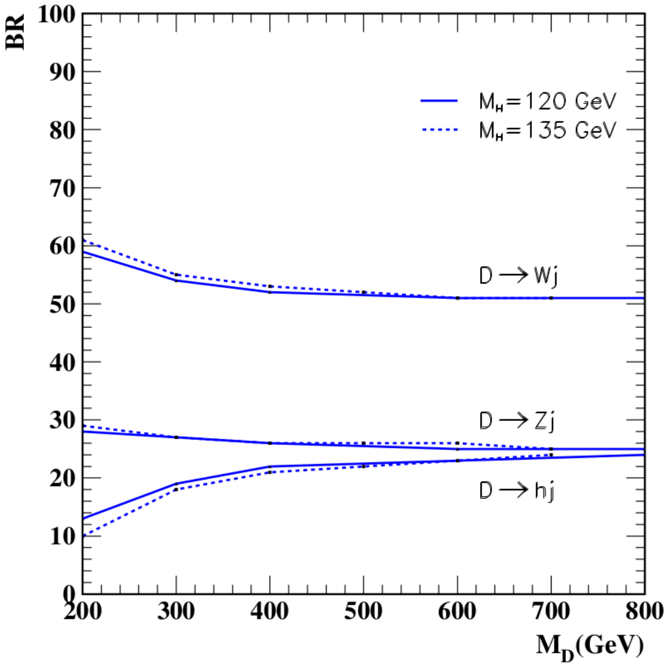

Figure 2.6. D quark branching ratio as predicted by E_6 iso-singlet model [19].

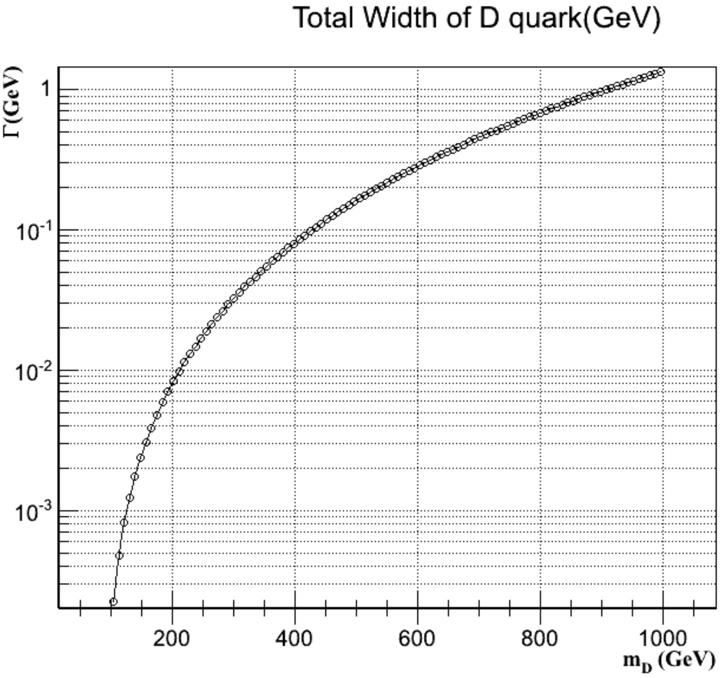

Figure 2.7. D quark width as a function of its mass.

2.4. Reconstructed Physics Objects

The relevant physics objects in this study are electrons, muons and jets. These objects are characterized and measured by various performance groups in the ATLAS Collaboration. To fulfill the needs of a large variety of physics studies, these objects are serviced with different aspects in a common task-force. In other words, the defining properties of these physics objects vary according to the target physics search. We have used object definitions from the Top Physics Working Group as our aimed signal loosely resembles the $t\bar{t}$ final state.

2.4.1. Tracks and Vertices

Charged particles leave tracks within the different layers of the inner detector and the muon spectrometer. While these tracks mainly provide momentum measurement of charged particles bent by the $\vec{B}$ fields inside the solenoid covering the ID and the toroid of the MS, the tracks segments within the TRT layer also contribute to the identification of charged particles, especially separation of electrons from pions. Identification of b-jets rely on reconstructed non-primary vertices and tracks inside the jets

Due to very large charged particle multiplicities in high luminosity collision environments, tracking is a complex and challenging task and requires extensively granular sensors around the interaction point. Pixel and SCT sensors provide very precise hits close to the interaction point providing the seeds to reconstruct tracks. These seeds are then extrapolated to the outer layers of SCT to form track candidates. After satisfying various quality criteria the track candidates are then associated to TRT drift circles. A final track fitting is done using the full information from all ID components. High performance pattern recognition algorithms are implemented to fulfill the needs for fast track-fitting in a high occupancy environment [55].

Primary vertex finding is carried out by assigning tracks to the vertex candidates, and then vertex finding algorithm calculates the positions of the primary vertices and their corresponding error matrices [56].

2.4.2. Electrons

Electrons are reconstructed by matching an inner detector track to an energy deposition inside the electromagnetic calorimeter. First of all, local calorimeter energy depositions are clustered and summed to calculate the total energy. These energies are then calibrated to account for leakages outside the reconstructed cluster while compensating for the losses due to the dead material within the calorimeter.

A cluster is formed around a seed whose position is calculated by a sliding window algorithm where a rectangular region in $\eta - \phi$ plane is moved around to find the local maximum of an energy deposition. If the seed is matched to an inner detector track with p_{T} $\geq$5 GeV the electron candidate is formed. The calculated track is extrapolated from its last measured points to the middle layer of the electromagnetic calorimeter. If the extrapolated track η and ϕ coordinates are close to the cluster seed in that layer by $|\Delta\eta|$ $\leq$0.05 the track is associated to that cluster. The matched track should have a decent longitudinal impact parameter $|z_0| \leq 2$ mm with respect to the primary vertex.

Electron candidates are required to have $E_{\mathrm{T}}^{(cluster)} \geq 25$ GeV for optimal trigger efficiency and $|\eta_{cluster}| \leq 2.47$ to fall inside the calorimeter acceptance. In addition to this, due to the transition region between the barrel and the end-cap calorimeter, electron candidates with $1.37 \leq |\eta_{cluster}| \leq 1.52$ were excluded.

Besides all these, electron candidates should satisfy the `medium++` requirements which make use of additional calorimeter and track parameters as described in the reference study [57]. No track or calorimeter isolation is imposed in order to keep the efficiency high as our analysis requires two electrons. The electrons defined here have reconstructed by `Electron/Gamma` performance group. The $r-\phi$ display of an example event with four electrons can be seen in Figure 2.8.

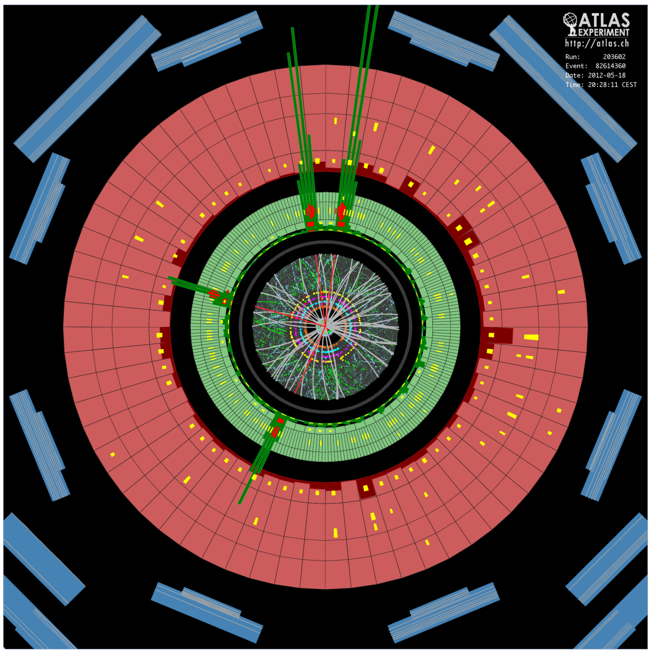

Figure 2.8. A candidate $H \to ZZ \to 4e$ event recorded in 2012 $\sqrt{s}$=8 TeV p-p collisions. The invariant mass of the 4 electron system is 124.5 GeV. Reconstructed Z boson masses are 70.6 GeV and 44.7 GeV. Calorimeter clusters are colored in green while the associated tracks and the calorimeter seeds are colored in red [58].

2.4.3. Muons

Muons leave tracks in the Inner Detector and in the Muon Spectrometer not interacting much with the calorimeter layers. Thanks to the muon spectrometer, ATLAS provides more precise momentum measurements of muons than that of the electrons. Independently reconstructed tracks from the muon spectrometer are matched to the tracks in the inner detector to obtain combined muon candidates. These candidates are then re-fitted using the complete tracking information.

To follow up with the optimal trigger efficiency, reconstructed muons should have $p_{\mathrm{T}} \geq 25$ GeV. Due to the finite detector coverage, they should fall in the pseudo-rapidity region $|\eta| \leq 2.5$. The muon spectrometer has limited number of components around the coordinate $\eta \approx 0$ in order to provide a service space for the inner detector and the other parts of the detector. This space causes some loss of efficiency around that point.

The muons used in this analysis have tight quality criteria in terms of track quality and calorimeter isolation [59]. Tracks in the inner detector should have at least 1 silicon pixel hit and at least 5 SCT hits. The number of dead SCT+pixel hits should not be more than 3. Inside the pseudo-rapidity region $0.1 \leq |\eta| \leq 1.9$, the number of TRT hits+outliers should at least be 9. In addition to these, similar to the electrons, the reconstructed muon track should have a proper longitudinal impact parameter with respect to the primary vertex ensuring that $|z_0| \leq 2$mm.

A track based p_{T} dependent isolation procedure has been used to reduce rate of fake mouns and muons from secondary interactions under high luminosity conditions. The scalar sum of the tracks' p_{T} inside a cone of $\Delta R \leq$ (10 GeV/ $p_{\mathrm{T}}^{(\mu)}$) around the reconstructed muon should be less than 5% of the muon's p_{T}. The display of an example event with an electron and a muon is shown in Figure 2.9.

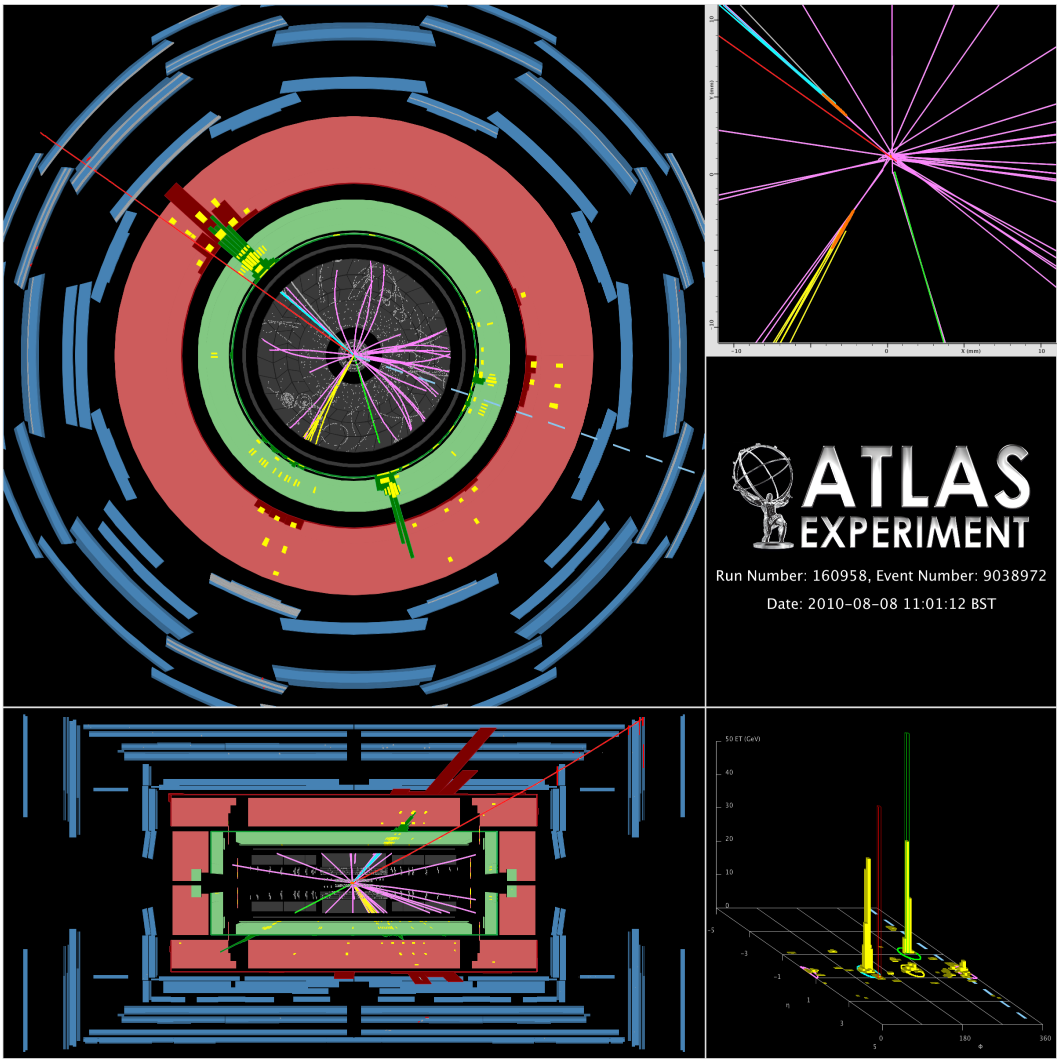

Figure 2.9. Event display of a top pair e- μ dilepton candidate with two b-tagged jets. The electron is shown by the green track pointing to a calorimeter cluster, the muon by the long red track intersecting the muon chambers, and the missing ET direction by the dotted line on the XY view. The secondary vertices of the two b-tagged jets are indicated by the orange ellipses on the zoomed vertex region view [58].

2.4.4. Jets

Jets are the experimental signatures of final state quarks and gluons produced in high energy collisions. Due to the color confinement in QCD, no free colored states can exist thus it is not possible to directly observe colored final state particles in the detector. They undergo parton showering and hadronization producing color singlet final states with large particle multiplicity which are then detected by the experiment as jets.

While the final state quark or gluon propagates in the vacuum, it emits a gluon which will in turn radiate $q\bar{q}$ pairs collinear with its parent parton and so on. As the the showering process creates lower energy partons, it will stop when non-perturbative region of QCD is reached. Finally, newly created colored states combine to form color singlet bound states during the hadronization phase forming the jets.

Jets consist of a large number of neutral or charged hadrons leaving many tracks inside the inner detector and deposit their energy to the electromagnetic and hadronic calorimeters. They are reconstructed from calibrated topological clusters formed by calorimeter energy depositions by the anti-k_t recombination algorithm [60] with radius parameter of ΔR=0.4. Prior to jet finding, calorimeter clusters are calibrated with the Local Cluster Weighting method [61] in order to compensate for shower energy losses inside inactive material and leakages outside the energy clusters. The set of calibrated clusters with non-negative energies are then fed into anti-k_t algorithm as massless particles to yield the reconstructed jets. The four momentum of the resulting jets are basically the sum of the four momenta of its constituent clusters. Finally, the jet energy and pseudo-rapidities are calibrated using Monte-Carlo based methods.

For this analysis, the calibrated jets are required to have p_{T} $\geq$25 GeV and $|\eta|$ $\leq$2.5. Jets from secondary interactions and pile-up effects are reduced by applying a cut on the jet vertex fraction (JVF). That is, for the jets with p_{T} $\leq$50 GeV, scalar p_{T} sum of all the tracks inside the reconstructed jet must at least be 50% of that of the tracks originating from the primary vertex.

Jet reconstruction procedure does not distinguish single electrons from a jet. To remove this overlap, if there are any jets in the neighborhood of a reconstructed electron within a cone of ΔR $\leq$0.2, the jet closest to the electron is removed from the event. After the completion of this procedure, if there are any electrons left around a jet inside a cone of ΔR=0.4, they are removed from the event to avoid double counting of electrons from hadrons decaying inside the jets.

2.4.5. *b*-Jet Identification

B-jets are crucial in our analysis because our final event selection involves b-jet veto. The typical characteristics of jets originating from *b*-quarks are the displaced tracks and vertices inside the jet as B-hadrons have long enough lifetime to have a detectable flight path before they decay. ATLAS uses a neural network based algorithm [62] utilizing the information from impact parameters of displaced tracks and non-primary vertices within the jet. *b*-tagging is carried out by the so called MV1 algorithm at its 70% operating point with light jet rejection factor of ≈130 and charm rejection factor of 5.

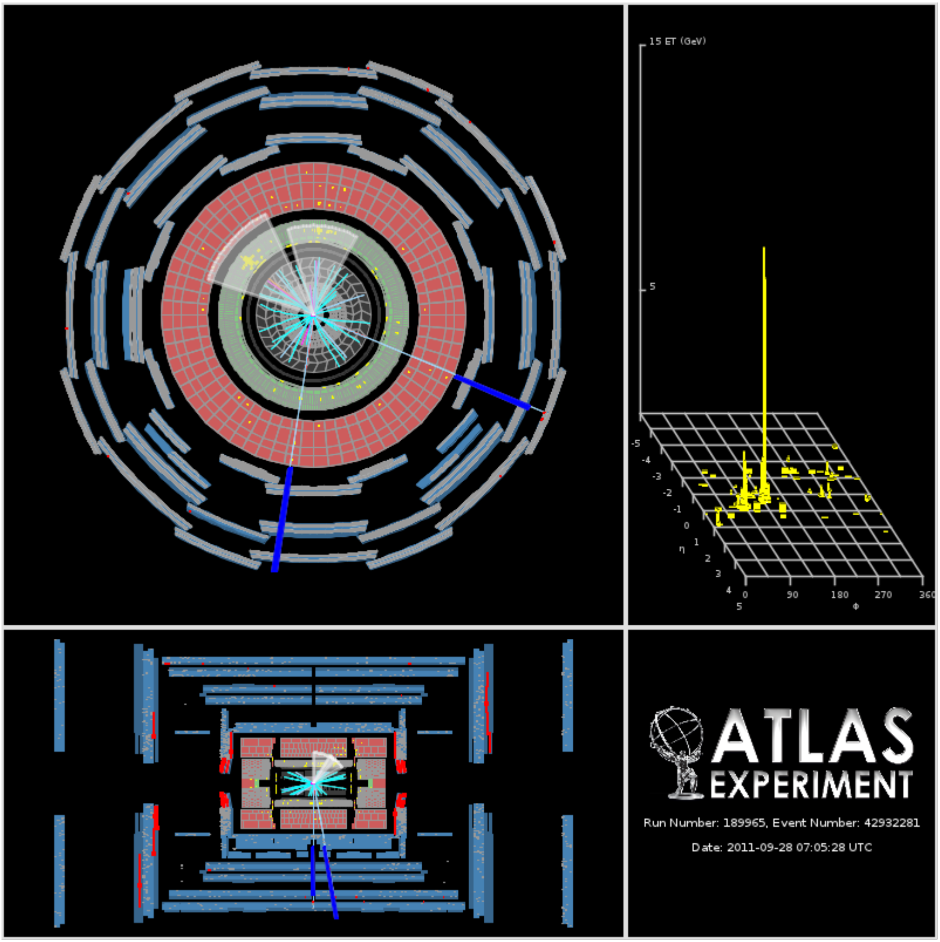

Figure 2.10. Event display of a candidate $H \to ZZ \to \mu\bar{\mu} + b\bar{b}$ event. B-jets are shown in grey cones while the muons are in blue. Invariant mass of $\mu\bar{\mu}b\bar{b}$ system is 332 GeV [58].

2.5. Event Selection, Definition of Signal and Control Regions

2.5.1. Event Pre-Selection

Once all the reconstructed physics objects satisfy the quality criteria already mentioned, we proceed by applying pre-selection cuts to reduce the enormous amount of data while eliminating some background events. The pre-selection requirements are summarized below.

2.5.1.1. Trigger requirements. The event should fire a single electron or muon trigger. In order to remove a possible overlap between e/γ and muon streams, we impose an orthogonal trigger requirements for both streams. Events from the muon stream are allowed to fire an electron or muon trigger but we remove events from e/γ streams which fired the muon trigger.

2.5.1.2. Exactly two lepton requirement. Surviving events should contain exactly one pair of leptons of the same flavor but with opposite sign of electric charge (OSSF). One of the reconstructed leptons should match to the triggering lepton with the criteria $\Delta R \leq$1.5

2.5.1.3. Primary Vertex. Events should have at least one primary vertex with at least five tracks. In multiple reconstructed primary vertex cases, the one with the highest scalar tracks' p_{T} sum is selected.

2.5.2. Control and Signal Regions

After pre-selection requirements, leptonic Z boson is reconstructed by adding the four momenta of the OSSF lepton pair. The invariant mass of the combination is required to fall into the mass window $|m_{l\bar{l}} - m_Z| \leq 10$ GeV. By satisfying all these requirements we obtain an inclusive Z boson sample whose subsets are going to be our signal and control samples.

Furthermore, we proceed further by requiring at least 4 jets so that the event topology is matched to that of a signal event. However Z+jets background is still dominating at this stage. In signal events, emerging from two massive quarks, the decay products are expected to have very large transverse momenta in contrast to the Z+jets events. so we impose additional kinematical cuts on the variables H_T and $p_\mathrm{T}(Z)$ to proceed with the signal region.

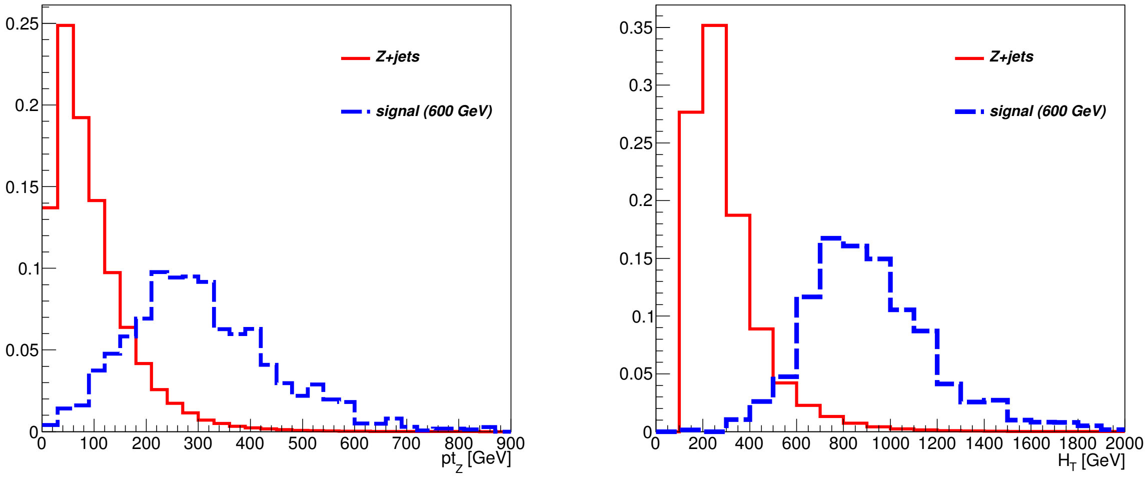

(a) (b)

Figure 2.11. Comparison of the discriminating variables $p_\mathrm{T}(Z)$ and H_T for the simulated signal at 600GeV and Z+jets after requiring at least 4 jets. Distributions are normalized to unity.

In the above distributions shown in Figure 2.11, we have defined $H_\mathrm{T} = \sum_i \left|p_\mathrm{T}^{(i)}\right|$ where the index i runs over all jets in the event. After requiring at least 4 jets we apply cuts $p_\mathrm{T}(Z) \geq$150 GeV and $H_\mathrm{T} \geq$ 600 GeV. Finally we run a reconstruction algorithm based on χ^2 minimization. The algorithm takes jets and the Z boson as inputs and assign jets to reconstruct $D\bar{D}$ pair 4 momenta separately. The $D\bar{D}$ combination which yields the minima of the following χ^2 function is chosen.

$$\chi^2 = \frac{(m_{q\bar{q}} - m_V)^2}{\Gamma_V^2} + 2\frac{(m_D - m_{\bar{D}})^2}{\Gamma_D \Gamma_{\bar{D}}} \tag{2.1}$$

The parameters Γ_V,Γ_D,$\Gamma_{\bar{D}}$ are the reconstructed mass widths and are estimated from simulations. V stands for the hadronically reconstructed $W^{\pm}$ or Z boson and m_V is taken to be $\frac{1}{2}(M_W + M_Z)$.

Since the reconstruction algorithm carries out minimization there is always a possibility to obtain fake minima. To reduce this effect, we impose some additional jet requirements at each iteration while going through all possible $D\bar{D}$ configurations. What we require is the following:

$$\begin{aligned} p_{\mathrm{T}}(jets) &\geq 50 \text{ GeV} \\ \Delta R(V, jet) &\geq 1.75 \\ \Delta R(Z, jet) &\geq 1.75 \end{aligned} \tag{2.2}$$

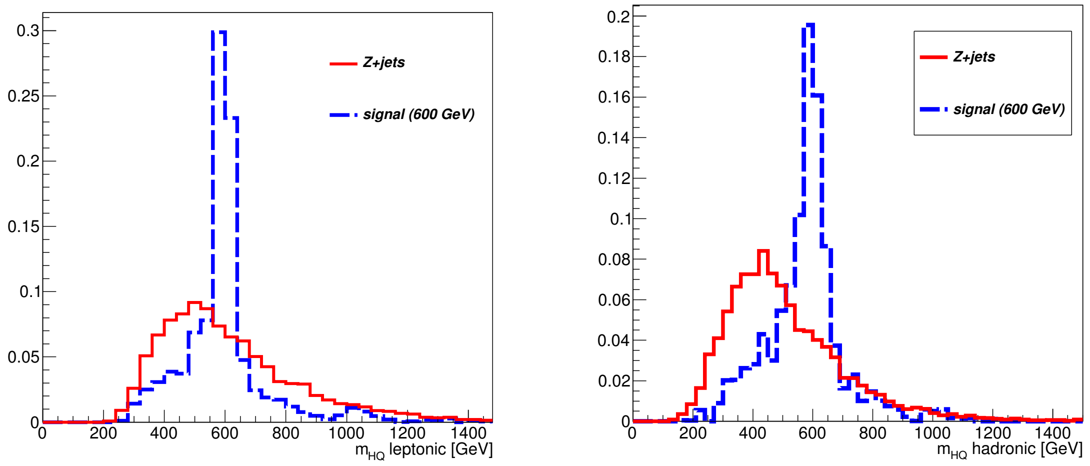

(a)

(b)

Figure 2.12. Leptonically(a) and hadronically(b) reconstructed D quark masses as discriminating variables for the signal and the Z+jets background. Distributions are normalized to unity. Distributions are obtained from simulations.

The phase space requirements in equation 2.2 implies that efficiency of the reconstruction can not be 100% because for some events there are no jet assignments that satisfy all the criteria defined above. In this case we reject the event.

H_{T} and $p_{\mathrm{T}}(Z)$ cuts are reverted at the stage of $Z+\geq 4$ jets event selection to obtain a signal depleted control region. We carefully check the reconstruction performance in this region and then continue to apply tight H_{T} and $p_{\mathrm{T}}(Z)$ cuts to obtain a signal enriched sample.

Z mass window requirement is also removed at the stage of inclusive Z boson selection to study non Z+jets backgrounds at the side-bands.

2.6. Comparison of the Predicted Backgrounds and Data

2.6.1. Comparisons at the Inclusive Z Boson Selection Stage

In order to check the level of agreement between data and the simulation, we compare data and the simulated samples at each event selection stage of the analysis. We start with comparisons after satisfying Z mass window cut yet without any requirement on the number of jets. These checks are crucial especially for determining the normalization of the overwhelming Z+jets background and the distributions of important variables such as $p_{\mathrm{T}}(Z)$ and H_{T} at an early stage. In the plots shown in the rest of this section, comparisons are shown separately for $e^{+}e^{-}$ and $\mu^{+}\mu^{-}$ channels where the bottom panels indicate the ratio between the real data and the expected backgrounds from simulations. The shaded area corresponds to the total systematic variation on the backgrounds.

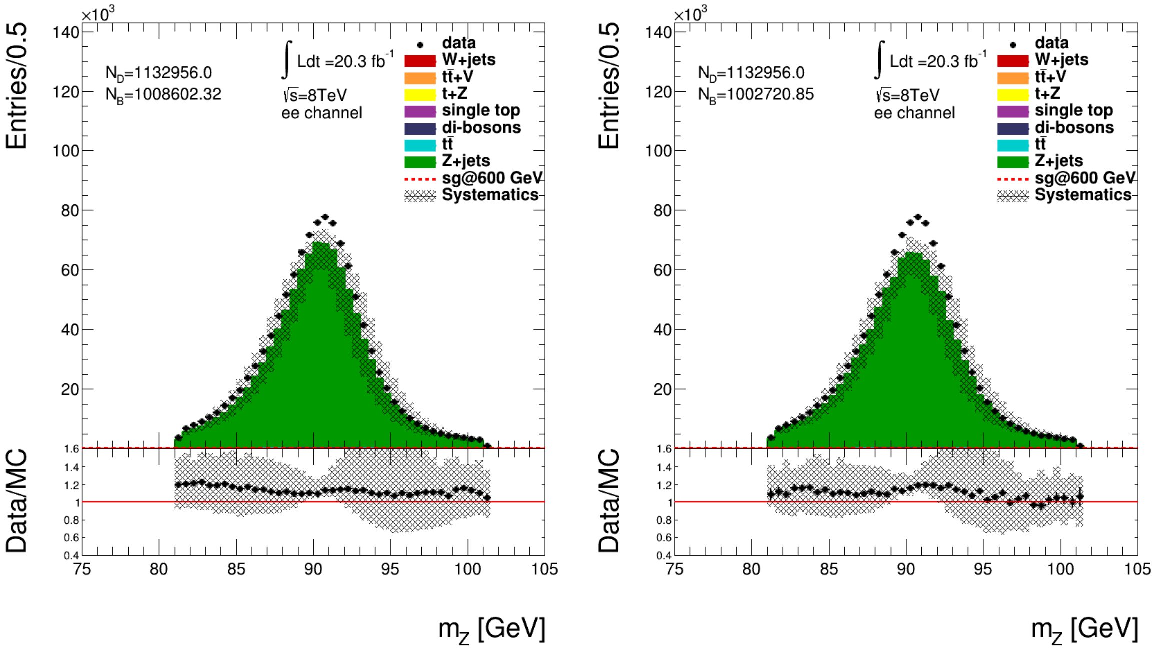

Figure 2.13. Comparison of the data and the simulated backgrounds in the M_Z distribution using ALPGEN(left) and SHERPA(right) Z+jets samples in the e^+e^- channel at the inclusive Z boson selection stage.

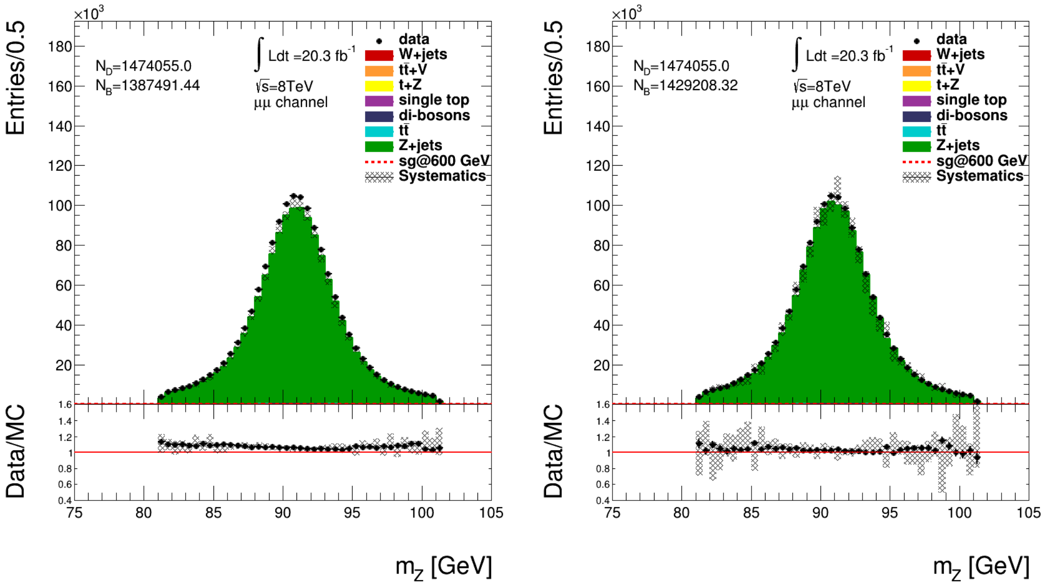

Figure 2.14. Comparison of the data and the simulated backgrounds in the M_Z distribution using ALPGEN(left) and SHERPA(right) Z+jets samples in the $\mu^+\mu^-$ channel at the inclusive Z boson selection stage.

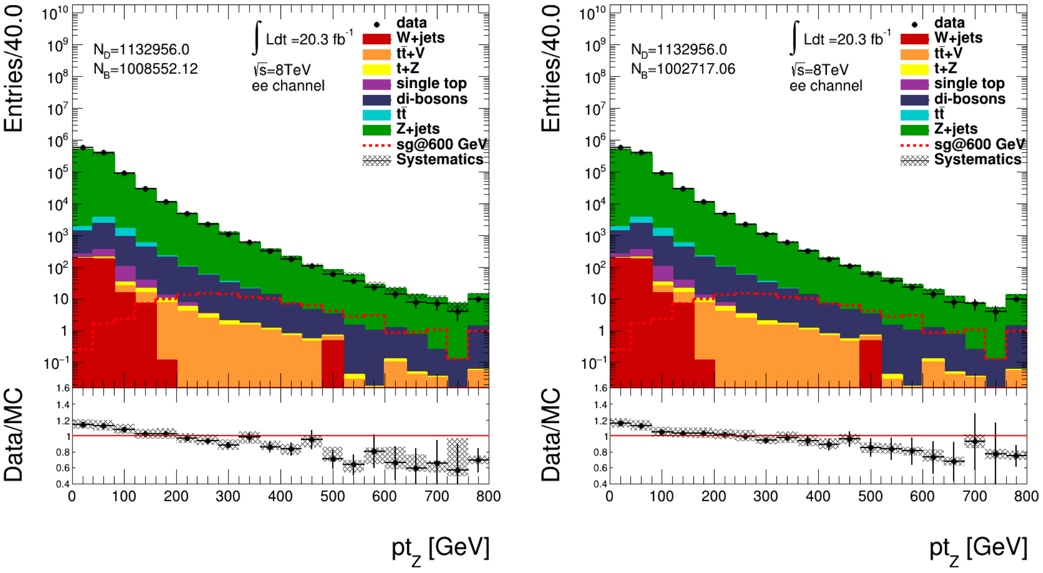

Figure 2.15. Comparison of the data and the simulated backgrounds in the $p_{\mathrm{T}}(Z)$ distribution using ALPGEN(left) and SHERPA(right) Z+jets samples in the e^+e^- channel.

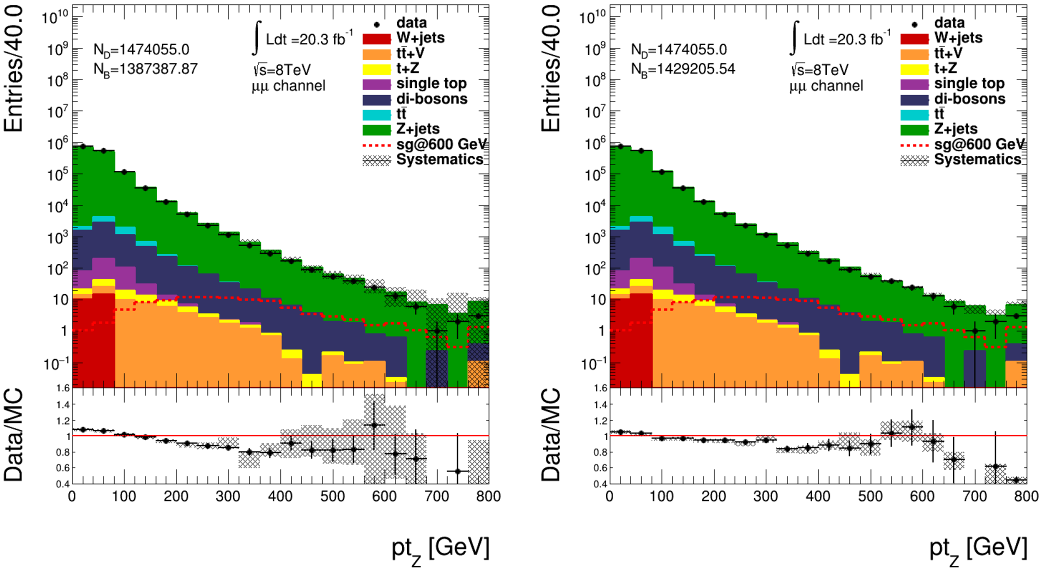

Figure 2.16. Comparison of the data and the simulated backgrounds in the $p_{\mathrm{T}}(Z)$ distribution using ALPGEN(left) and SHERPA(right) Z+jets samples in the $\mu^+\mu^-$ channel.

From the distributions shown in Figures 2.15 - 2.16 it is observed that the variable $p_{\mathrm{T}}(Z)$ is slightly mismodelled by the simulations. The small excess of events at low $p_{\mathrm{T}}(Z)$ in the e^+e^- channel are mostly from the fake lepton events passing through our electron selection criteria as electrons have higher fake rates when compared to the muons. More seriously, a downward slope at high $p_{\mathrm{T}}(Z)$ is observed in both e^+e^- and $\mu^+\mu^-$ channels. As we are applying cuts on these variables towards the final stage of the event selection, these mismodellings would result in over-predicted number of background events if uncorrected. We will mention about all such correction procedures in the upcoming sections.

The NLO k-factors used in ALPGEN and SHERPA are just corrections to their cross sections while both event generators still have only LO accuracy at the matrix level. Another SHERPA Z+jets sample prepared with the MENLOPS prescription with a NLO accuracy at the matrix level has also been used which indicates a better data/simulation agreement related to the Z boson kinematics. The corresponding distributions obtained from the MENLOPS samples are shown below.

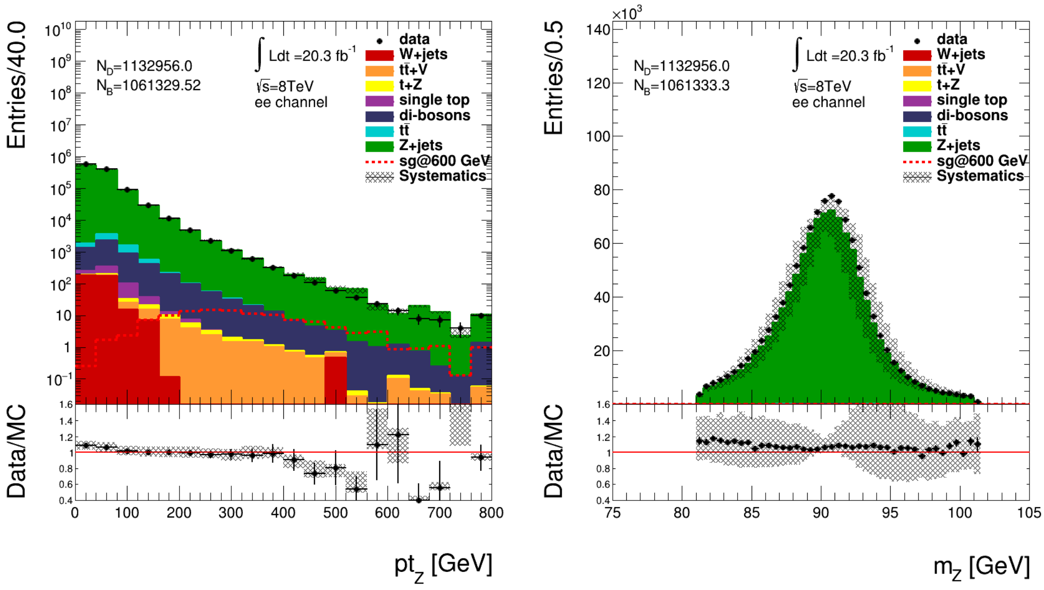

Figure 2.17. $p_{\mathrm{T}}(Z)$ and M_Z distributions at the inclusive Z boson selection stage for the e^+e^- channel. Z+jets backgrounds have been modelled by MENLOPS.

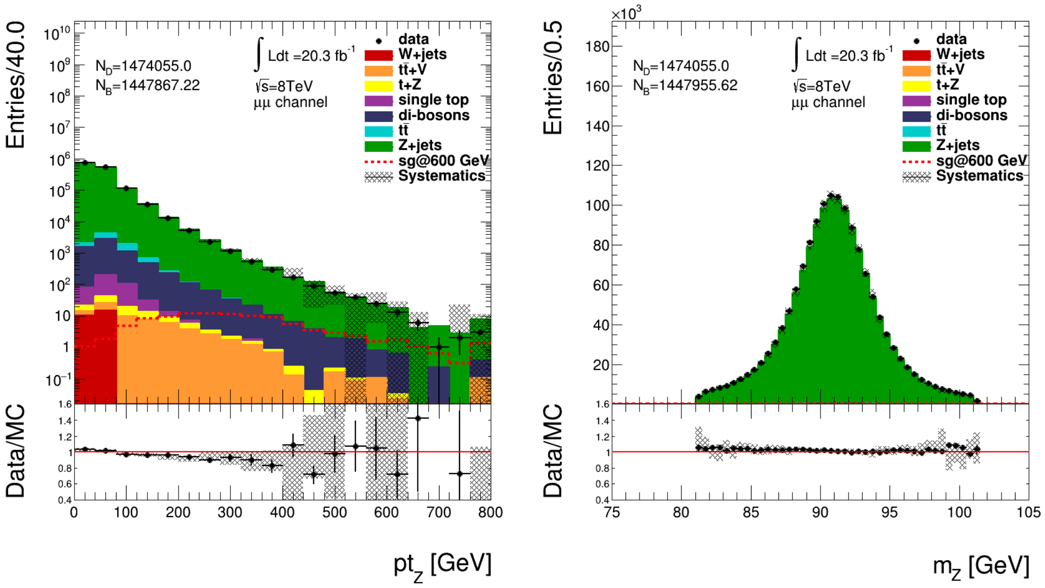

Figure 2.18. Comparisons of $p_{\mathrm{T}}(Z)$ and M_Z distributions at the inclusive Z boson selection stage for the $\mu^+\mu^-$ channel. Z+jets backgrounds have been modelled by MENLOPS.

From Figures 2.17 and 2.18 we can conclude that the NLO calculations at the matrix level provides a more realistic description $p_{\mathrm{T}}(Z)$ variable while yielding a better cross section on the Z+jets events. Thus we apply corrections to ALPGEN and SHERPA by matching their $p_{\mathrm{T}}(Z)$ to that of MENLOPS.

However as the MENLOPS samples lack of enough statistics at high $p_{\mathrm{T}}(Z)$, the correction is chosen to be applied where $p_{\mathrm{T}}(Z) \leq 500$ GeV in order not to introduce any statistical errors at the very beginning of the event selection. Furthermore, bottom and charm quarks are taken to be massless in the MENLOPS so the results from this generator cannot be trusted once we require b-tagging information. For these reasons we do not use the MENLOPS sample throughout the analysis except for deriving a $p_{\mathrm{T}}(Z)$ correction in the inclusive Z boson sample.

Figures 2.19 and 2.22 indicate Z boson mass and p_{T} after the MENLOPS corrections have been applied to both ALPGEN and SHERPA samples. The correction mostly effects the ALPGEN sample with an incrase of 3% in the cross section, p_{T} agreement is also slightly improved.

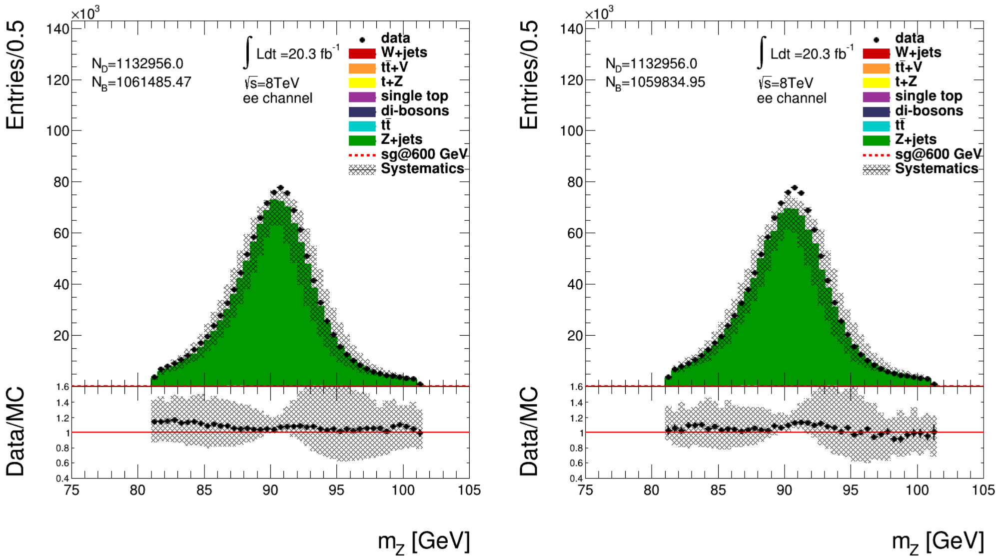

Figure 2.19. Comparisons of M_Z distributions at the inclusive Z boson selection stage for the e^+e^- channel after MENLOPS $p_{\mathrm{T}}(Z)$ correction is applied. Z+jets events are modelled by ALPGEN(left) and SHERPA(right).

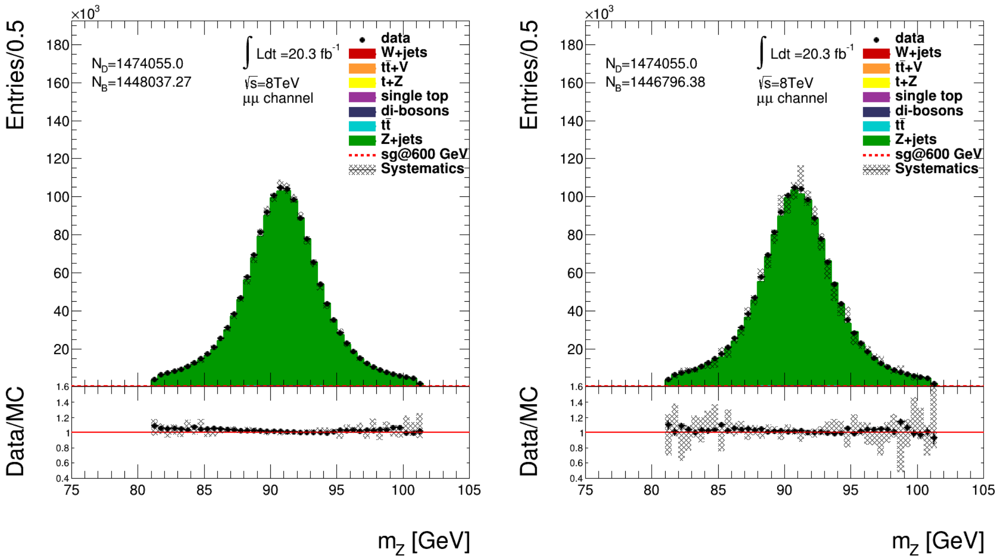

Figure 2.20. Comparisons of M_Z distributions at the inclusive Z boson selection stage for the $\mu^+\mu^-$ channel after MENLOPS $p_{\mathrm{T}}(Z)$ correction is applied. Z+jets events are modelled by ALPGEN(left) and SHERPA(right).

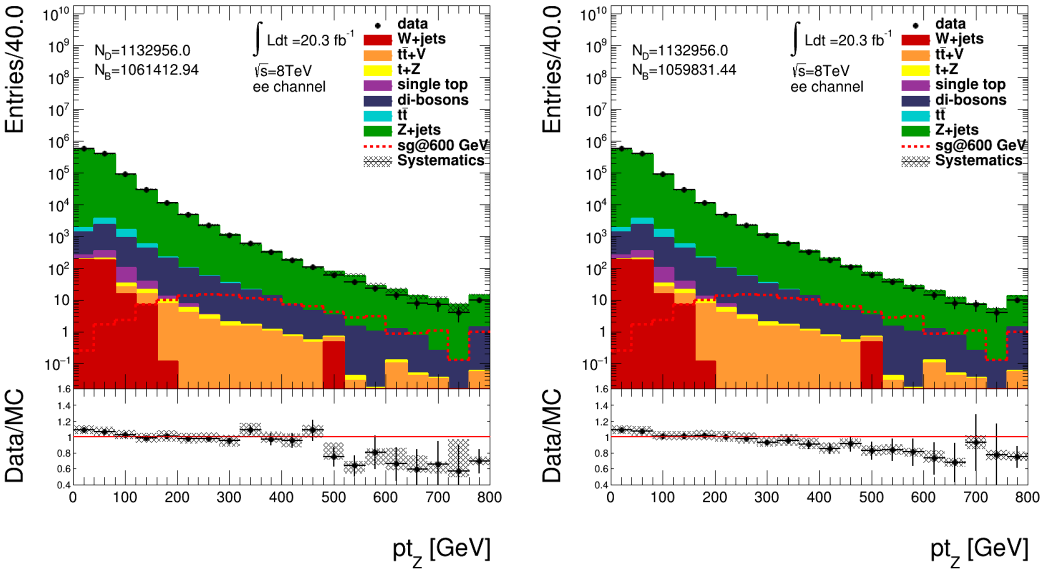

Figure 2.21. Comparisons of $p_{\mathrm{T}}(Z)$ distributions at the inclusive Z boson selection stage for the e^+e^- channel after MENLOPS $p_{\mathrm{T}}(Z)$ correction is applied. Z+jets events are modelled by ALPGEN(left) and SHERPA(right).

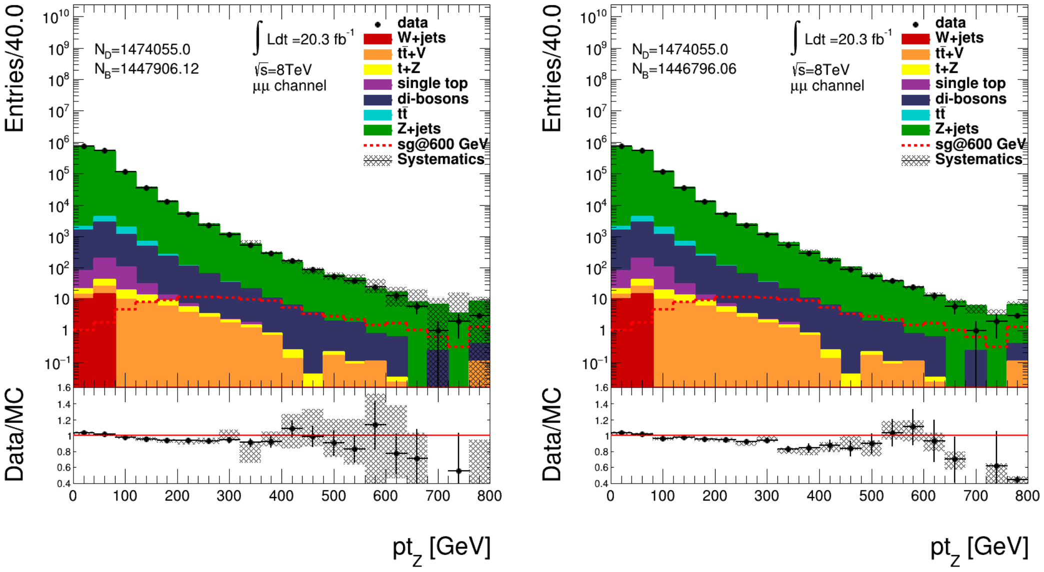

Figure 2.22. Comparisons of $p_{\mathrm{T}}(Z)$ distributions at the inclusive Z boson selection stage for the $\mu^+\mu^-$ channel after MENLOPS $p_{\mathrm{T}}(Z)$ correction is applied. Z+jets events are modelled by ALPGEN(left) and SHERPA(right).

After applying Monte-Carlo driven $p_{\mathrm{T}}(Z)$ correction, the next variables of interest are the jet and b-jet multiplicities. As we go further with the event selection by requiring at least 4 jets and b-jet veto, the jet multiplicities will play a prosecutory role in the final distributions that we will obtain in the coming chapters. Any disagreement on jet/b-jet multiplicities will automatically cause excess or deficit on the number of expected events in the final event selection which will significantly bias our final result. Depending on how badly the simulation models the reality, this issue may cause a fake discovery depending on the number of events in the final distributions or may reduce our search sensitivity.

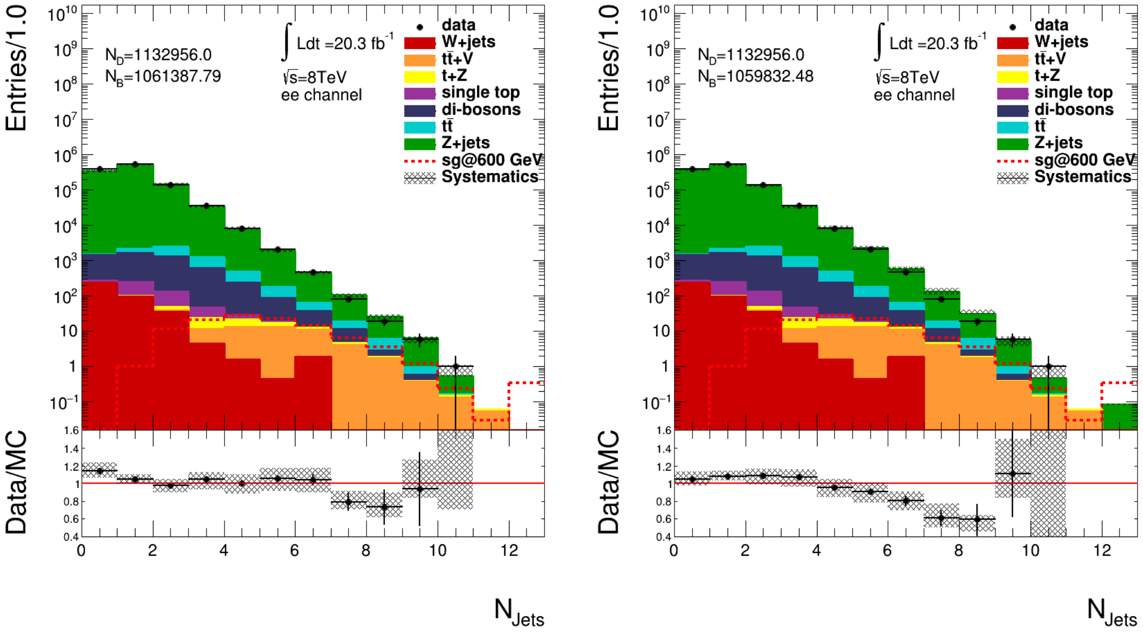

Figure 2.23. Comparisons of the jet multiplicites at the inclusive Z boson selection stage for the e^+e^- channel. Z+jets events are modelled by ALPGEN(left) and SHERPA(right).

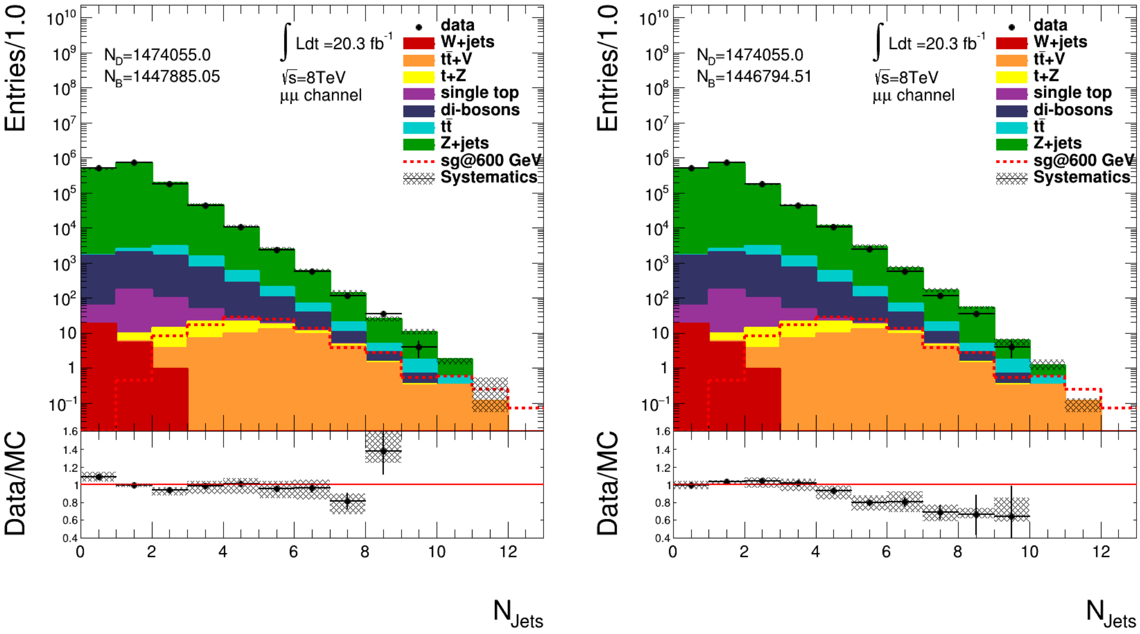

Figure 2.24. Comparisons of the jet multiplicites at the inclusive Z boson selection stage for the $\mu^+\mu^-$ channel. Z+jets are modelled by ALPGEN(left) and SHERPA(right).

From distributions 2.23 and 2.24, it is appearent that SHERPA Z+jets prediction will be a slight underestimate once we further require at least 4 jets. The impact will be an overall normalization factor on all the distributions.

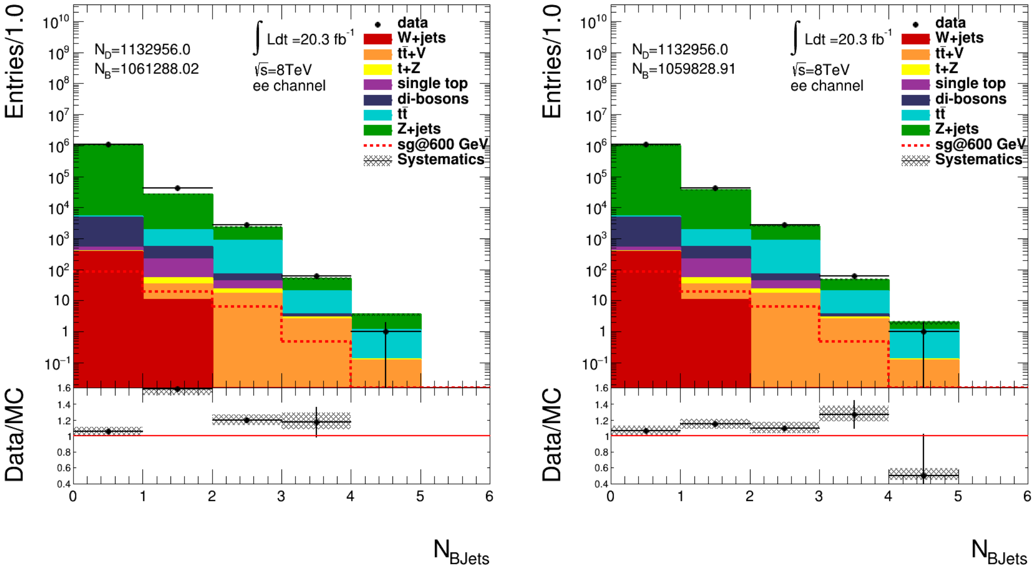

Figure 2.25. Comparisons of the b-jet multiplicites at the inclusive Z boson selection stage for the e^+e^- channel. Z+jets events are modelled by ALPGEN(left) and SHERPA(right).

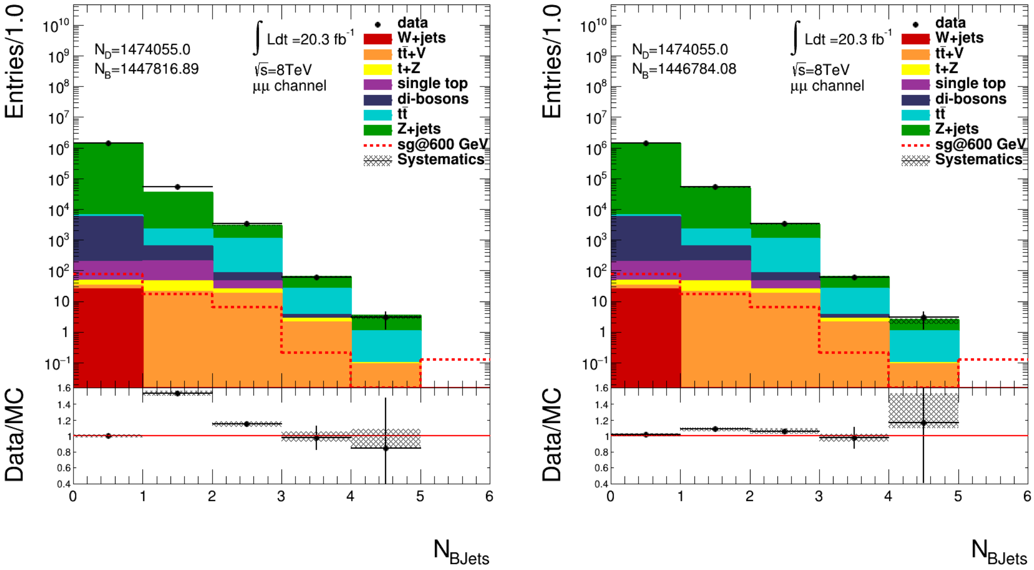

Figure 2.26. Comparisons of the b-jet multiplicites at the inclusive Z boson selection stage for the $\mu^+\mu^-$ channel. Z+jets events are modelled by ALPGEN(left) and SHERPA(right).

It also turns out that SHERPA samples provide a better heavy flavor composition in both channels when compared to the ALPGEN as can be seen in Figures 2.25-2.26. Considering the fact that all other backgrounds are small when compared to Z+jets in those figures, we assume that the only significantly mismodelled background is Z+jets. To justify this assumption we compare M_Z with the side bands classified in various b-tag bins.

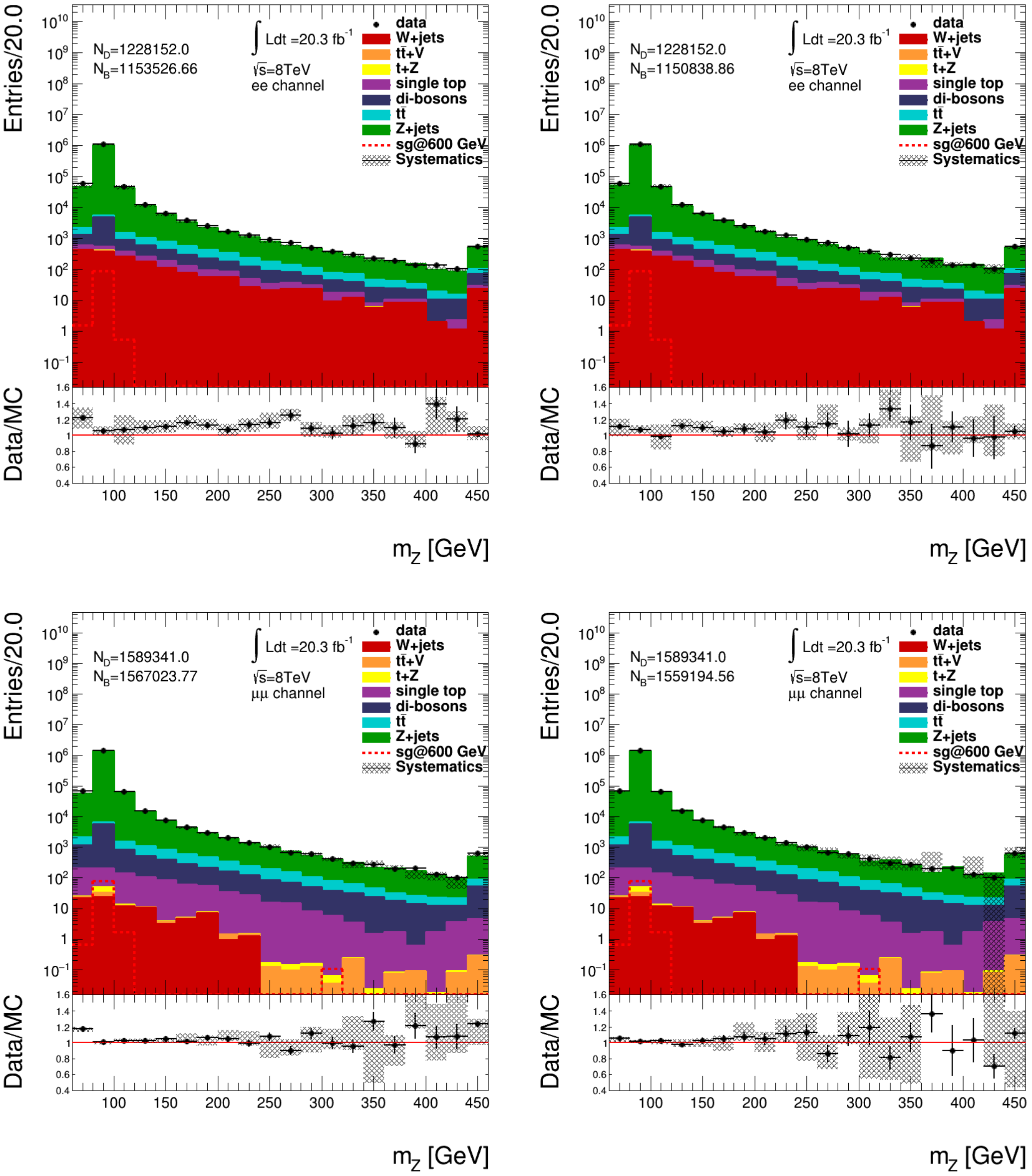

Figure 2.27. Comparisons of M_Z with the side-bands outside the Z mass window in the 0 b-tag exclusive bin. Left(Right) column consists of ALPGEN(SHERPA) Z+jets sample.

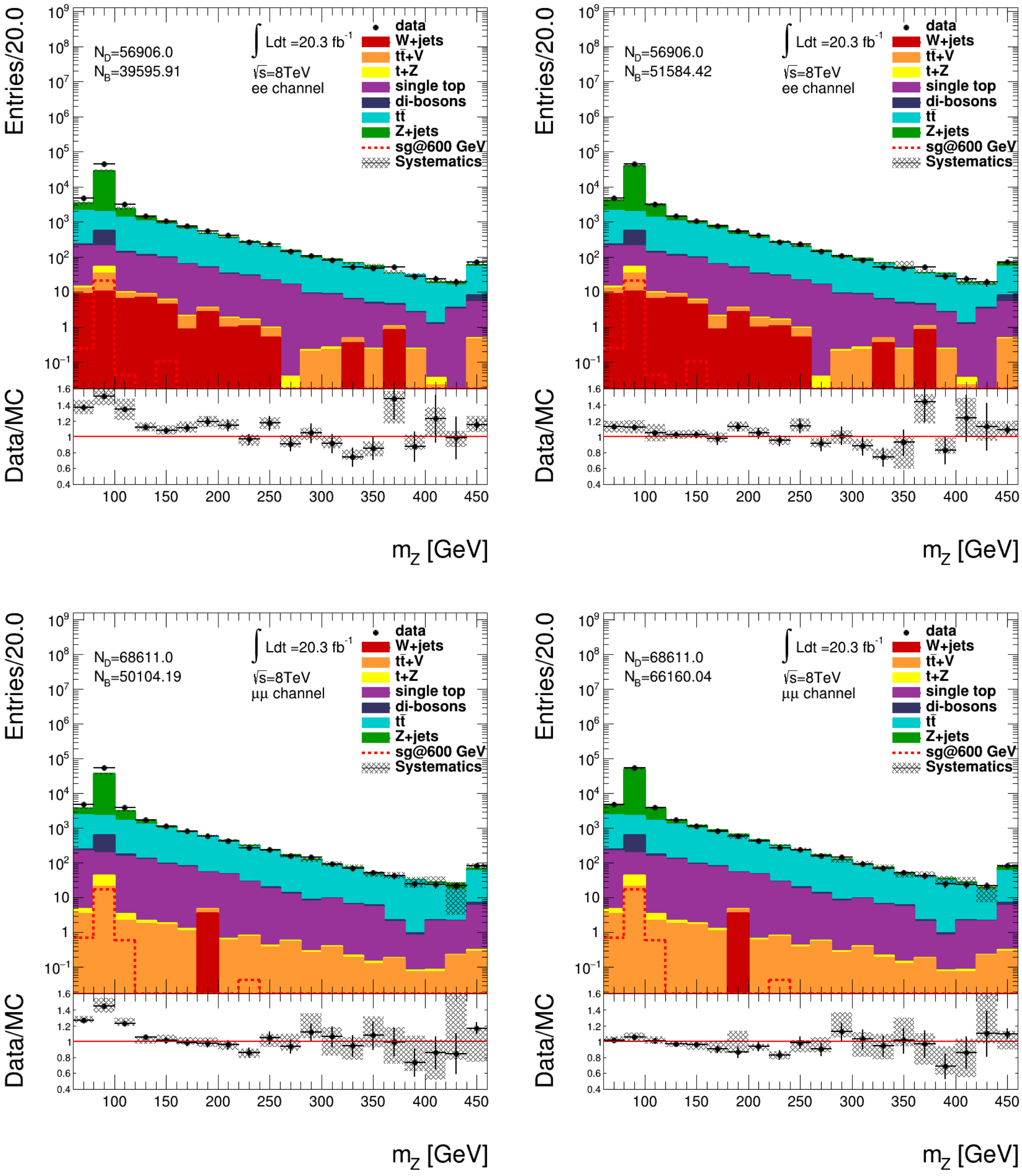

Figure 2.28. Comparisons of M_Z with the side-bands outside the Z mass window in the 1 b-tag exclusive bin. Left(Right) column consists of ALPGEN(SHERPA) Z+jets sample.

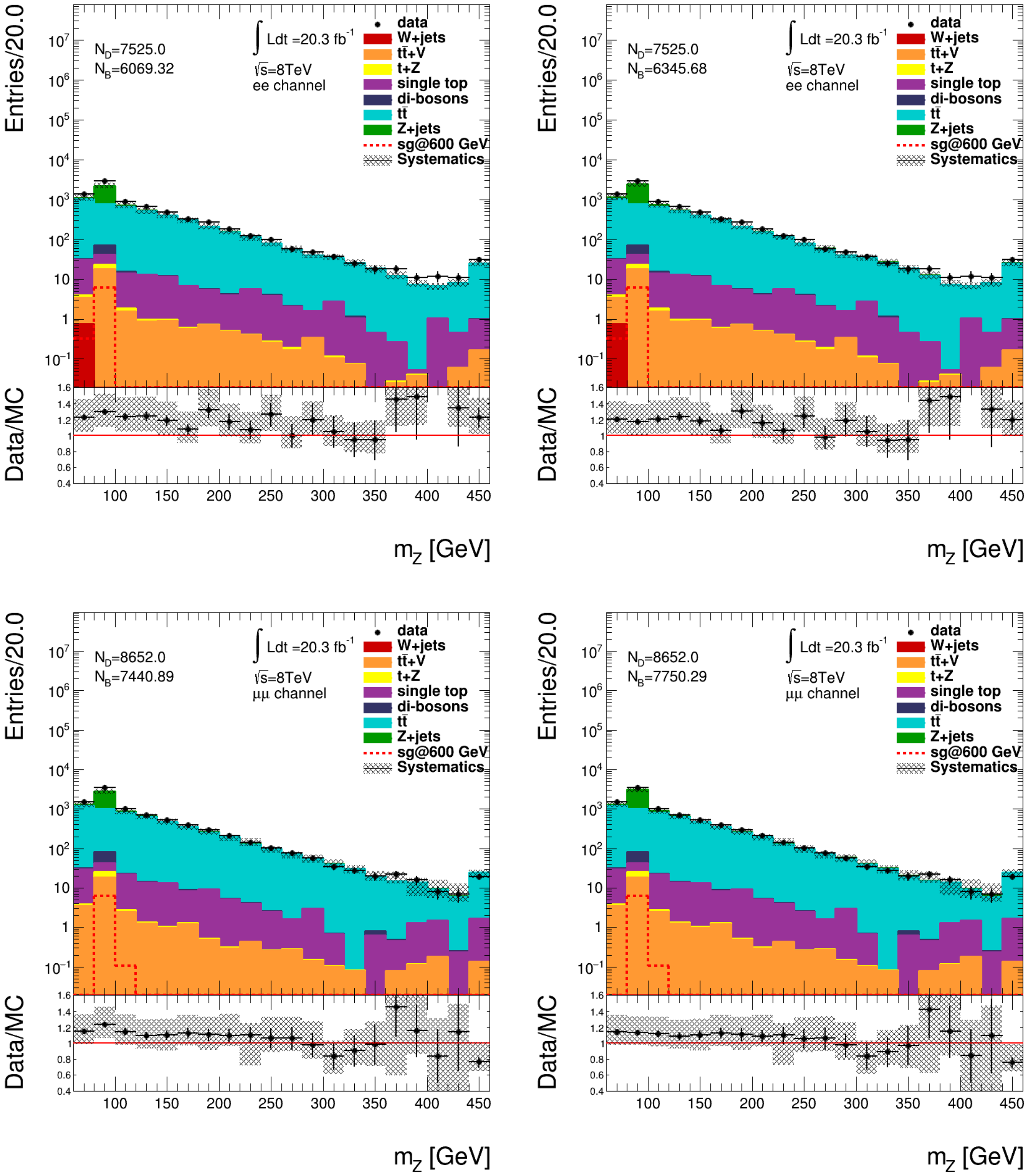

Figure 2.29. Comparisons of M_Z with the side-bands outside the Z mass window in the 2 b-tag inclusive bin. Left(Right) column consists of ALPGEN(SHERPA) Z+jets sample.

The decent data/simulation agreement outside the Z mass window in distributions 2.28 - 2.29, and large disagreements around the Z peak clearly supports our assumption that the only insufficiently modelled background is Z+jets.

2.6.2. Comparisons at the $Z+\geq$ 4jets stage

To see the impact of jet multiplicities as shown in Figures 2.23 - 2.24 we start with comparing distributions after requiring at least 4 jets. As our final event selection also requires a b-jet veto, we first study the b-jet composition of the events with this selection. Figures 2.30 and 2.31 indicate some disagreements on the number of b-jets in the simulated events. Those heavy flavor composition issues in the both event generators are already known and addressed in a previous heavy quark search [41] yet with the heavy quarks coupling to heavy flavor jets only. To compensate for these disagreements, data driven scale factors to b-jet multiplicities are derived in a control region where $p_{\mathrm{T}}(Z) \leq 100$ GeV then extrapolated to the whole $p_{\mathrm{T}}(Z)$ region. Systematics assessment related to this correction is carried out by deriving the same scale factors in another control region where 50 GeV $\leq p_{\mathrm{T}}(Z) \leq 150$ GeV. The difference between the two is taken as a systematic error.

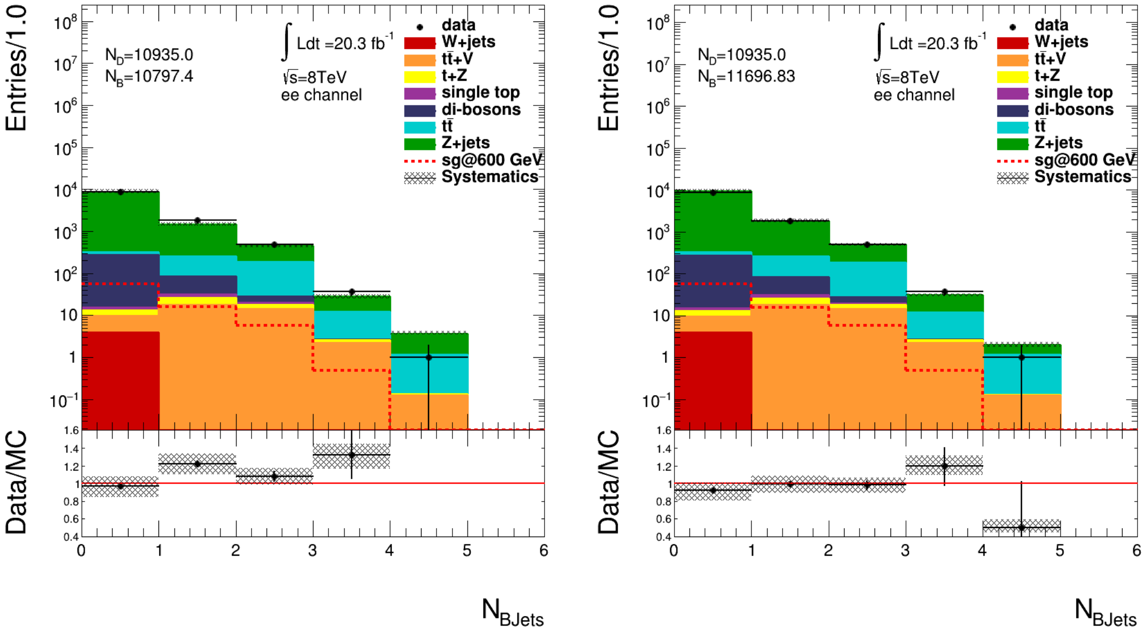

Figure 2.30. b-jet multiplicities after requiring at least 4 jets obtained by ALPGEN(left) and SHERPA(right) in the e^+e^- channel.

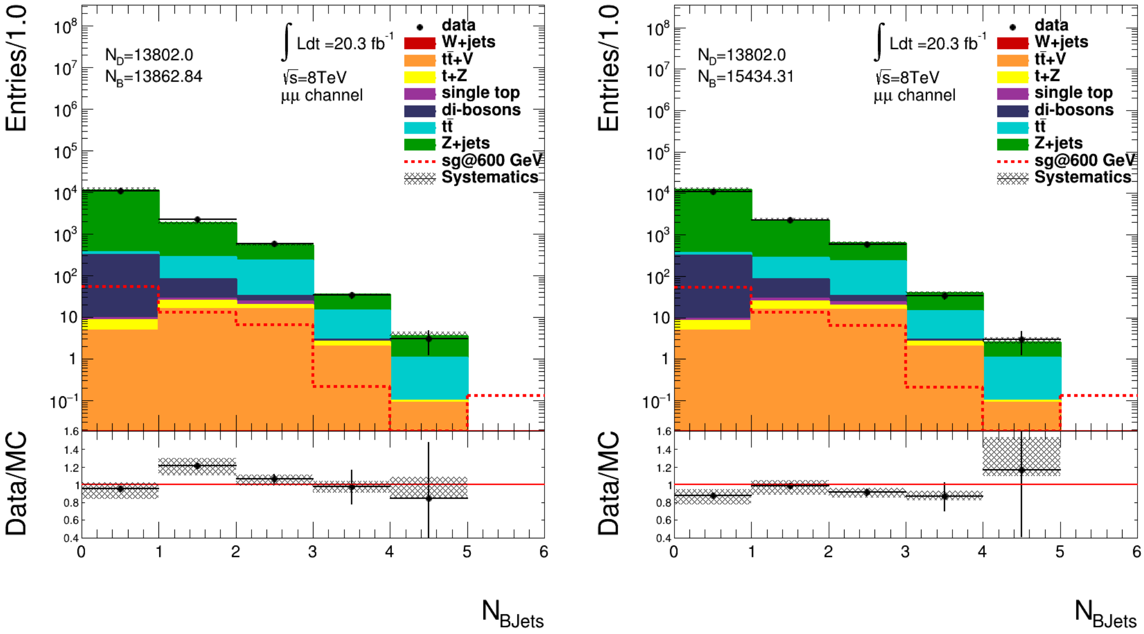

Figure 2.31. b-jet multiplicities after requiring at least 4 jets obtained by ALPGEN(left) and SHERPA(right) in the $\mu^+\mu^-$ channel.

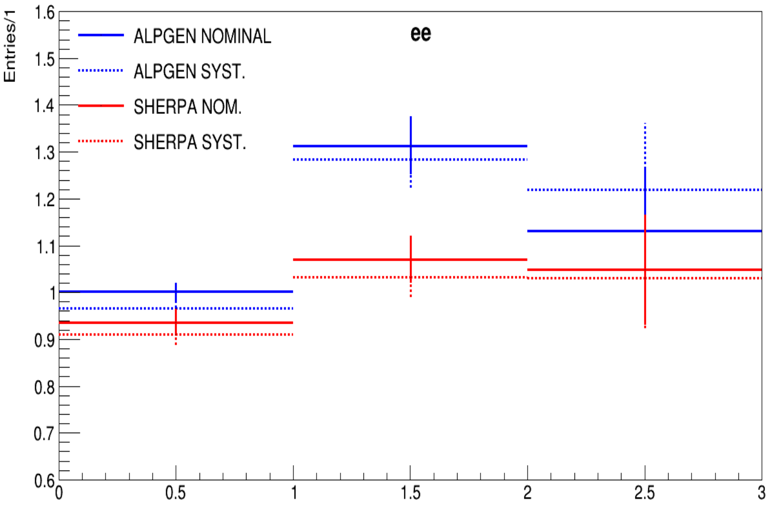

Figure 2.32. b-jet multiplicity corrections derived in the nominal and systematic regions in the $Z+\geq 4$ jets sample in the e^+e^- channel.

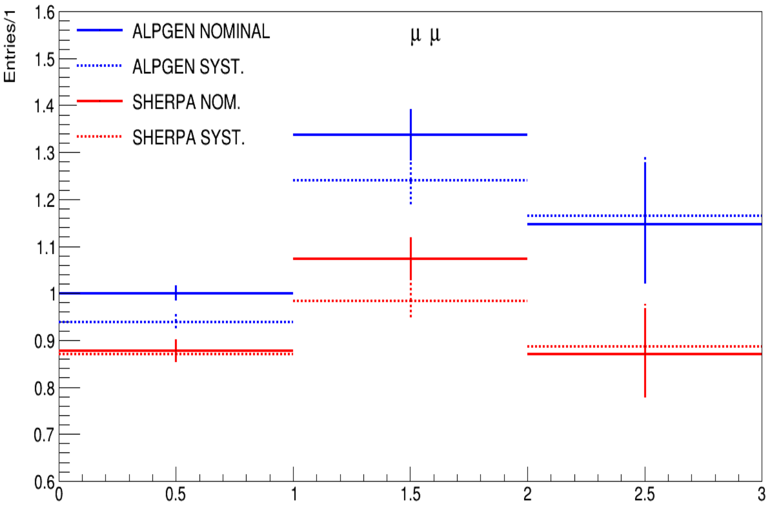

Figure 2.33. b-jet multiplicity corrections derived in the nominal and systematic regions in the $Z+\geq4$ jets sample in the $\mu^+\mu^-$ channel.

The correction factors in Figures 2.32-2.33 are derived by bin-wise subtraction all the backgrounds, except Z+jets, from the data. Then this difference is divided by the Z+jets expectation in the corresponding bin to obtain the scale factor. Mathematically speaking, each bin (i) is scaled to the data expectation by a scale factor ϵ_i:

$$\epsilon_i = \frac{N_{data}^{(i)} - N_{other}^{(i)}}{N_{Z+jets}^{(i)}} \tag{2.3}$$

Hence, instead of normalizing the Z+jets background using their theoretical cross section, we are normalizing it via a data driven method by using the scale factors in Figures 2.32-2.33. We deduce that ALPGEN sample has a slightly larger systematic error of 6% when compared to SHERPA with an error of 4% as derived in the 0 b-tag bin. Additional 2% of statistical errors are to be added in quadrature as indicated by the vertical error bars in those figures. As a conservative approach, the largest of the errors are taken into account and applied to both of them. After all, this is going to correspond to ±6.5% uncertainty in the cross section for both samples in the final event selection.

After applying b-jet multiplicity correction, the disagreements as seen in Figures 2.30 and 2.31 have been reduced significantly while keeping the shape of the distributions unchanged. Figure 2.34 shows the b-jet multiplicities after the scaling correction has been applied.

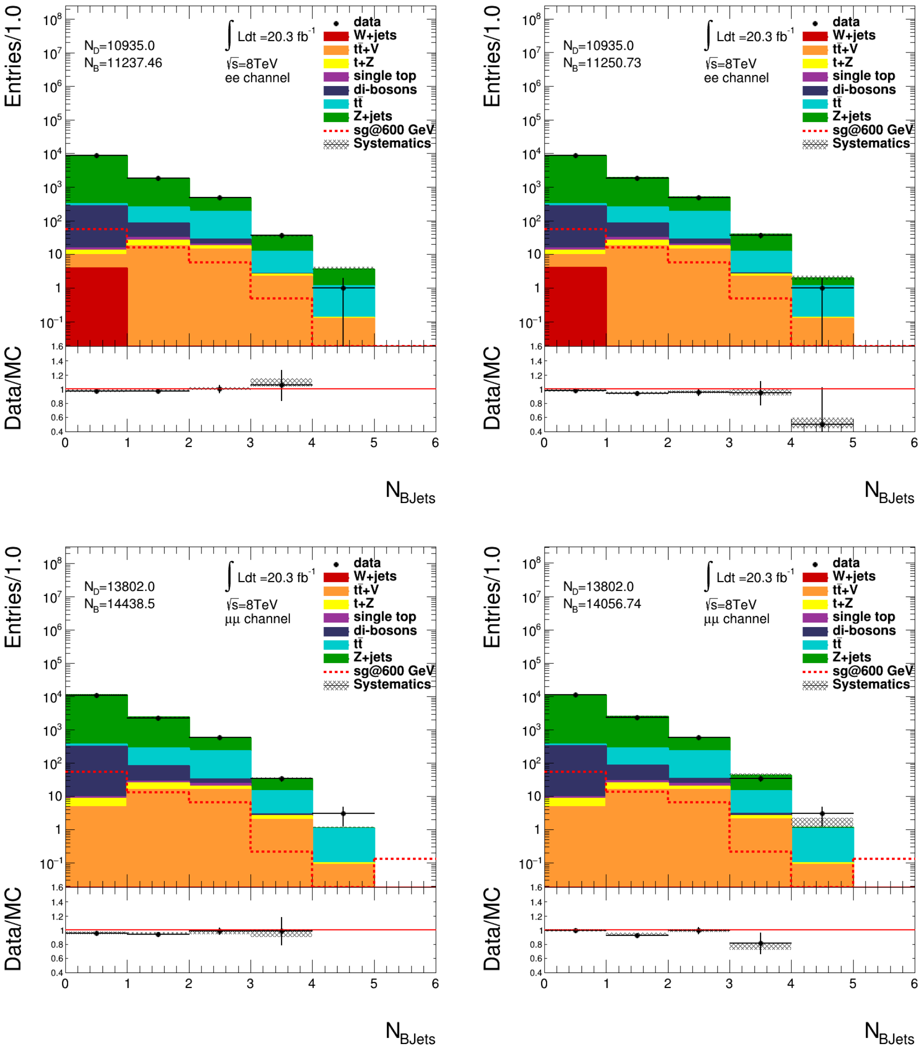

Figure 2.34. b-jet multiplicities after requiring at least 4 jets obtained by ALPGEN(left) and SHERPA(right) in the $\mu^+\mu^-$ channel when the b-jet scaling correction is applied.

The next stage of event selection will involve the requirement of very large $p_{\mathrm{T}}(Z)$ and H_{T}. Similar downward slopes in DATA/MC ratios as encountered in Figures 2.15 - 2.16 are also apparent in the Z+$\geq$4 jets sample as can be seen in Figure 2.36. To account for this disagreement we derive a data-driven correction by matching $p_{\mathrm{T}}(Z)$

of the Z+jets sample to that of the data in a region where $pT(j_3) \leq 100$ GeV. The correction is then applied to all events.

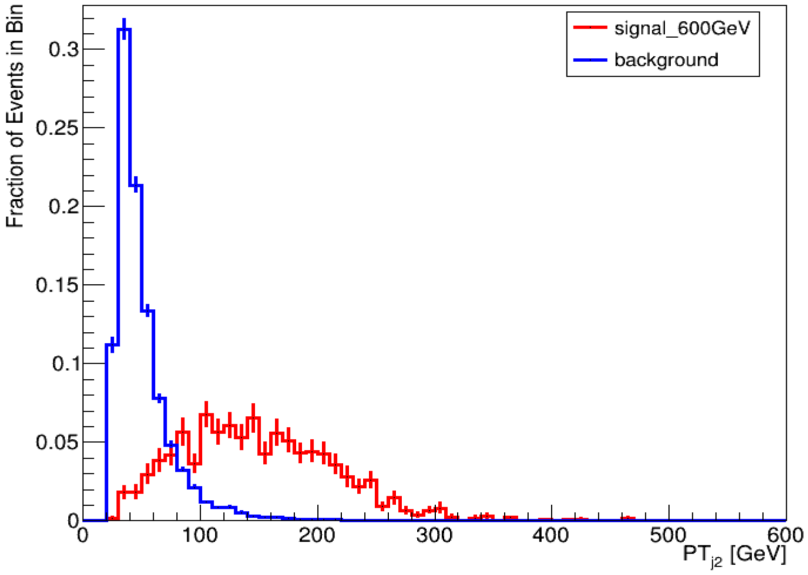

Figure 2.35. Third leading jet p_{T} shape for the simulated signal and total expected background after requiring at least 4 jets. The distributions are normalized to unity.

Even though we are not sensitive to the expected signal at this stage, the control region is carefully chosen to minimize the contamination from possible signal events. The related systematic error on this correction is estimated by deriving the same correction in a region where 50 GeV $\leq p_{\mathrm{T}}(j_3) \leq$ 150 GeV. The difference between corrections derived in these two regions is considered as a systematic error in the statistical analysis.

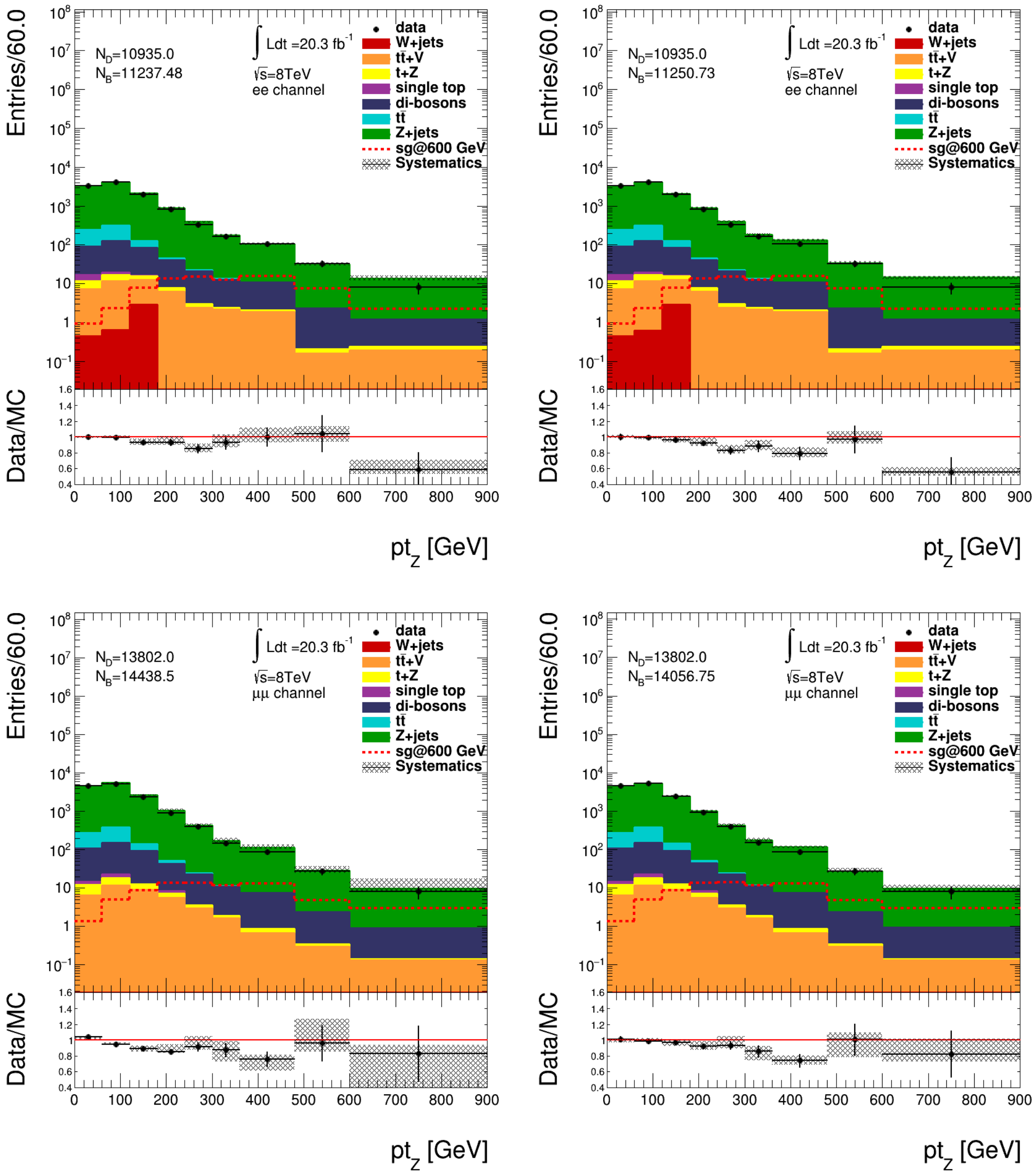

Figure 2.36. $p_{\mathrm{T}}(Z)$ distribution at $Z+\geq4$ jets stage after b-jet multiplicity scaling and before data-driven $p_{\mathrm{T}}(Z)$ correction is applied. Left(Right) column consists of ALPGEN(SHERPA) Z+jets sample.

If we leave $p_{\mathrm{T}}(Z)$ distribution uncorrected, it is apparent from figure 2.36 that we will over estimate Z+jets background approximately by 10% once we apply the cut $p_{\mathrm{T}}(Z)$ $\geq$150 GeV at the next stage of event selection. The uncorrected $p_{\mathrm{T}}(Z)$ will impact negatively on the reconstructed variables such as heavy quark and hadronic boson mass. After applying this correction data/simulation agreement has been improved significantly as can be seen from Figure 2.37.

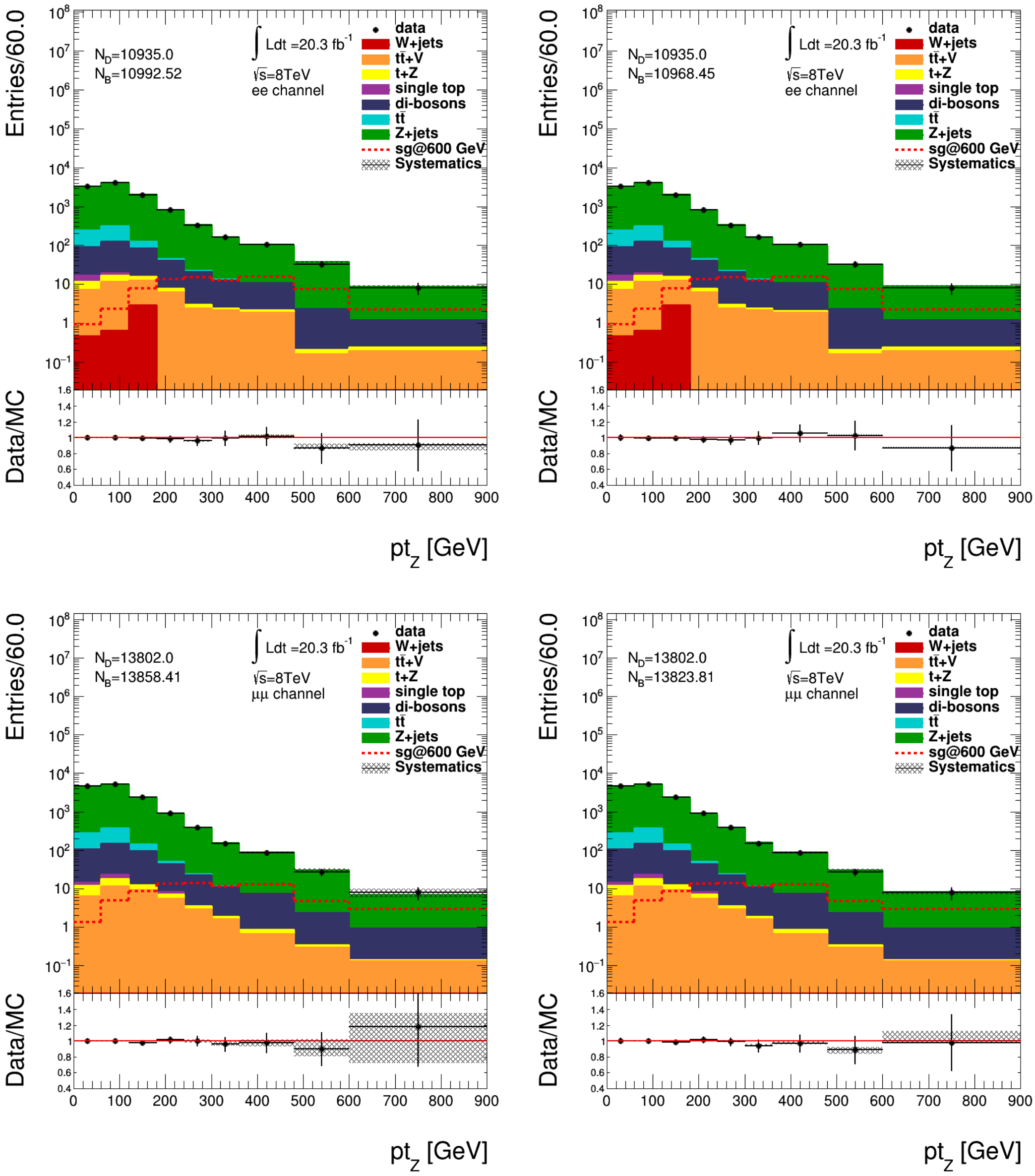

Figure 2.37. $p_{\mathrm{T}}(Z)$ distribution at $Z+\geq 4$ jets stage after data driven $p_{\mathrm{T}}(Z)$ correction is applied. Left(Right) column consists of ALPGEN(SHERPA) Z+jets sample.

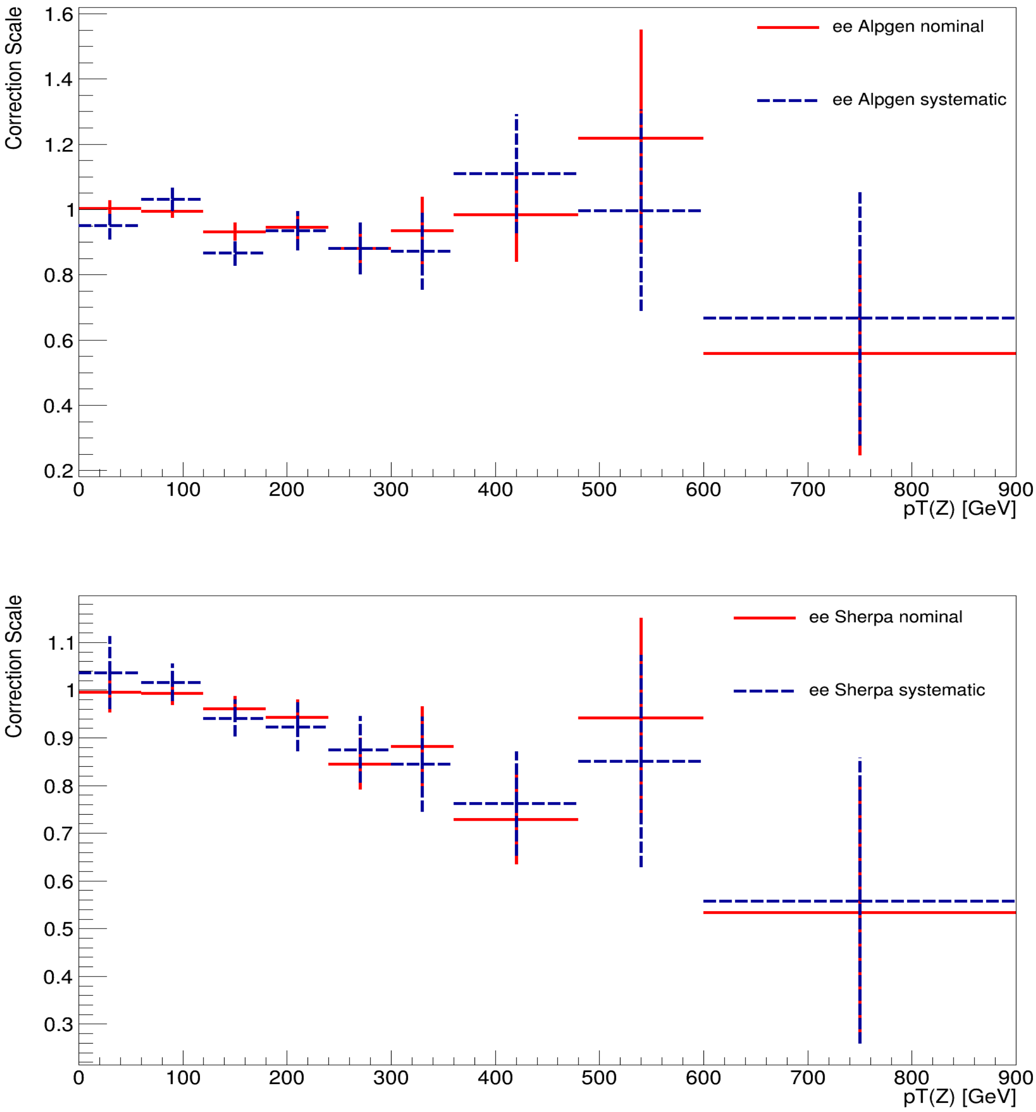

Figure 2.38. Data-driven $p_{\mathrm{T}}(Z)$ corrections and their systematic variations for ALPGEN and SHERPA Z+jets samples in the ee channel.

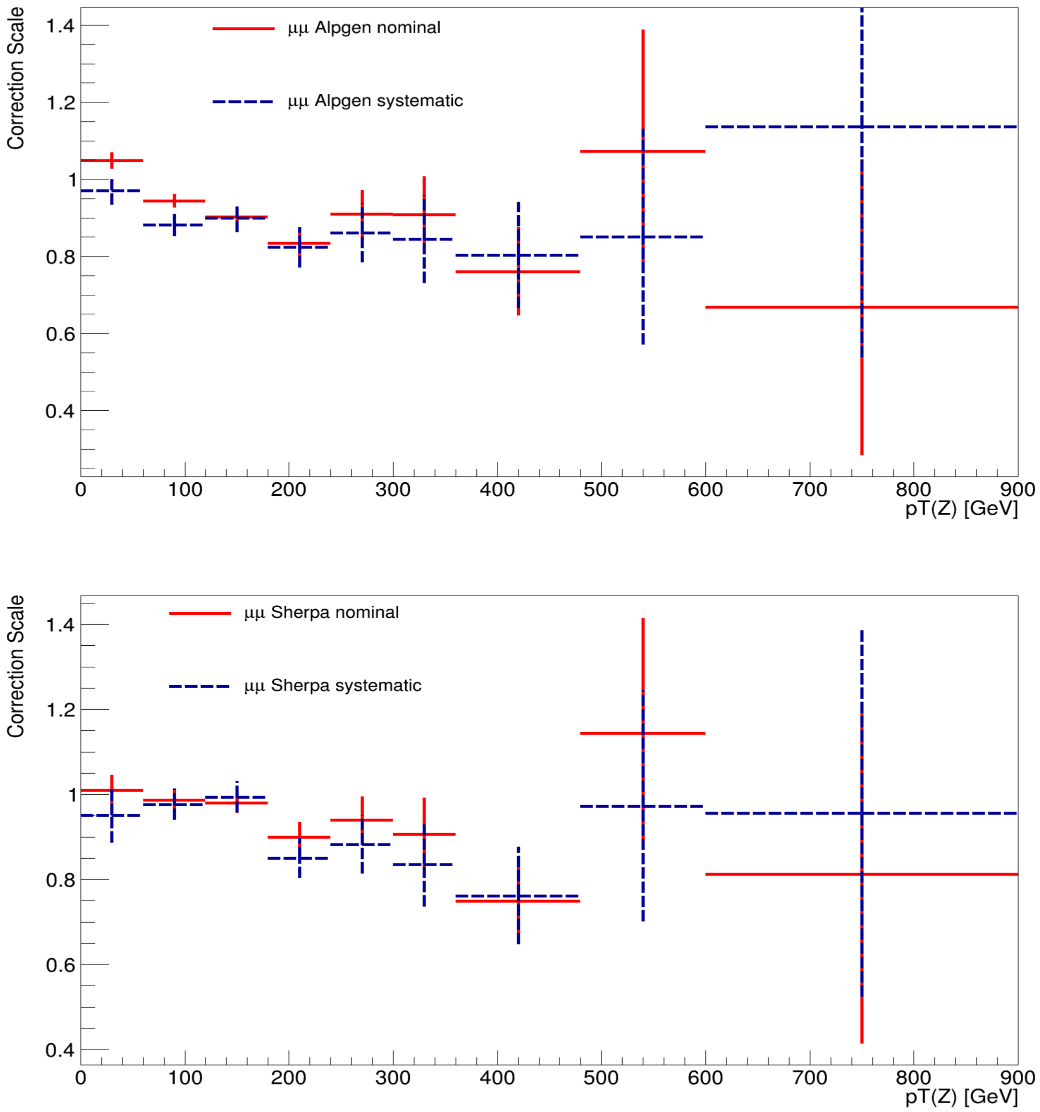

Figure 2.39. Data-driven $p_{\mathrm{T}}(Z)$ corrections and their systematic variations for ALPGEN and SHERPA Z+jets samples in the $\mu^+\mu^-$ channel.

The data driven $p_{\mathrm{T}}(Z)$ correction factors in the figures 2.38 and 2.39 are derived from the same method as in equation 2.3. The nominal corrections have been derived and applied explicitly for each systematic variation of the corresponding MC sample, such as the variations on jet energy scale, muon momentum resolution, electron trigger uncertainty etc..

Table 2.3. Number of expected and observed events in $Z+\geq 4$ jets sample

	e^+e^- **channel**	$\mu^+\mu^-$ **channel**
signal (600 GeV)	$77.99 \pm 3.25^{+12.65}_{-12.60}$	$74.26 \pm 3.23^{+55.16}_{-55.00}$
Z+jets(SHERPA no corr.)	$10915.36 \pm 144.97^{+1685.25}_{-1361.17}$	$14535.27 \pm 182.70^{+2152.61}_{-1573.29}$
Z+jets(SHERPA)	$10186.99 \pm 135.60^{+828.59}_{-830.18}$	$12924.76 \pm 162.36^{+1068.79}_{-1072.55}$
Z+jets(ALPGEN no corr.)	$10015.92 \pm 75.16^{+1697.34}_{-1382.45}$	$12963.78 \pm 87.31^{+2031.04}_{-1448.44}$
Z+jets(ALPGEN)	$10211.05 \pm 77.25^{+811.35}_{-812.88}$	$12959.35 \pm 88.48^{+1227.28}_{-1230.05}$
Other Bkg.	$781.47 \pm 13.45^{+320.08}_{-318.64}$	$899.06 \pm 14.93^{+363.83}_{-366.48}$
Total Bkg.(ALPGEN)	$10992.52 \pm 78.41^{+884.82}_{-885.50}$	$13858.41 \pm 89.73^{+1289.92}_{-1289.89}$
Total Bkg.(SHERPA)	$10968.46 \pm 136.27^{+900.38}_{-901.36}$	$13823.82 \pm 163.05^{+1139.99}_{-1141.25}$
Data	10935	13802

Since χ^2 values explained in equation 2.1 and 2.2 heavily depend on ΔR variable between the leptonic Z boson and the jet associated to it, we need to justify a decent DATA/MC agreements of these variables before going further and requiring large $p_{\mathrm{T}}(Z)$ and H_{T}. By obtaining ΔR distributions up to the 4th hardest jet we can conclude from the distributions 2.40 that ΔR agreements are in good shape for each p_{T} ordered jet.

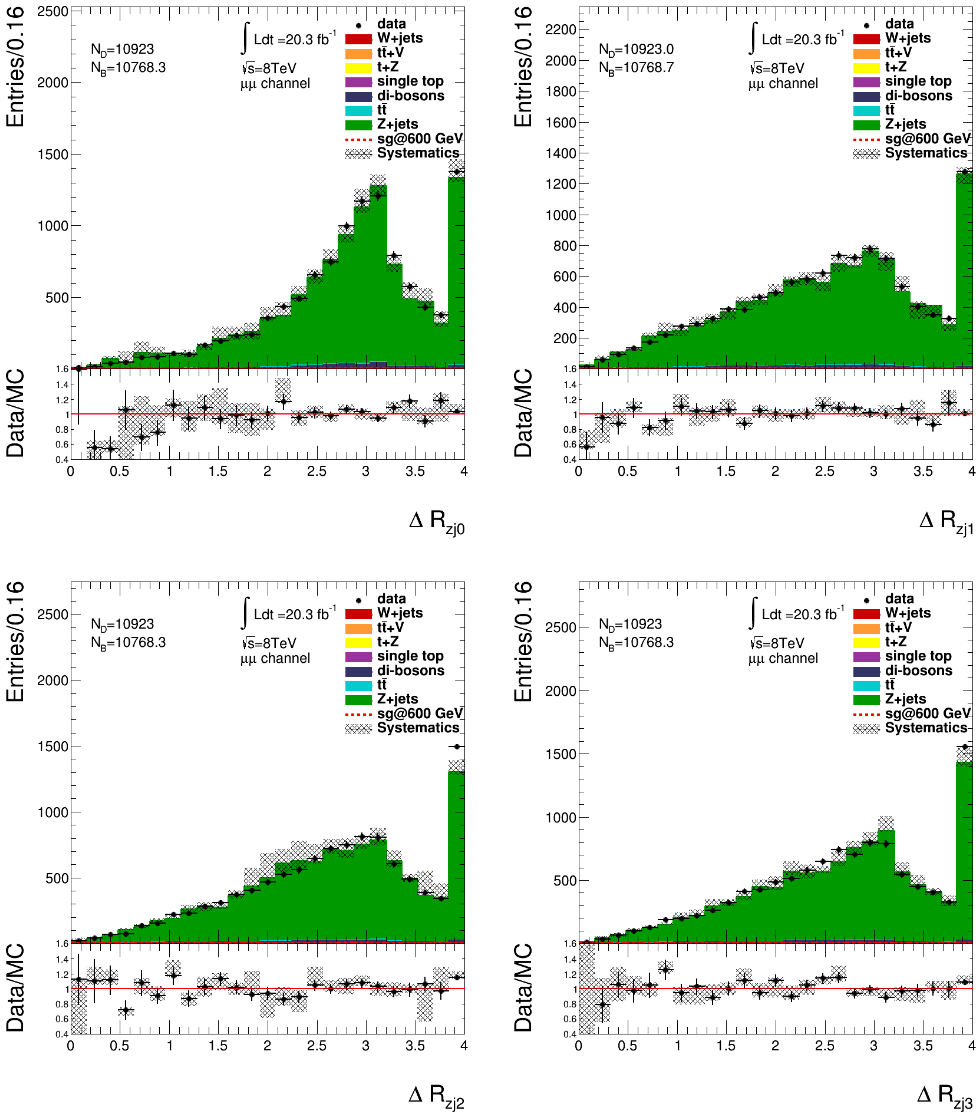

Figure 2.40. ΔR between Z boson and the first four hardest jets in the event at $Z + \geq 4$ jets sample after data-driven $p_{\mathrm{T}}(Z)$ correction and b-jet veto are applied. Distributions are obtained by SHERPA Z+jets sample.

The same kind of ΔR distributions are quite similar in the ee channel and for the ALPGEN samples. They can be seen in the appendix

2.6.3. Comparisons after $p_{\mathrm{T}}(Z)$ requirement

After applying b-jet veto , we select events with $p_{\mathrm{T}}(Z) \geq 150$ GeV and carefully observe the behavior of the other remaining critical variables such as H_{T} and M_Z.

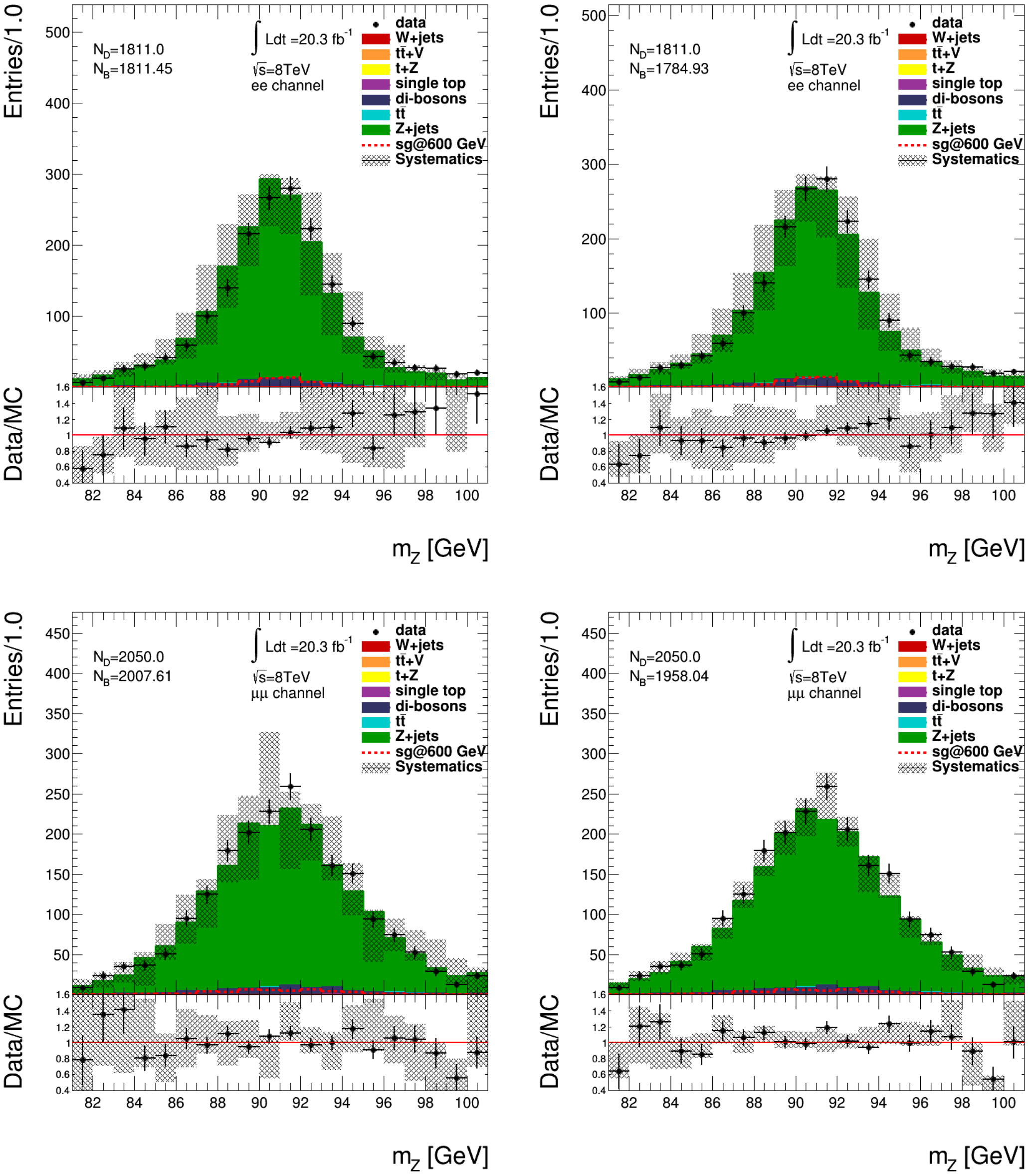

Figure 2.41. M_Z distributions in $Z+\geq 4$ jets sample after applying $p_{\mathrm{T}}(Z)$ cuts and b-jet veto. Left(right) column consists of ALPGEN (SHERPA) Z+jets sample.

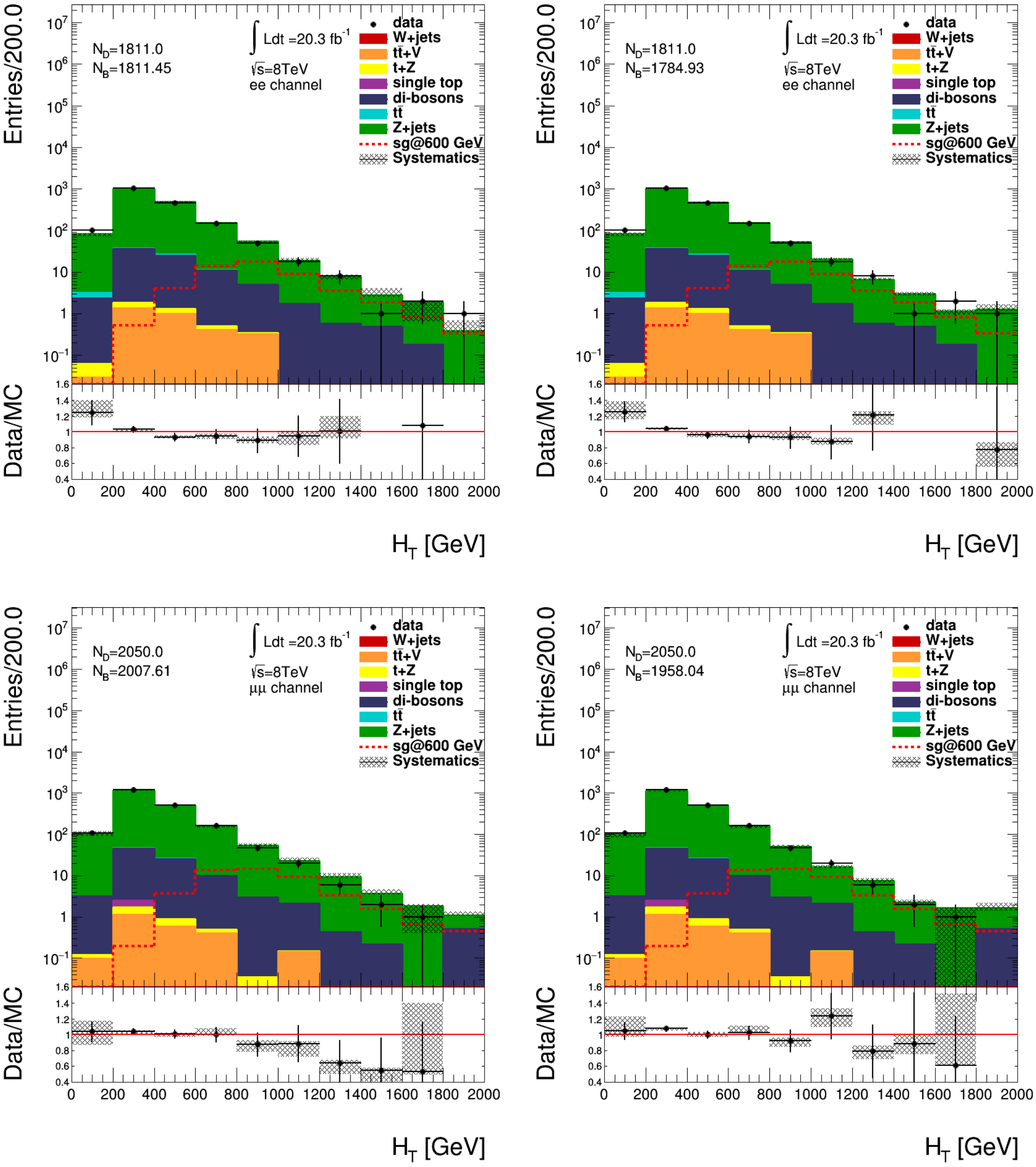

Figure 2.42. H_T distributions in Z+≥4 jets sample after applying $p_\mathrm{T}(Z)$ cut. Left(right) column consists of ALPGEN (SHERPA) Z+jets sample.

Table 2.4. Number of expected and observed events after $p_{\mathrm{T}}(Z) \geq 150$ GeV requirement.

	e^+e^- **channel**	$\mu^+\mu^-$ **channel**
signal (600 GeV)	$51.82 \pm 2.66^{+8.47}_{-8.42}$	$47.09 \pm 2.64^{+8.24}_{-7.34}$
Z+jets(SHERPA no corr.)	$1981.06 \pm 14.47^{+245.06}_{-228.16}$	$2282.38 \pm 15.96^{+248.01}_{-203.44}$
Z+jets(SHERPA)	$1698.23 \pm 12.53^{+151.57}_{-151.14}$	$1864.30 \pm 13.10^{+171.46}_{-172.40}$
Z+jets(ALPGEN no corr.)	$1845.97 \pm 30.29^{+249.04}_{-221.68}$	$2192.18 \pm 33.42^{+252.17}_{-203.64}$
Z+jets(ALPGEN)	$1724.75 \pm 28.39^{+171.14}_{-169.59}$	$1913.88 \pm 29.22^{+179.73}_{-179.85}$
Other Bkg.	$86.71 \pm 4.02^{+35.45}_{-35.64}$	$93.74 \pm 4.28^{+37.99}_{-38.26}$
Total Bkg.(ALPGEN)	$1811.45 \pm 28.67^{+176.17}_{-174.62}$	$2007.61 \pm 29.54^{+184.53}_{-184.50}$
Total Bkg.(SHERPA)	$1784.93 \pm 13.16^{+156.98}_{-156.76}$	$1958.04 \pm 13.79^{+176.53}_{-177.34}$
Data	1811	2050

2.6.4. Comparisons after H_T requirement

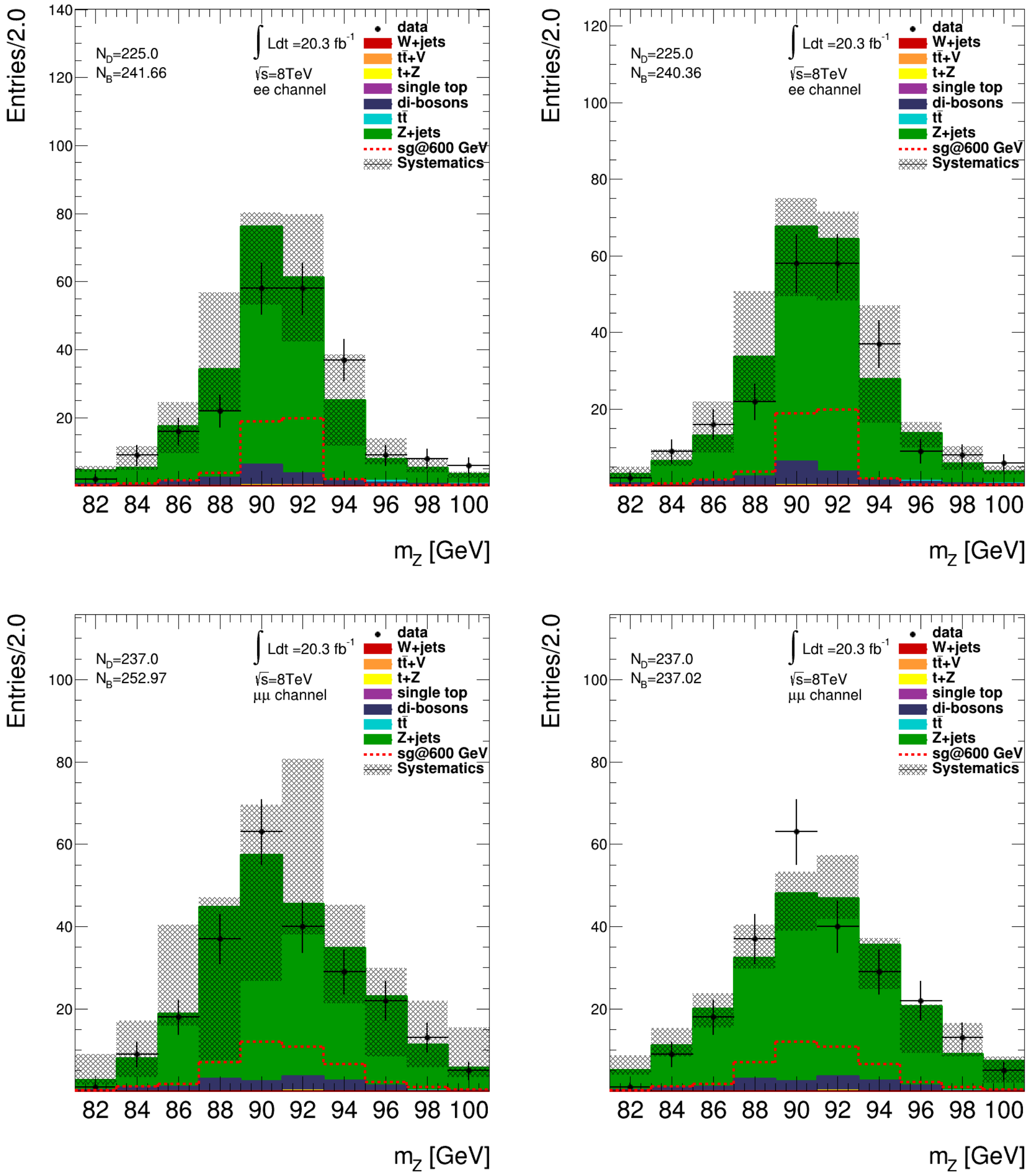

Figure 2.43. M_Z distributions in $Z+\geq 4$ jets sample after applying H_T cut. Left(right) column consists of ALPGEN (SHERPA) Z+jets sample.

Very large systematic fluctuations in a given distribution such as in the above figures does not necessarily cause large fluctuations in the number of events, which is basically the integral of the distribution. Fluctuation correlations in between the bins of the distribution keep the integral almost intact. Such systematic errors are classified as shape errors.

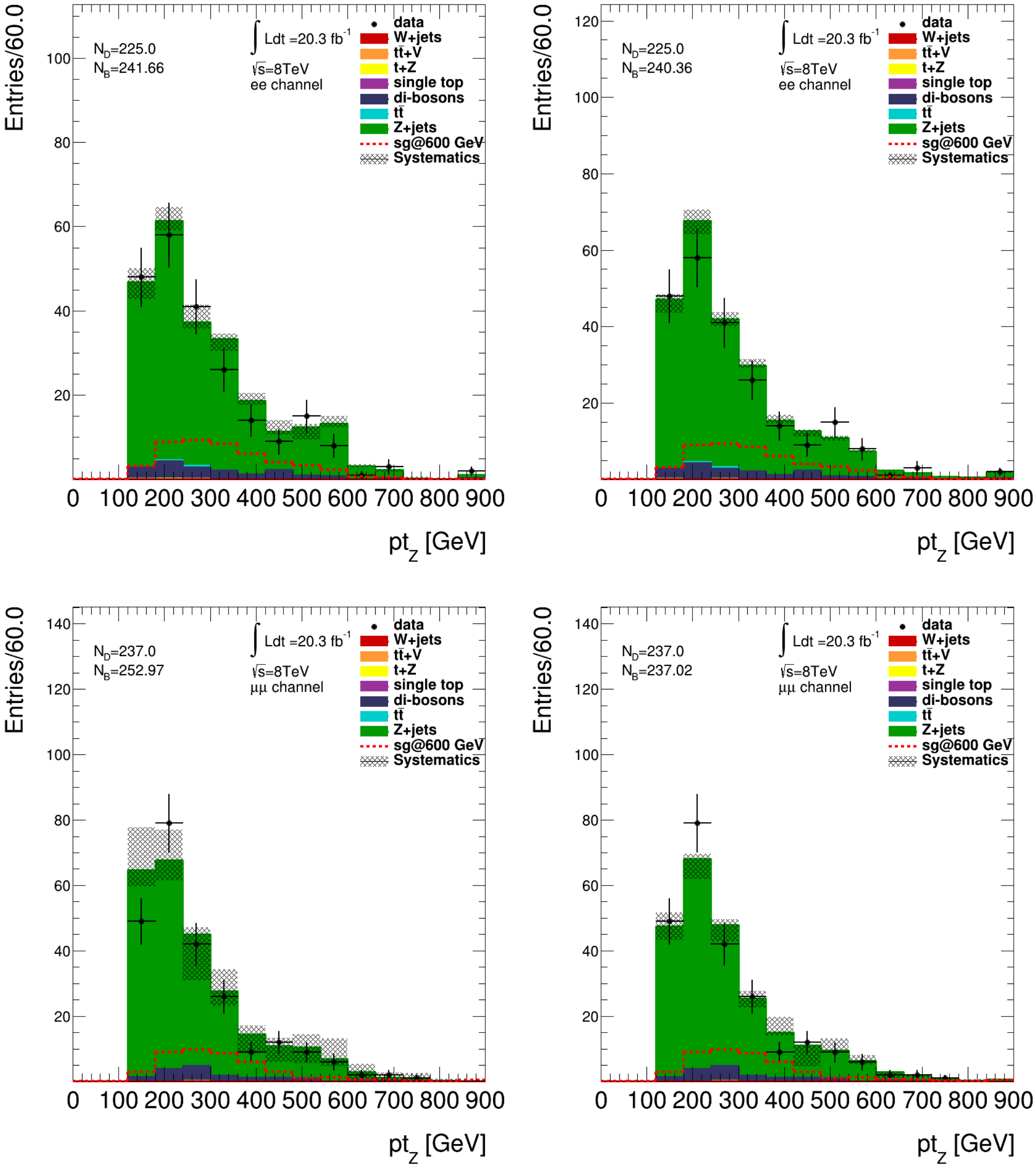

Figure 2.44. $p_{\mathrm{T}}(Z)$ distributions in $Z+\geq 4$ jets sample after applying H_{T} cut obtained by ALPGEN(left) and SHERPA.

Table 2.5. Number of expected and observed events after $H_{\mathrm{T}} \geq 600 GeV$ requirement.

	e^+e^- **channel**	$\mu^+\mu^-$ **channel**
signal (600 GeV)	$47.19 \pm 2.54^{+7.69}_{-7.71}$	$43.27 \pm 2.55^{+7.76}_{-6.76}$
Z+jets(SHERPA no corr.)	$268.88 \pm 5.34^{+29.88}_{-29.60}$	$274.94 \pm 5.03^{+23.93}_{-27.68}$
Z+jets(SHERPA)	$220.99 \pm 4.52^{+26.55}_{-26.33}$	$220.81 \pm 4.06^{+25.95}_{-29.49}$
Z+jets(ALPGEN no corr.)	$235.20 \pm 10.27^{+27.80}_{-25.20}$	$271.23 \pm 11.16^{+23.40}_{-24.45}$
Z+jets(ALPGEN)	$222.30 \pm 9.91^{+31.33}_{-31.01}$	$236.76 \pm 9.80^{+29.16}_{-30.54}$
Other Bkg.	$19.36 \pm 1.92^{+7.93}_{-7.99}$	$16.21 \pm 1.76^{+6.87}_{-6.83}$
Total Bkg.(ALPGEN)	$241.66 \pm 10.10^{+32.69}_{-32.48}$	$252.97 \pm 9.96^{+30.61}_{-31.23}$
Total Bkg.(SHERPA)	$240.36 \pm 4.91^{+28.04}_{-27.90}$	$237.02 \pm 4.42^{+27.14}_{-30.06}$
Data	225	237

2.6.5. Comparisons of the reconstructed variables

Four momentum reconstruction of the heavy quark pair is achieved by choosing the jet configuration which yields the minimum of the χ^2 in equation 2.1. Invariant mass of the leptonically reconstructed heavy quark is used instead of fully hadronic heavy quark mass as a final discriminant because lepton energy-momentum measurements are much more precise than for jets at ATLAS.

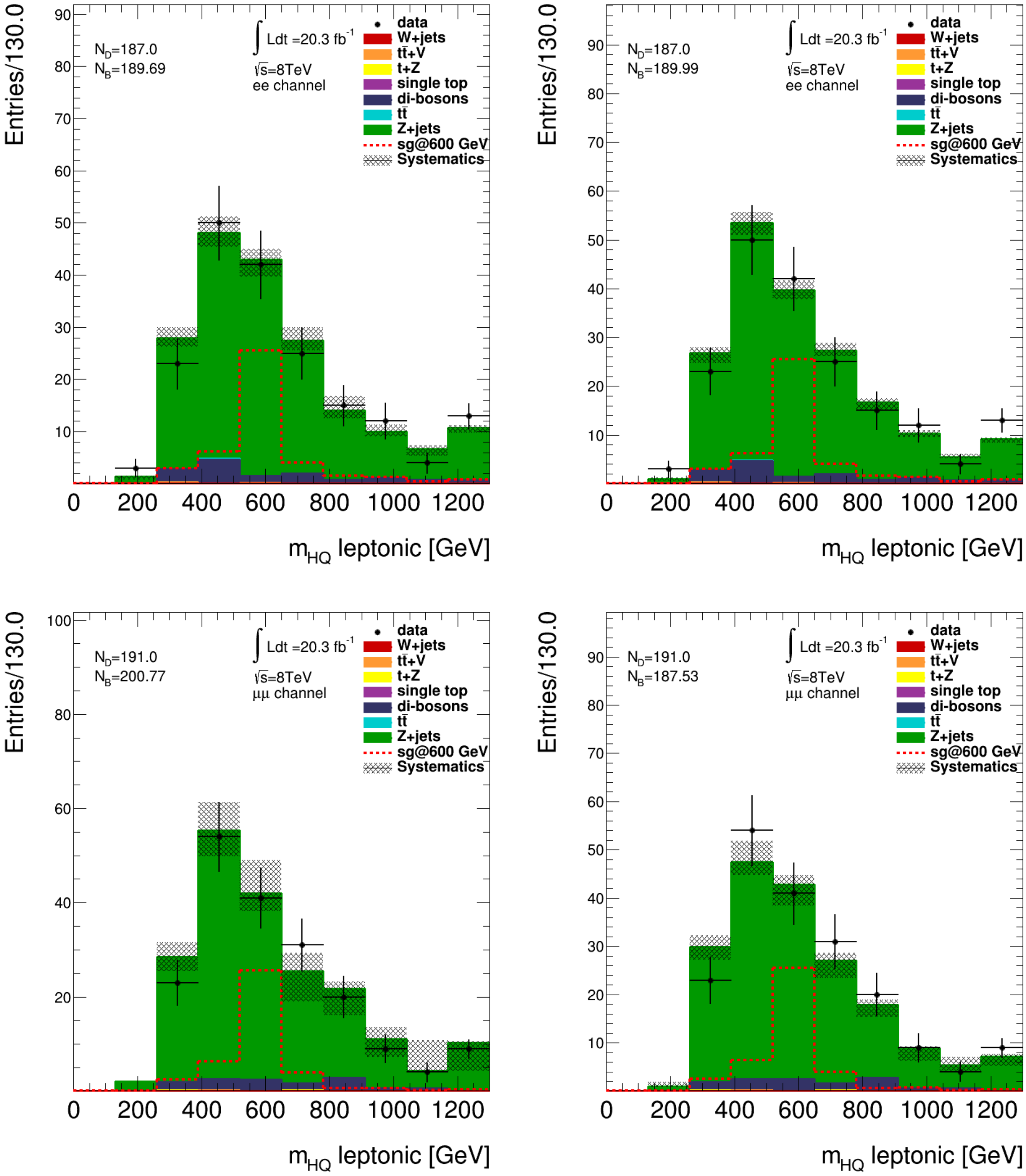

Figure 2.45. Leptonically reconstructed D quark mass in e^+e^- and $\mu^+\mu^-$ channels with ALPGEN(left) and SHERPA.

We increase the sensitivity of our search by further applying a loose cut of mass windows around hadronically reconstructed vector boson as shown in figure 2.46. The real value of the vector boson mass is taken as $M_V = \frac{1}{2}(M_Z + M_W)$ and selected events should fall inside a mass window with a width of 100 GeV around M_V. This cut

Table 2.6. Number of expected and observed events in the reconstructed sample.

	e^+e^- **channel**	$\mu^+\mu^-$ **channel**
signal (600 GeV)	$43.18 \pm 2.43^{+7.09}_{-7.08}$	$40.55 \pm 2.46^{+6.89}_{-6.36}$
Z+jets(SHERPA no correction)	$212.18 \pm 4.90^{+22.74}_{-22.43}$	$217.45 \pm 4.50^{+19.42}_{-21.52}$
Z+jets(SHERPA)	$175.20 \pm 4.15^{+20.67}_{-21.12}$	$174.72 \pm 3.63^{+20.36}_{-23.45}$
Z+jets(ALPGEN no correction)	$184.22 \pm 9.04^{+20.80}_{-19.86}$	$214.27 \pm 9.75^{+18.00}_{-21.09}$
Z+jets(ALPGEN)	$174.90 \pm 8.77^{+24.10}_{-24.80}$	$187.95 \pm 8.61^{+22.91}_{-24.98}$
Other Bkg.	$14.79 \pm 1.66^{+6.06}_{-6.02}$	$12.81 \pm 1.57^{+5.51}_{-5.51}$
Total Bkg.(ALPGEN)	$189.69 \pm 8.93^{+25.16}_{-25.82}$	$200.77 \pm 8.75^{+23.78}_{-25.41}$
Total Bkg.(SHERPA)	$189.99 \pm 4.47^{+21.93}_{-22.29}$	$187.53 \pm 3.95^{+21.41}_{-23.87}$
Data	187	191

may seem to be loose but it is carefully chosen not to reduce statistics but increase signal/background ratio slightly.

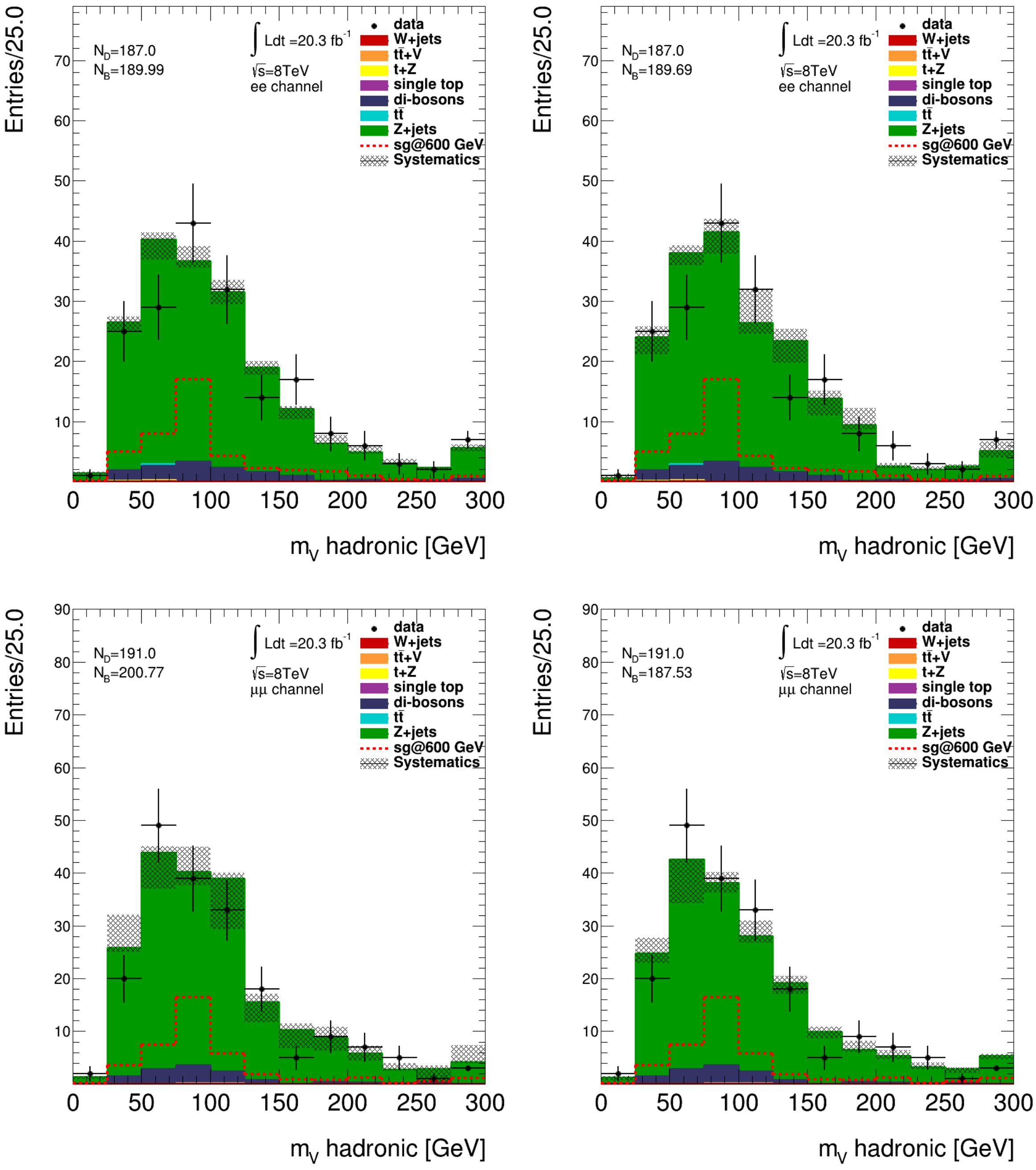

Figure 2.46. Hadronically reconstructed W/Z boson mass in e^+e^- and $\mu^+\mu^-$ channels as obtained from ALPGEN(left) and SHERPA.

And finally we impose the requirement that the mass difference between the heavy quark and its anti-particle should not be very large. As can be seen from the below figure the expected signal have a sharper and more symmetric distribution of mass difference than the expected background. We apply a loose cut such that $|M_D - M_{\bar{D}}| \leq$

100 GeV to eliminate some more background.

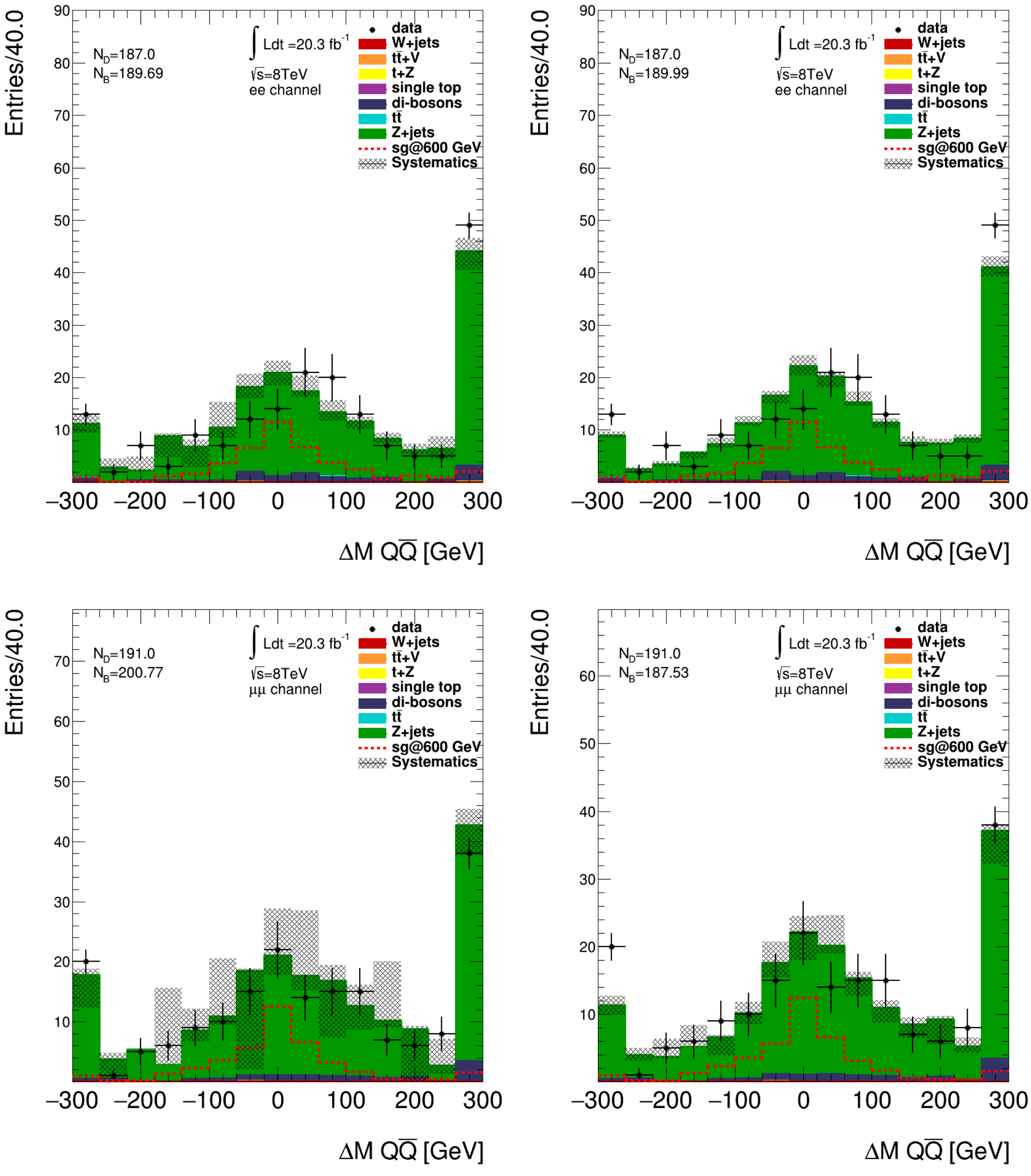

Figure 2.47. Mass difference between pairs of reconstructed D quarks in the both channels as obtained by ALPGEN(left) and SHERPA.

The signal/background enhancement of the two mass window cuts can easily be seen when Figures 2.45 and 2.48 are compared. Signal remains almost unchanged but the backgrounds have been eliminated by a factor of 1.6. We use the final distribution 2.48 in the hypothesis testing.

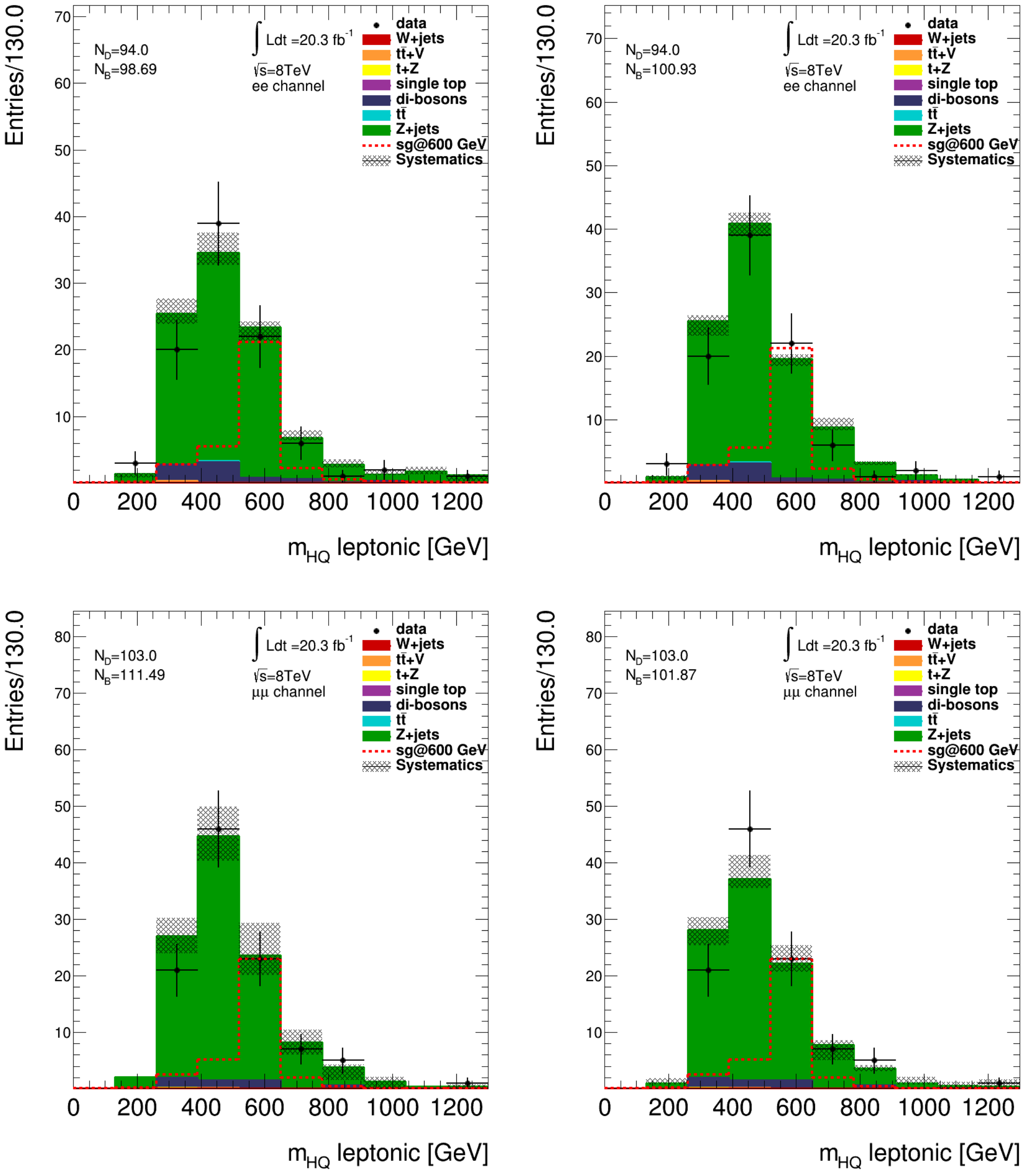

Figure 2.48. Leptonically reconstructed D quark mass after $|M_D - M_{\bar{D}}|$ and $|M_{jj} - M_V| \leq 100$ GeV cuts in the both channels obtained by ALPGEN(left) and SHERPA.

Table 2.7. Number of expected and observed events in the final selection.

	e^+e^- **channel**	$\mu^+\mu^-$ **channel**
signal (600 GeV)	$32.97 \pm 2.10^{+5.38}_{-5.39}$	$33.23 \pm 2.23^{+5.56}_{-5.36}$
Z+jets(SHERPA no correction)	$111.17 \pm 3.58^{+12.18}_{-13.05}$	$119.02 \pm 3.39^{+12.18}_{-10.86}$
Z+jets(SHERPA)	$92.65 \pm 3.02^{+10.03}_{-10.90}$	$96.10 \pm 2.75^{+11.48}_{-12.16}$
Z+jets(ALPGEN no correction)	$95.44 \pm 6.48^{+11.10}_{-10.29}$	$121.04 \pm 7.61^{+13.77}_{-15.60}$-
Z+jets(ALPGEN)	$90.41 \pm 6.22^{+11.31}_{-11.70}$	$105.73 \pm 6.68^{+16.21}_{-15.17}$
Other Bkg.	$8.28 \pm 1.24^{+3.46}_{-3.42}$	$5.76 \pm 1.02^{+3.40}_{-3.11}$
Total Bkg.(ALPGEN)	$98.69 \pm 6.35^{+12.00}_{-12.46}$	$111.49 \pm 6.75^{+16.23}_{-15.59}$
Total Bkg.(SHERPA)	$100.93 \pm 3.27^{+10.84}_{-11.59}$	$101.87 \pm 2.93^{+12.97}_{-12.72}$
Data	94	103

2.7. Systematic Uncertainties

Majority of the systematic errors arise from imperfections in the simulation events that most of our signal and background predictions are based on. Even after calibrating the detector, it is impossible to have a perfect detector, trigger and event simulations. For matching the simulations to the real data, each physics objects are treated with correction methods that are derived from different parts of the detector in dedicated studies. These are mainly classified in uncertainties on trigger and reconstruction efficiencies as well as with the uncertainties on energy-momentum resolutions of leptons and the jets. Such corrections are parametrized within the detector geometry in terms of the kinematic variables such $|\eta|$, p_{T} and E_{T} by the dedicated collaborative studies.

The other sources of systematic errors are normalization uncertainties which include theoretical uncertainties on cross sections of signal/background and the uncertainty on the integrated luminosity. We classify such sources of uncertainties as rate systematics.

We take the effect of these uncertainties into account by shifting them by $\pm 1\sigma$

around their nominal values and each shift is propagated through the full analysis chain to obtain its impact on the final discriminant. The correlations between each individual source of systematic error are small and are considered uncorrelated in the final analysis.

In addition to these, our data driven correction methods have associated systematic errors related to them.The error on b-jet multiplicity correction is manifested as uncertainty in Z+jets cross section where $p_{\mathrm{T}}(Z)$ correction has an associated shape systematics.

2.7.1. Luminosity

The uncertainty on the integrated luminosity is ±2.8%. This value has been extracted from a previous luminosity scale measurement carried out by a Van Der Meer scan of the interaction point in November 2012. This uncertainty effects all of the simulated backgrounds as a normalization factor.

2.7.2. Background and Signal Cross Sections

Although we started with a decent theoretical cross sections as predicted by an NNLO calculation at the inclusive Z boson selection, due to a slightly digressed jet multiplicities predicted by each event generator, we applied a rate correction obtained by a data driven method. So the cross section uncertainty of the $Z+\geq 4$ jets background is the systematic error on these correction factors and taken to be ±6.5% as derived in the 0 b-tag exclusive bin.

There is also an additional systematic error related to the data-driven $p_{\mathrm{T}}(Z)$ shape correction applied to the $Z+\geq 4$ jets sample. This correction has been derived from a finite statistics of data and simulated events so statistical errors here are taken as a systematic. We shift the correction factors in Figure 2.38 and 2.39 around their nominal values with $\pm 1\sigma$ of the associated statistical errors. The effect of up and down shifts are propagated through the full analysis chain and shifted distributions are taken into account in the final analysis.

The only remaining background events at the final selection are from di-boson processes with cross section uncertainty of 34%.

Uncertainties on the signal samples vary with each mass point from 9% to 14% as calculated by perturbative QCD calculator TOP++ at NNLO+NNLL order. [2]

2.7.3. Systematics related to data-driven $p_{\mathrm{T}}(Z)$ correction

The $p_{\mathrm{T}}(Z)$ correction has been derived in two different control regions with the hope that fluctuations are small with respect to each other. Due to the freedom in choosing the two control regions, we symmetrize the difference between the two and consider it as a systematic error at the final event selection.

2.7.4. Lepton Trigger, Identification, and Reconstruction

Lepton trigger and reconstruction efficiencies are measured from clean $Z \to ee$ and $Z \to \mu\mu$ processes by using real and simulated data events by Electron and Muon performance groups. By using the both kind of samples, scale factors are derived in different parts of the detector and parametrized in terms of lepton kinematics to compensate any disagreement between real data and simulation. The uncertainties on these scale factors create systematic errors on lepton related variables in the analysis.

2.7.5. Lepton Energy-Momentum Scale and Resolution

$Z \to ee$ and $Z \to \mu\mu$ events are very good candidates to measure these leptonic quantities inside the detector. Due to different lepton energy-momentum resolutions between real data and simulated events, these variables are smeared in the simulated events to match the real data. Muons' momenta and electrons' energies are applied

---

[2] NNLL mode refers to resummation of the next to nexto leading order logarithmic soft gluon terms

such scale factors in the simulated events. $\pm 1\sigma$ shifts of these smearing and scaling factors are considered as a systematic error.

2.7.6. Jet Reconstruction Efficiency and Jet Energy Scale

Since jets are reconstructed from energy deposits in the calorimeters, jet properties heavily depend on various real-life factors such as distribution of the large bulk material inside the detector and pile-up events. Jet reconstruction efficiencies are measured by using minimum-bias and QCD di-jet events in slices of jet p_{T} and $|\eta|$. The different jet reconstruction efficiencies between data and simulated events are mimicked by randomly dropping some of the jets in the simulated samples. Jet energy scale is measured from various sources like test-beam and collision data as well as from the truth informations given by the simulated events. Scale factors are applied to simulation events to match reconstructed jet energies to the real data.

The systematic uncertainties on jet quantities are important due to the requirement of at least 4 jets in our analysis. They are supposedly the major source of systematic shifts on the final distributions.

2.7.7. B-jet Uncertainties

Uncertainties on b-jet properties depend on performance studies of the neural network based tagging algorithms with capability of separating heavy flavor c and b-jets [62]. By using truth information from the simulated events, b-jets are applied certain scale factors in bins of $|\eta|$ and p_{T} to match the real data. Our analysis is not very sensitive to uncertainties on these scale factors since we reject b-jets.

Impacts of each individual source of systematic errors on the number of final events are shown in Tables 2.8 and 2.9 in percentage errors separately for each simulated sample.

Table 2.8. List of all systematic errors in the e^+e^- channel.

Syst. Source	Signal (600 GeV)	OtherBG	Z+jets	Total bkg.
b-jet energy scale	+0.0/-0.0	+0.0/-0.0	+0.1/+0.0	+0.1/+0.0
b-tagging	+0.9/-0.9	+3.1/-3.0	+1.1/-1.0	+1.2/-1.1
Electron energy resolution	+0.5/-0.3	+5.0/-5.3	-0.0/-0.6	+0.4/-0.1
Electron energy scale	+0.1/-0.6	+6.4/-2.7	+2.3/-1.7	+2.7/-1.8
Electron identification	+5.4/-5.2	+5.0/-4.9	+0.1/-0.1	+0.5/-0.5
Electron reconstruction	+0.7/-0.7	+0.7/-0.7	+0.0/-0.0	+0.1/-0.1
Electron trigger	+0.0/+0.0	+0.0/+0.0	-0.0/-0.0	-0.0/-0.0
Jet reconstruction	+0.7/-0.7	+2.3/-2.3	+0.6/-0.6	+0.7/-0.7
Jet energy scale	+0.0/-0.4	+3.3/-1.7	+1.5/-2.0	+1.7/-2.0
Jet vertex fraction	+0.3/-0.6	+0.2/-3.5	+2.5/-4.7	+2.3/-4.6
Luminosity	+2.8/-2.8	+2.8/-2.8	+2.8/-2.8	+2.8/-2.8
Mis-tagging	+1.0/-1.0	+0.9/-0.8	+0.9/-0.9	+0.9/-0.9
Other BG. Cross Sect.	–	+40.0/-40.0	–	+3.3/-3.3
PTZ correction (REGION)	–	–	+1.0/-1.0	+0.9/-0.9
PTZ correction (STAT)	–	–	+6.9/-6.9	+6.4/-6.3
Pile-up	+0.6/-0.4	+2.9/+3.4	-0.4/-0.1	-0.1/+0.2
Z+jets Cross Sect.	–	–	+6.5/-6.5	+6.0/-6.0
Signal Cross Sect.	+15.0/-15.0	–	–	+0.0/+0.0
Total	+16.3/-16.4	+42.2/-41.4	+10.8/-11.9	+10.8/-11.6

Table 2.9. List of all systematic errors in the $\mu^+\mu^-$ channel.

Syst. Source	Signal (600 GeV)	OtherBG	Z+jets	Total bkg.
b-jet energy scale	+0.8/-0.6	+0.5/-5.1	+0.2/-0.2	-0.1/+0.1
b-tagging	+0.9/-1.6	+6.5/-12.0	+0.6/-1.3	+0.9/-0.5
Jet reconstruction	+0.2/-0.2	+15.2/-15.2	+4.0/-4.0	+4.6/-4.6
Jet energy scale	+1.4/-0.9	+3.9/-12.2	+2.4/-0.6	+2.4/-0.1
Jet vertex fraction	+5.3/-0.7	+9.0/-1.4	+1.9/-5.0	+2.3/-4.8
Luminosity	+2.8/-2.8	+2.8/-2.8	+2.8/-2.8	+2.8/-2.8
Mis-tagging	+2.7/-2.5	+11.1/-13.4	+1.3/-0.5	+1.8/-0.3
Muon identification	+2.3/-1.6	+9.1/-0.5	+0.8/-0.2	+1.3/-0.1
Muon momentum scale	+0.1/-0.7	+8.9/-7.5	+0.2/-0.1	+0.3/-0.3
Muon reconstruction	+0.2/-0.1	+10.0/-0.4	+0.3/-0.1	+0.9/-0.1
Muon momentum resolution	+0.4/-0.1	+6.8/-0.3	+0.2/-1.8	+0.5/-1.7
Muon trigger	+0.0/-1.0	+4.7/-0.3	+0.4/+0.3	+0.6/-0.3
Other BG. Cross Sect.	–	+40.0/-40.0	–	+2.3/-2.3
PTZ correction (REGION)	–	–	+3.9/-3.9	+3.7/-3.7
PTZ correction (STAT)	–	–	+6.3/-6.4	+5.9/-6.0
Pile-up	+1.4/-1.1	+12.6/+2.5	+0.1/-0.0	+0.8/-0.1
Z+jets Cross Sect.	–	–	+6.5/-6.5	+6.1/-6.1
Signal Cross Sect.	+15.0/-15.0	–	–	+0.0/+0.0
Total	+16.8/-16.2	+56.5/-50.0	+12.0/-12.6	+12.6/-12.4

3. FINAL RESULTS

Even though no excess events have been observed on top of the Standard Model, a certain region for possible D quark mass range have been excluded by setting an upper limit on the $D\bar{D}$ cross section. The final distributions 2.48 of the leptonically reconstructed heavy quark mass have been used in the hypothesis testing to set upper limits on $D\bar{D}$ production cross section. These limits have been calculated with the CL_s method [63] implemented in the MCLIMIT [64] program. This method utilizes a maximization of the log likelihood ratio function :

$$LLR = -2\ln\prod_{i=1}^{N}\left(\frac{L_{s+b}}{L_b}\right)^{(i)} \tag{3.1}$$

where N is the number of bins and L_{s+b} (L_b) is the binned likelihood function computed under the hypothesis that the data is represented by background-plus-signal (background only). To compute the likelihood functions, a number of pseudo-experiments are carried out at each bin of the distributions taking statistical and systematical fluctuations into account. Statistical fluctuations are treated according to the Poisson statistics where systematical errors are considered as Gaussian fluctuations.

.

$$CL_s = \left(\frac{CL_{s+b}}{CL_b}\right) \tag{3.2}$$

In the above equation the variable CL_{s+b} (CL_b) is the number of pseudo-experiments satisfying a certain LLR threshold value under signal-plus-background (background only) hypothesis. Signal cross sections are varied in small increments and the pseudo-experiments are repeatedly carried out at each iteration. Then the largest cross section satisfying $CL_s \leq 0.05$ correspond to the upper limit with 95% confidence level.

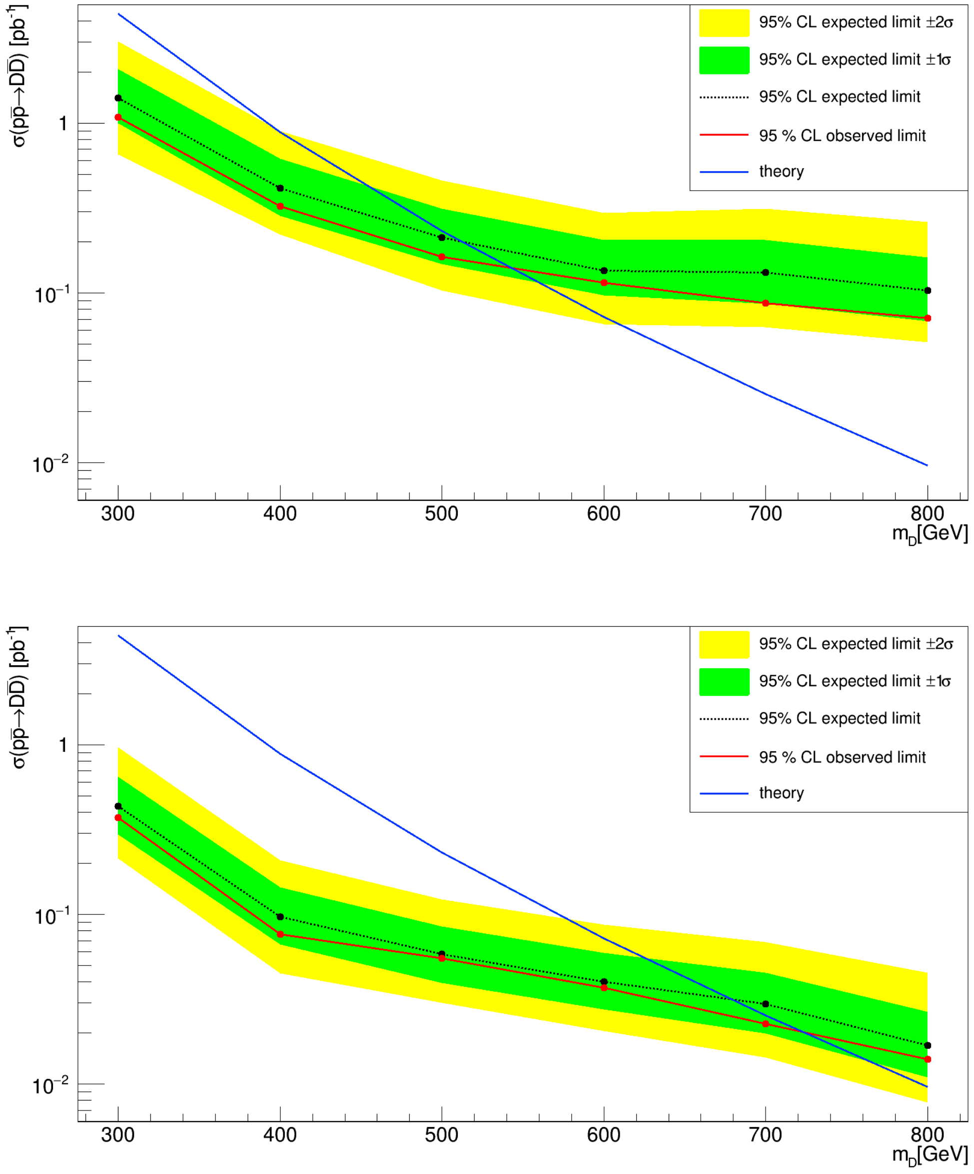

Figure 3.1. Expected and observed 95% CL upper limits on the D quark pair production cross section. The green and yellow bands correspond to the 1 and 2 standard deviations around the expected limit where the blue line shows the theoretical prediction.

By repeating this procedure for different hypothetical D quark masses, the cross section exclusion plots, such as the ones in the Figure 3.1 are obtained. Using the pair production cross section predictions and the expected branching ratios in the E_6 model we exclude heavy quarks with mass less than 530 GeV. The bottom exclusion plot is for the assumption that D decays via Z with 100% branching ratio. In that case we exclude quarks with mass less than 730 GeV.

3.1. Future Prospects

LHC will be delivering proton-proton collisions with an increased center of mass energies around $\sqrt{s}$=13 TeV soon. With these new LHC running parameters, this search will be sensitive to the D quarks beyond TeV mass regime. Moreover, by combining our results with the other similar heavy quark searches [65] with different decay modes of D, we will get a wider picture in terms of the results.

APPENDIX A: VALIDATION OF SIGNAL SAMPLES

CompHEP signal events have been validated from the obtained distributions at the truth level. Distributions from each mass points are put in different colors and superimposed to reflect the effects of increasing heavy quark mass.

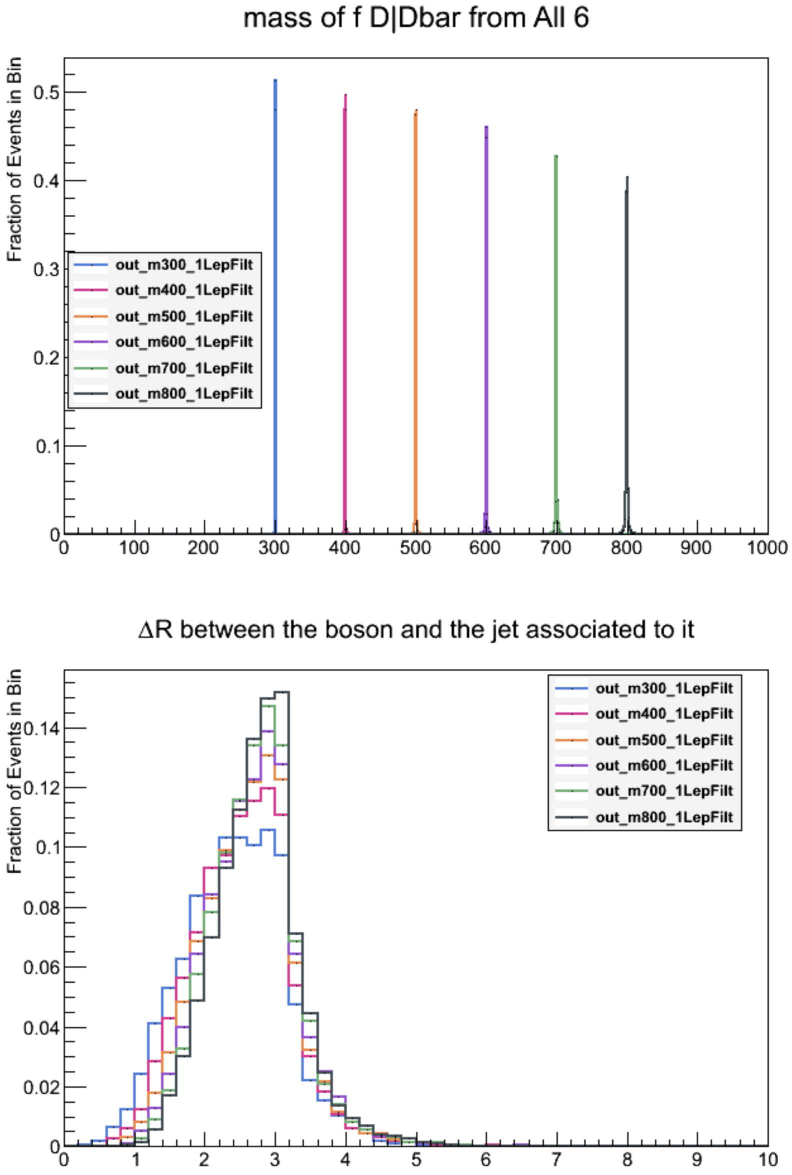

Figure A.1. Heavy quark mass and angular separation between bosons and the associated jets for the signal events at the truth level

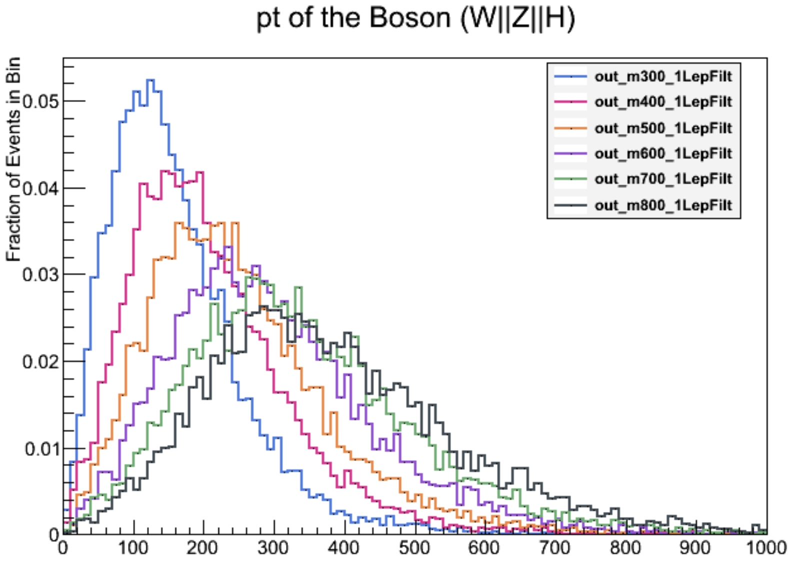

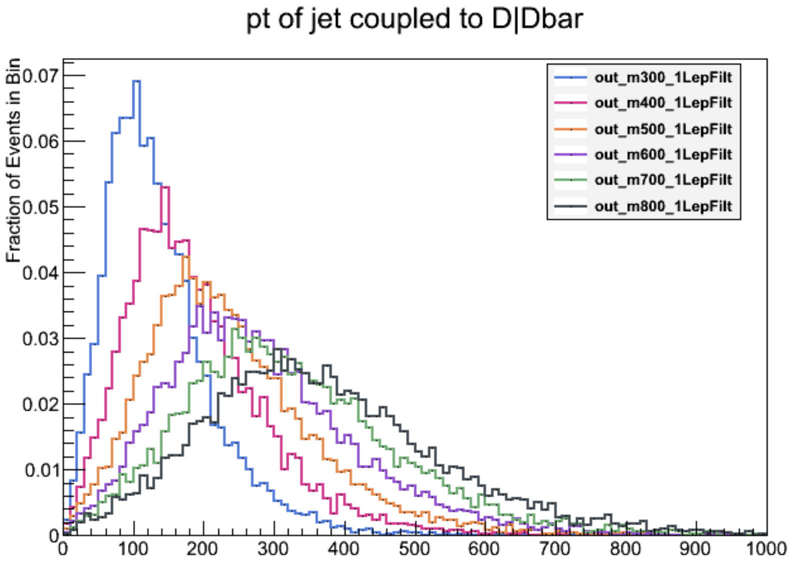

Figure A.2. Traansverse momenta of the bosons and the jets coupled to the heavy quark for the signal events at the truth level

Each signal sample contains equal number of events from the six possible $D\bar{D}$ decay modes in order to study any set of branching ratios by reweighting the events. Here are the applied weight distributions for each sub-channel. X and Y edges of the below triangles correspond to $BR(D \longrightarrow W + u)$ and $BR(D \longrightarrow Z + d)$ respectively

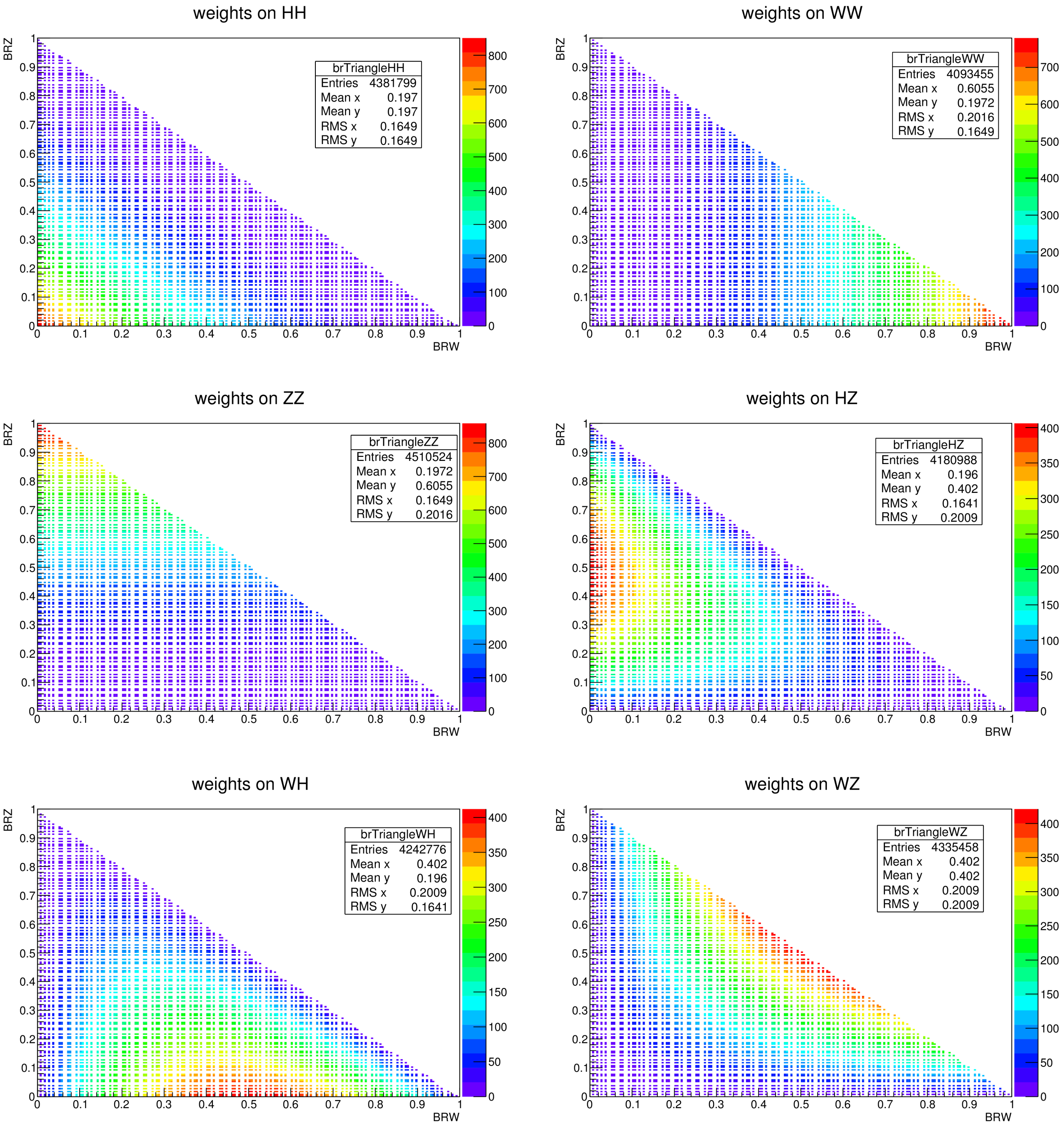

Figure A.3. Applied event weight distributions for each decay mode for the signal events

APPENDIX B: ΔR DISTRIBUTION BETWEEN Z BOSON AND THE p_{T} ORDERED JETS

In addition to the figures 2.40, here are the channel-wise versions of the similar figures

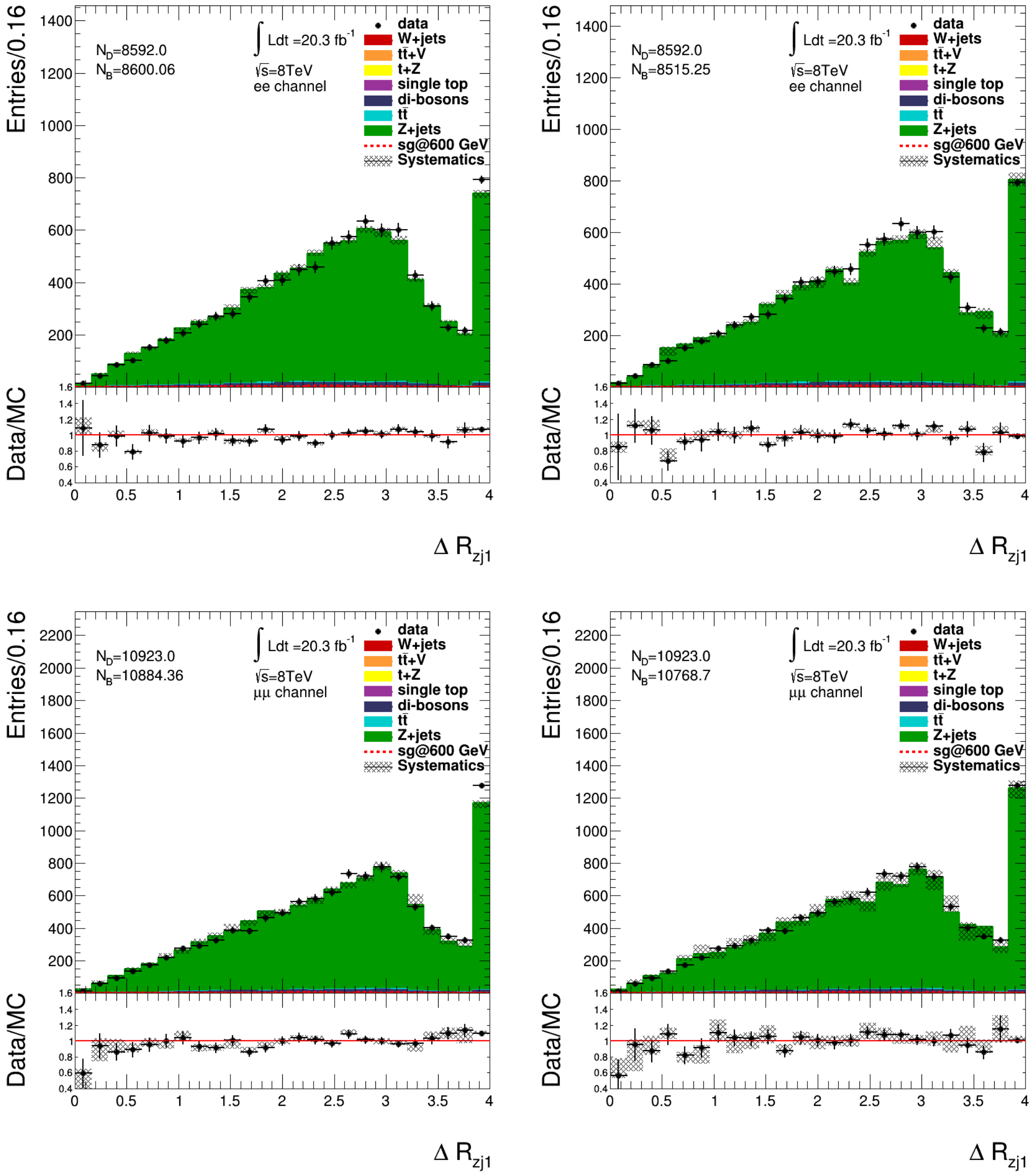

Figure B.1. ΔR between Z boson and the second hardest jet in the event at Z+$\geq$ 4 jets sample after data-driven $p_{\mathrm{T}}Z$ correction and b-jet veto are applied. Left(right) column is obtained by ALPGEN(SHERPA) Z+jets sample

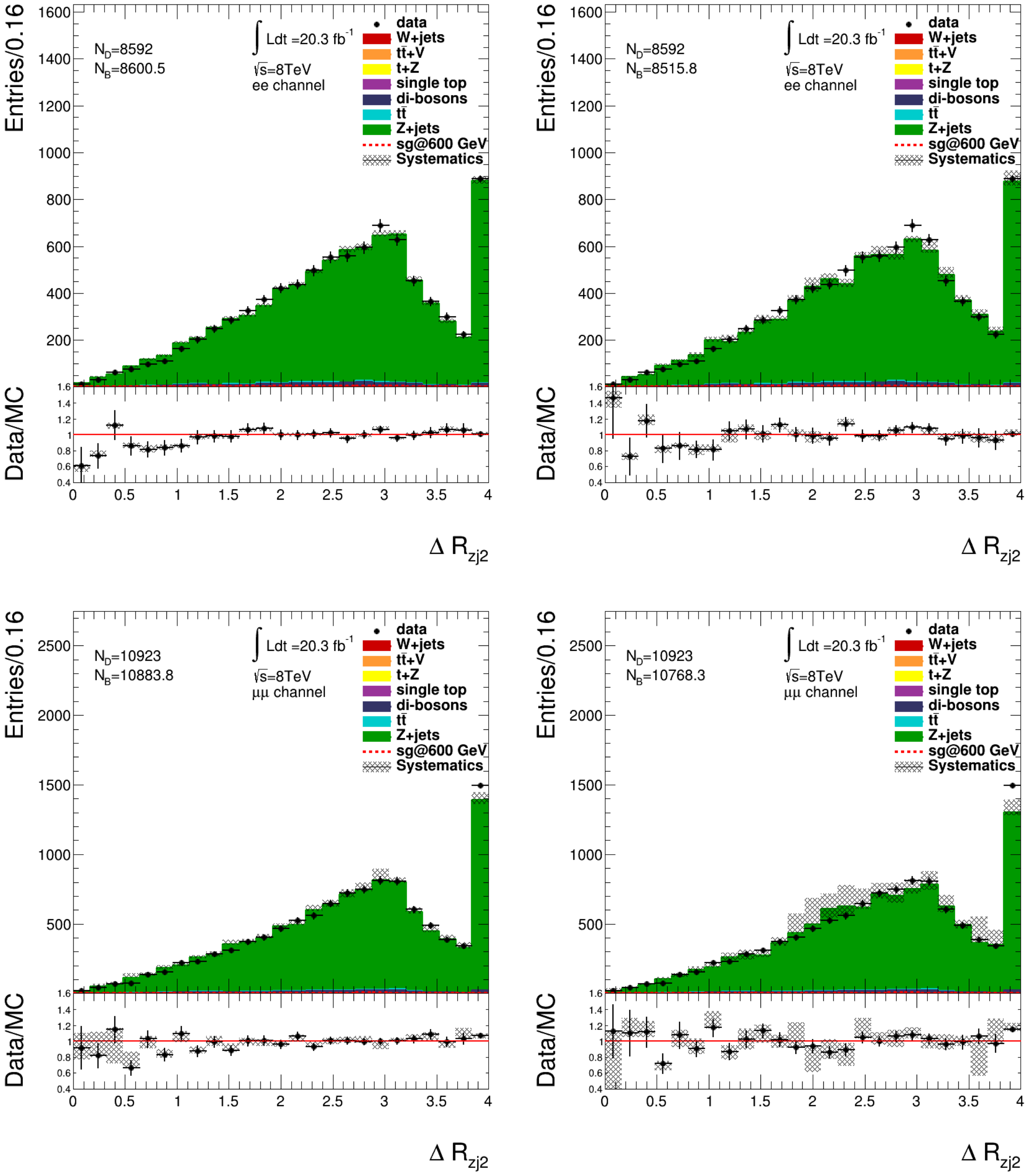

Figure B.2. ΔR between Z boson and the third hardest jet in the event at Z+$\geq$ 4 jets sample after data-driven $p_{\mathrm{T}}Z$ correction and b-jet veto are applied. Left(right) column is obtained by ALPGEN(SHERPA) Z+jets sample

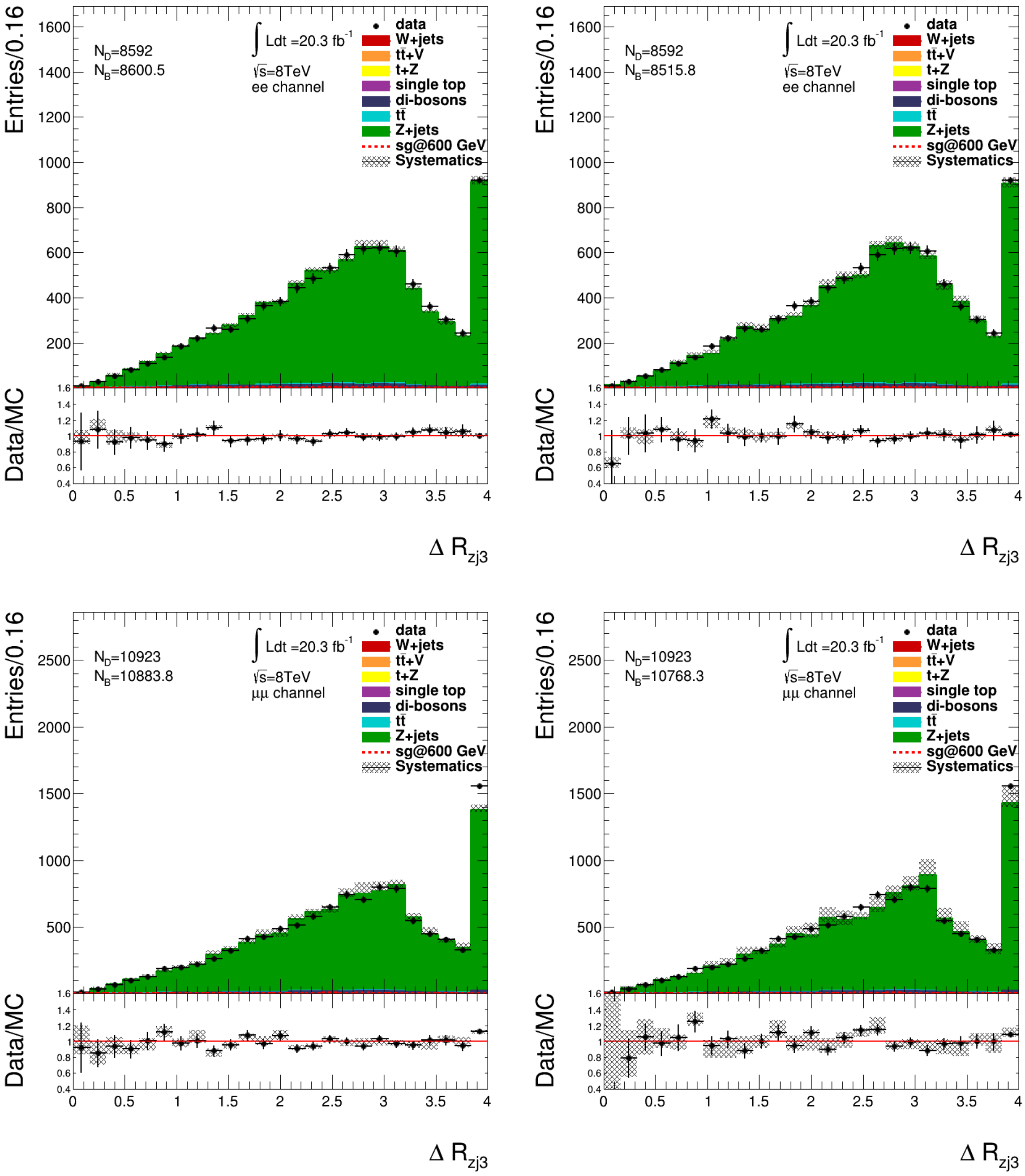

Figure B.3. ΔR between Z boson and the fourth hardest jet in the event at Z+$\geq$ 4 jets sample after data-driven $p_{\mathrm{T}}Z$ correction and b-jet veto are applied. Left(right) column is obtained by ALPGEN(SHERPA) Z+jets sample

APPENDIX C: RECONSTRUCTION PERFORMANCE IN THE REVERTED H_{T} CONTROL REGION

The below figures show the leptonically reconstructed heavy quark mass in the reverted H_{T} control region. .

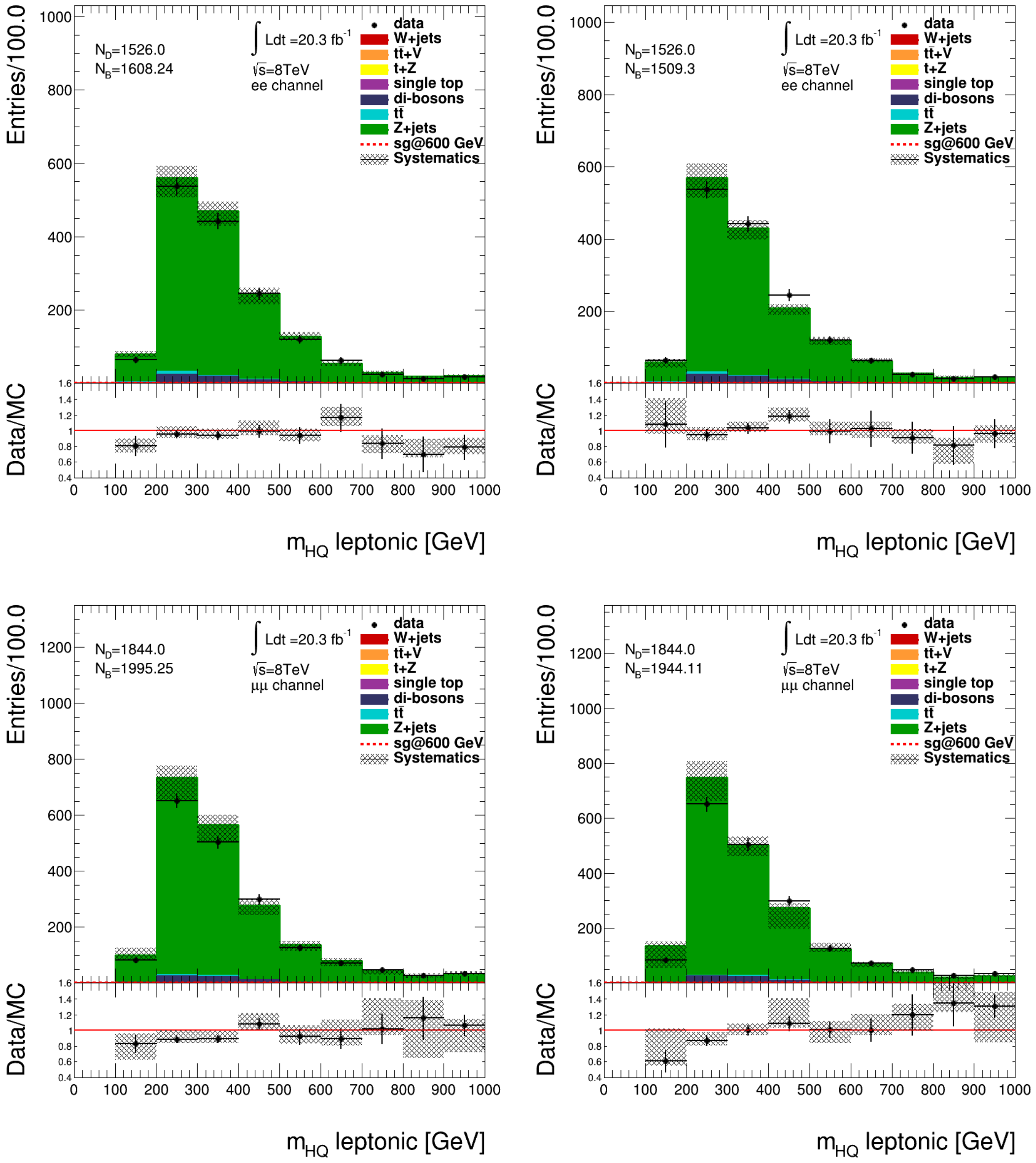

Figure C.1. Leptonically reconstructed D quark mass in e^+e^- and $\mu^+\mu^-$ channels with ALPGEN(left) and SHERPA in the reverted H_{T} control region

REFERENCES

1. Olive, K. and P. D. Group, “Review of Particle Physics”, *Chinese Physics C*, Vol. 38, No. 9, p. 090001, 2014.

2. Nakano, T. and K. Nishijima, “Charge Independence for V-particles”, *Progress of Theoretical Physics*, Vol. 10, No. 5, pp. 581–582, 1953.

3. Nishijima, K., “Charge Independence Theory of V-particles”, *Progress of Theoretical Physics*, Vol. 13, No. 3, pp. 285–304, 1955.

4. Arnison, G., A. Astbury, B. Aubert, C. Bacci, G. Bauer, A. Bézaguet, R. Böck *et al.*, “Experimental Observation of Lepton Pairs of Invariant Mass Around 95 GeV/c2 at the CERN SPS Collider”, *Physics Letters B*, Vol. 126, No. 5, pp. 398 – 410, 1983.

5. Arnison, G., A. Astbury, B. Aubert, C. Bacci, G. Bauer, A. Bézaguet, Böck *et al.*, “Experimental Observation of Isolated Large Transverse Energy Electrons with Associated Missing Energy at s= 540 GeV”, *Physics Letters B*, Vol. 122, No. 1, pp. 103–116, 1983.

6. Rubbia, C., “Experimental Observation of the Intermediate Vector Bosons W^+, W^-, and Z^0”, *Rev. Mod. Phys.*, Vol. 57, pp. 699–722, Jul 1985.

7. Lüscher, M., S. Sint, R. Sommer, P. Weisz and U. Wolff, “Non-perturbative O (a) Improvement of Lattice QCD”, *Nuclear Physics B*, Vol. 491, No. 1, pp. 323–343, 1997.

8. Andersson, B., G. Gustafson, G. Ingelman and T. Sjöstrand, “Parton Fragmentation and String Dynamics”, *Physics Reports*, Vol. 97, No. 2, pp. 31–145, 1983.

9. Fukuda, Y., T. Hayakawa, E. Ichihara, K. Inoue, K. Ishihara, H. Ishino, Y. Itow,

T. Kajita, J. Kameda, S. Kasuga *et al.*, “Evidence for Oscillation of Atmospheric Neutrinos”, *Physical Review Letters*, Vol. 81, No. 8, p. 1562, 1998.

10. McLerran, L., M. Shaposhnikov, N. Turok and M. Voloshin, “Why the Baryon Asymmetry of the Universe is 10^{-10}”, *Physics Letters B*, Vol. 256, No. 3, pp. 477–483, 1991.

11. Moore, B., S. Ghigna, F. Governato, G. Lake, T. Quinn, J. Stadel and P. Tozzi, “Dark Matter Substructure within Galactic Halos”, *The Astrophysical Journal Letters*, Vol. 524, No. 1, p. L19, 1999.

12. Aad, G., T. Abajyan, B. Abbott, J. Abdallah, S. A. Khalek, A. Abdelalim, O. Abdinov, R. Aben, B. Abi, M. Abolins *et al.*, “A Particle Consistent with the Higgs Boson Observed with the ATLAS Detector at the Large Hadron Collider”, *Science*, Vol. 338, No. 6114, pp. 1576–1582, 2012.

13. Chatrchyan, S., V. Khachatryan, A. M. Sirunyan, A. Tumasyan, W. Adam, E. Aguilo, T. Bergauer, M. Dragicevic, J. Erö, C. Fabjan *et al.*, “Observation of a New Boson at a Mass of 125 GeV with the CMS Experiment at the LHC”, *Physics Letters B*, Vol. 716, No. 1, pp. 30–61, 2012.

14. Georgi, H. and S. L. Glashow, “Unity of all Elementary-particle Forces”, *Physical Review Letters*, Vol. 32, No. 8, p. 438, 1974.

15. Regis, C., K. Abe, Y. Hayato, K. Iyogi, J. Kameda, Y. Koshio, L. Marti, M. Miura, S. Moriyama, M. Nakahata *et al.*, “Search for Proton Decay via p$\rightarrow$ μ+K0 in Super-Kamiokande I, II, and III”, *Physical Review D*, Vol. 86, No. 1, p. 012006, 2012.

16. Langacker, P., “Grand Unified Theories and Proton Decay”, *Physics Reports*, Vol. 72, No. 4, pp. 185–385, 1981.

17. Gürsey, F., P. Ramond and P. Sikivie, “A Universal Gauge Theory Model Based

on E_6", *Physics Letters B*, Vol. 60, No. 2, pp. 177–180, 1976.

18. Mehdiyev, R., S. Sultansoy, G. Unel and M. Yilmaz, "Prospects to Search for E_6 Isosinglet Quarks in ATLAS", *The European Physical Journal C*, Vol. 49, No. 2, pp. 613–622, 2007.

19. Sultansoy, S. and G. Unel, "The E_6 Inspired Isosinglet Quark and the Higgs Boson", *Physics Letters B*, Vol. 669, No. 1, pp. 39–45, 2008.

20. ALEPH Collaboration, DELPHI Collaboration, L3 Collaboration, OPAL Collaboration, LEP Electroweak Working Group *et al.*, "Electroweak Measurements in Electron–Positron Collisions at W-boson-pair Energies at LEP", *Physics reports*, Vol. 532, No. 4, pp. 119–244, 2013.

21. ALEPH collaboration, CDF collaboration, D0 Collaboration, DELPHI collaboration, L3 Collaboration, OPAL collaboration, SLD collaboration, LEP Electroweak Working Group, Tevatron Electroweak Working Group *et al.*, "Precision Electroweak Measurements and Constraints on the Standard Model", *arXiv preprint arXiv:1012.2367*, 2010.

22. The LEP Working Group, ALEPH Collaboration, DELPHI Collaboration, L3 Collaboration, OPAL Collaboration *et al.*, "Search for the Standard Model Higgs boson at LEP", *Physics Letters B*, Vol. 565, pp. 61–75, 2003.

23. Lamont, M., "Status of the LHC", *Journal of Physics: Conference Series*, Vol. 455, p. 012001, IOP Publishing, 2013.

24. Atlas Collaboration, "Luminosity Public Results", `https://twiki.cern.ch/twiki/bin/view/AtlasPublic/LuminosityPublicResults`, 2013 (accessed August 2015).

25. Atlas Collaboration, "ATLAS Detector and Physics Performance Technical Design Report", *CERN/LHCC*, Vol. 99, No. 14, pp. 99–15, 1999.

26. Ros, E., “ATLAS Inner Detector”, *Nuclear Physics B-Proceedings Supplements*, Vol. 120, pp. 235–238, 2003.

27. Aad, G., B. Abbott, J. Abdallah, A. Abdelalim, A. Abdesselam, O. Abdinov, B. Abi, M. Abolins, H. Abramowicz, H. Abreu *et al.*, “The ATLAS Inner Detector Commissioning and Calibration”, *The European Physical Journal C*, Vol. 70, No. 3, pp. 787–821, 2010.

28. Aad, G., M. Ackers, F. Alberti, M. Aleppo, G. Alimonti, J. Alonso, E. Anderssen, A. Andreani, A. Andreazza, J. Arguin *et al.*, “ATLAS Pixel Detector Electronics and Sensors”, *Journal of Instrumentation*, Vol. 3, No. 07, p. P07007, 2008.

29. ATLAS collaboration *et al.*, “Operation and Performance of the ATLAS Semiconductor Tracker”, *Journal of Instrumentation*, Vol. 9, No. 08, p. P08009, 2014.

30. Abat, E., T. Addy, T. Åkesson, J. Alison, F. Anghinolfi, E. Arik, M. Arik, G. Atoian, B. Auerbach, O. Baker *et al.*, “The ATLAS Transition Radiation Tracker (TRT) Proportional Drift Tube: Design and Performance”, *Journal of Instrumentation*, Vol. 3, No. 02, p. P02013, 2008.

31. Jackson, J. D., *Classical Electrodynamics*, Vol. 3, Wiley New York., 1962.

32. ATLAS collaboration *et al.*, “Particle Identification Performance of the ATLAS Transition Radiation Tracker”, ATLAS-CONF-2011-128, 2011.

33. Sutton, M., A. Collaboration *et al.*, “Commissioning the ATLAS Inner Detector Trigger”, *Journal of Physics: Conference Series*, Vol. 219, p. 022021, IOP Publishing, 2010.

34. Ilic, N., “Performance of the ATLAS Liquid Argon Calorimeter After Three Years of LHC Operation and Plans for a Future Upgrade”, *Journal of Instrumentation*, Vol. 9, No. 03, p. C03049, 2014.

35. Aad, G., B. Abbott, J. Abdallah, A. Abdelalim, A. Abdesselam, O. Abdinov, B. Abi, M. Abolins, H. Abramowicz, H. Abreu *et al.*, "Readiness of the ATLAS Tile Calorimeter for LHC Collisions", *The European Physical Journal C*, Vol. 70, No. 4, pp. 1193–1236, 2010.

36. Diehl, E. *et al.*, "Calibration and Performance of the ATLAS Muon Spectrometer", *arXiv preprint arXiv:1109.6933*, 2011.

37. Atlas Collaboration *et al.*, "ATLAS Magnet System Technical Design Report", *Technical Design Report ATLAS. CERN, Geneva*, 1997.

38. Astigarraga, M. P., A. collaboration *et al.*, "Evolution of the ATLAS Trigger and Data Acquisition System", *Journal of Physics: Conference Series*, Vol. 608, p. 012006, IOP Publishing, 2015.

39. Aad, G., B. Abbott, J. Abdallah, A. Abdelalim, A. Abdesselam, O. Abdinov, B. Abi, M. Abolins, H. Abramowicz, H. Abreu *et al.*, "Performance of the ATLAS Trigger System in 2010", *The European Physical Journal C*, Vol. 72, No. 1, pp. 1–61, 2012.

40. Czakon, M. and A. Mitov, "Top++: a Program for the Calculation of the Top-pair Cross-section at Hadron Colliders", *Computer Physics Communications*, Vol. 185, No. 11, pp. 2930–2938, 2014.

41. ATLAS collaboration *et al.*, "Search for Pair and Single Production of New Heavy Quarks that Decay to a Z Boson and a Third-generation Quark in pp Collisions at $\sqrt{s}s$=8 TeV with the ATLAS Detector", *arXiv preprint arXiv:1409.5500*, 2014.

42. Allison, J., K. Amako, J. Apostolakis, H. Araujo, P. A. Dubois, M. Asai, G. Barrand, R. Capra, S. Chauvie, R. Chytracek *et al.*, "Geant4 Developments and Applications", *Nuclear Science, IEEE Transactions on*, Vol. 53, No. 1, pp. 270–278, 2006.

43. Lukas, W., “Fast Simulation for ATLAS: Atlfast-II and ISF”, *Journal of Physics: Conference Series*, Vol. 396, p. 022031, IOP Publishing, 2012.

44. Mangano, M. L., F. Piccinini, A. D. Polosa, M. Moretti and R. Pittau, “ALPGEN, a Generator for Hard Multiparton Processes in Hadronic Collisions”, *Journal of High Energy Physics*, Vol. 2003, No. 07, p. 001, 2003.

45. Gleisberg, T., S. Höche, F. Krauss, M. Schönherr, S. Schumann, F. Siegert and J. Winter, “Event Generation with SHERPA 1.1”, *Journal of High Energy Physics*, Vol. 2009, No. 02, p. 007, 2009.

46. Kretzer, S., H. Lai, F. I. Olness and W. Tung, “CTEQ6 Parton Distributions with Heavy Quark Mass Effects”, *Physical Review D*, Vol. 69, No. 11, p. 114005, 2004.

47. Sjöstrand, T., S. Mrenna and P. Skands, “A Brief Introduction to PYTHIA 8.1”, *Computer Physics Communications*, Vol. 178, No. 11, pp. 852–867, 2008.

48. Aad, G., T. Abajyan, B. Abbott, J. Abdallah, S. A. Khalek, A. A. Abdelalim, O. Abdinov, R. Aben, B. Abi, M. Abolins *et al.*, “Study of Heavy Flavor Quarks Produced in Association with Top-quark Pairs at $\sqrt{s}s$=7 TeV Using the ATLAS Detector”, *Physical Review D*, Vol. 89, No. 7, p. 072012, 2014.

49. Guzzi, M., P. Nadolsky, B. Edmond, L. Hung-Liang, O. Fredrick and C.-P. Yuan, “CT10 Parton Distributions and Other Developments in the Global QCD Analysis”, *arXiv preprint arXiv:1101.0561*, 2011.

50. Schonherr, M., S. Höche, F. Krauss and F. Siegert, “Merging of Matrix Elements and Parton Showers at NLO Accuracy”, *arXiv preprint arXiv:1311.3634*, 2013.

51. Alioli, S., P. Nason, C. Oleari and E. Re, “A general Framework for Implementing NLO Calculations in Shower Monte Carlo Programs: the POWHEG BOX”, *Journal of High Energy Physics*, Vol. 2010, No. 6, pp. 1–58, 2010.

52. Alwall, J., M. Herquet, F. Maltoni, O. Mattelaer and T. Stelzer, "MadGraph 5: Going Beyond", *Journal of High Energy Physics*, Vol. 2011, No. 6, pp. 1–40, 2011.

53. Frixione, S. and B. R. Webber, "Matching NLO QCD Computations and Parton Shower Simulations", *Journal of High Energy Physics*, Vol. 2002, No. 06, p. 029, 2002.

54. Boos, E., V. Bunichev, M. Dubinin, L. Dudko, V. Edneral, V. Ilyin, A. Kryukov, V. Savrin, A. Semenov and A. Sherstnev, "CompHEP 4.4 Automatic Computations from Lagrangians to Events", *Nuclear Instruments and Methods in Physics Research Section A: Accelerators, Spectrometers, Detectors and Associated Equipment*, Vol. 534, No. 1, pp. 250–259, 2004.

55. Aad, G., B. Abbott, J. Abdallah, A. Abdelalim, A. Abdesselam, O. Abdinov, B. Abi, M. Abolins, H. Abramowicz, H. Abreu *et al.*, "Charged-particle Multiplicities in pp Interactions Measured with the ATLAS Detector at the LHC", *New Journal of Physics*, Vol. 13, No. 5, p. 053033, 2011.

56. Piacquadio, G., K. Prokofiev and A. Wildauer, "Primary Vertex Reconstruction in the ATLAS Experiment at LHC", *Journal of Physics: Conference Series*, Vol. 119, p. 032033, IOP Publishing, 2008.

57. Aad, G., T. Abajyan, B. Abbott, J. Abdallah, S. A. Khalek, O. Abdinov, R. Aben, B. Abi, M. Abolins, O. AbouZeid *et al.*, "Electron Reconstruction and Identification Efficiency Measurements with the ATLAS Detector Using the 2011 LHC Proton-Proton Collision Data", *The European Physical Journal C*, Vol. 74, No. 7, pp. 1–38, 2014.

58. Drohan, J., J. Couchman, N. Konstantinidis, Z. Maxa, H. Drevermann, C. F. Crijns, E. Jansen, P. Klok, C. Timmermans, D. Petrusca *et al.*, "The ATLANTIS Visualisation Program for the ATLAS Experiment", *Proc. of Computing in High Energy Physics (CHEP'04)*, pp. 361–364, 2004.

59. Aad, G., B. Abbott, J. Abdallah, S. A. Khalek, O. Abdinov, R. Aben, B. Abi, M. Abolins, O. AbouZeid, H. Abramowicz *et al.*, "Measurement of the Muon Reconstruction Performance of the ATLAS Detector Using 2011 and 2012 LHC Proton-Proton Collision Data", *The European Physical Journal C*, Vol. 74, No. 11, pp. 1–34, 2014.

60. Cacciari, M., G. P. Salam and G. Soyez, "The Anti-kt Jet Clustering Algorithm", *Journal of High Energy Physics*, Vol. 2008, No. 04, p. 063, 2008.

61. Aad, G., T. Abajyan, B. Abbott, J. Abdallah, S. A. Khalek, A. Abdelalim, O. Abdinov, R. Aben, B. Abi, M. Abolins *et al.*, "Jet Energy Resolution in Proton-Proton Collisions at $\sqrt{s}s$=7 TeV Recorded in 2010 with the ATLAS Detector", *The European Physical Journal C*, Vol. 73, No. 3, pp. 1–27, 2013.

62. ATLAS collaboration *et al.*, "Commissioning of the ATLAS High-Performance b-tagging Algorithms in the 7 TeV Collision Data", ATLAS-CONF-2011-102, 2011.

63. Read, A. L., "Presentation of Search Results: the CLs Technique", *Journal of Physics G: Nuclear and Particle Physics*, Vol. 28, No. 10, p. 2693, 2002.

64. Junk, T. *et al.*, "Sensitivity, Exclusion and Discovery with Small Signals, Large Backgrounds, and Large Systematic Uncertainties", *CDF Public note*, , No. 8128, 2007.

65. ATLAS Collaboration *et al.*, "Search for Pair Production of a New Heavy Quark that Decays into a W Boson and a Light Quark in pp Collisions at $\sqrt{s}$=8 TeV with the ATLAS Detector", *arXiv preprint arXiv:1509.04261*, 2015.